UNIVERSITÀ DEGLI STUDI DI FERRARA

DOTTORATO DI RICERCA IN FISICA

XXVIII CICLO

COORDINATORE: PROF. GUIDI VINCENZO

Fabrication and characterization of silicon bent crystals for channeling experiments

---

SETTORE SCIENTIFICO DISCIPLINARE: FIS/01

Dottorando:
Dott. GERMOGLI Giacomo

Tutore:
Prof. GUIDI Vincenzo

Anni: 2013 - 2015

Contents

Introduction

A high energy charged particle traveling in an amorphous material loses energy by ionization and its trajectory is affected by the multiple Coulomb scattering, due to uncorrelated collisions with the atoms. If the atoms of the target were distributed according to an ordered scheme, the uncorrelated collisions would turn into a coherent interaction with the whole atomic structure. This is the case of a crystal, which is a solid material whose constituent atoms are arranged in a highly ordered microscopic structure, forming a crystal lattice that extends in all directions. Since that, depending on the orientation, a crystal is seen as a set of atomic planes or strings by the impinging particles. In particular, planes and strings produce potential wells which are able to confine the charged particles in a transversal region of the crystal, in the so called channeling condition. This phaenomenon may even occour in a slightly bent crystals, so that particles are forced to follow the curvature, being deflected.

In particle accelerators, particle deflection is provided by bending magnets, which are bulky device that produce a magnetic field induced by the current injected in its coils: bending magnetic dipoles currently installed in LHC can generate magnetic fields up to 8 Tesla [1]. A bent crystal can be used to obtain the same effect, indeed the particles can be deflected exploiting the electric field generated at the atomic scale by the crystalline planes; in this way an equivalent magnetic field of hundreds of Tesla can be produced [2]. However, crystal present an important limitation: while in a bending magnet particles can travel in vacuum inside the beam pipe, in a crystalline medium the presence of nuclei and electrons cannot be avoided, resulting in a certain amount of scattering. This causes a perturbation of particle trajectory and produces a deflection efficiency smaller that 100%. This is the reason why it is impossible to replace bending magnets with bent crystals. Despite of that limitation, from late 70's, several theoretical and experimental studies were done to prove the possibility to manipulate charged particles beam with crystals, and the feasibility of some elective applications.

Among the different applications, a special interest is present around beam collimation and beam extraction. For instance, a crystal-assisted collimation for high-energy hadron machines has been proposed. Such collimation scheme consists

in the usage of a short bent crystal as primary collimator to deflect channeled particles of the beam halo. Promising results were achieved in the last years of tests of crystal-assisted collimation in the CERN Super Proton Synchrotron (SPS), in the framework of the UA9 Collaboration [3], thus demonstrating the principle feasibility of such technology for the collimation of the LHC beam [4]. Crystal assisted extraction, which was the first application proposed for a bent crystal in accelerator physics [5], was recently proposed for modern high energy particle accelerator in the framework of the CRYSBEAM project [6].

Another issue related to channeling is the study of radiation emission by channeled electrons or positrons, which oscillate during their motion inside a crystal [7]. This phenomenon was called channeling radiation and has been exploited for the production of intense electromagnetic radiation [8]. Lighter particles are employed for these studies, since they generate the highest intensity radiation because bremsstrahlung strongly decreases with particle mass. In particular, owing to the comparatively high number of accelerators delivering GeV- or sub-GeV- energy electron beams, the study of channeling radiation is of special interest in view of developing some elective applications, such as a crystalline undulator. Once again, as well as a crystalline deflector was proposed as an alternative to huge bending magnets, an undulated crystal can be imagined as an alternative to free electron lasers for certain applications.

Since the beginning of my Ph. D, my research activity regarded the study of coherent interaction between charged particles and oriented crystals, in which I have been involved since the first observation of efficient steering of GeV-energy electrons in a bent crystals, through the study of electromagnetic emission accompanying coherent interactions in a bent crystal, to the very recent first test of crystal-assisted collimation of the LHC proton beam at maximum energy. In particular, I made use of the resources available at the Sensor Semiconductor Laboratories (SSL) of Ferrara, consisting of a clean room facility with all the equipment for processing prime semiconductor material (i.e. photolitograpic line, mechanical dicing machine, chemical etching set) and measurement instruments for high precision characterization (Veeco white light interferometer, Fogale infrared interferometer, Panalytical high-resolution X-ray diffractometer). My activities consisted of:

- manufacturing and bending of silicon crystals for channeling experiments by means of a revisitation of the techniques for semiconductor processing at SSL. I autonomously managed with this part.
- high resolution characterization of the specimens, both morphological and structural, independently performed by means of the measurement instruments available at SSL.
- active participation to data taking at the accelerator facilities (H4- and

H8-extracted lines at CERN-SPS, MAMI accelerator at Mainz-Germany, AN2000 accelerator at National Laboratories of Legnaro-Italy).

After Chapter 1, which gives an overview of the main concepts of coherent interactions for a charged particles moving in a crystal, the attention of this thesis is centered into the description of how crystalline devices are fabricated and characterized at SSL, given in Chapter 2. This part is composed of both some original work representing the latest improvement in manufacturing and measuring technologies, as well as of a review of the innovative techniques developed by my group in the last decade, which are still employed at the present time. Chapter 3 shows experimental results about beam steering and radiation emission obtained with sub-GeV electrons at MAMI and with GeV electrons at SLAC. Chapter 4 shows the results of characterization of the latest prototypes of strip and multistrip for collimation and extraction performed at the H8 extracted line of CERN-SPS, comparing it to the results of precharacterization at SSL. Moreover, preliminary result indicating the first evidence of channeling at the LHC will be shown.

Chapter 1

Orientational effects in crystals

The idea that the atomic order in crystal may be important for the processes of interaction of charged particles with matter is dated 1912, thanks to Stark [9]. However, only in the early 1960s the channeling effect was discovered in computer simulations [10], and in experiments [11] where anomalously long penetration depth of ions entering in crystal were observed. The theoretical explanation of the channeling effects has been given by Lindhard [12], which by channeling meant that a particle path near the channel center along a major axis (plane) in a crystal may have a certain stability.

In the 1976 Tsyganov suggested to use slightly bent monocrystals to deflect high-energy particle beams [13]; his idea was that a channeled particle would follow the direction of the bent atomic planes (or axes), thus deviating from its initial direction by an angle equal to the bending angle of the crystal. In 1979 the possibility of steering beams of charged particles using bent crystal was first demonstrated in an experiment on the deflection of 8.4 GeV proton beam extracted from the synchrophasotron of the Laboratory of High Energies, JINR [14].

In the following years many other effects were discovered through Monte Carlo simulations, for instance volume capture and volume reflection. The first one consists in capturing a charged particle into a channeling mode in the depth of a bent single crystal, in a region where the particle trajectories are tangential to the crystallographic planes. This effect was discovered in 1982 using a beam of 1 GeV protons [15–17]. The second one consists in the deflection of particles tangent to the crystal curvature in a direction opposite to the crystal bending and hence opposite to the one of the channeled particles deflection. This effect, which was called volume reflection, was found in computer simulations in 1987 [18] and was experimentally proved in 2006 [19].

In this chapter, an overview of the main concepts of coherent interactions in straight and bent crystals will be given, following the scheme proposed in [2].

1.1 Coherent Interactions in Straight Crystals

In this section the theoretical explanation of the channeling phenomenon given by Lindhard is presented [12]. Any charged particle traversing an amorphous medium, which is characterized by homogeneity, isotropy and randomness, or a misaligned crystal, makes uncorrelated collisions with single atoms. These collisions may be of different nature , depending on different impact parameters; the most common are angular scattering in multiple collisions with atomic nuclei and energy loss in collisions with atomic electrons. So in a random system the slowing-down process is independent of direction and hence the probability distribution in energy loss and scattering angle depends only on the mass per cm^2 penetrated, and it has to be computed in a familiar way from single collisions. This is essentially a gas picture, and may be called a random system, implying homogeneity, isotropy and random collisions. The approximation of a random system is not confined to randomly distributed atoms or molecules, but may be also applied to media with lattice structure.

An anisotropy due to lattice structure can thus result in some kind of correlations between collisions. A single crystal is a typical example of a medium in which directional effect in stopping might appear, due to both inhomogeneity, anisotropy and lack of randomness. In fact, a crystal is a regular arrangement of atoms located on a lattice so that, depending on the point of view of the observer, the atoms are arranged in strings or plane.

The directional effects for charged particles traversing crystal were found for a number of processes requiring a small impact parameter in a particle-atom collision, e.g., nuclear reactions, large-angle scattering and energy loss. We may classify directional effects for charged particles moving through single crystal using two labels: ungoverned motion and governed motion. By ungoverned motion is meant the approximation where the path of the particle may be assumed to be essentially unaffected by the structure of the substance. Governed motion means that a path deviates definitely from the one in a random system, because the path is determined by the structure of the medium. Governed motion leads to more fundamental changes in physical processes, whereas ungoverned motion just show fluctuations in physical effects due to correlations.

For treatment of possible governed motion the scattering angle of the particle may be assumed to be small, because scattering by large angles would imply that the original direction is completely lost, as well as correlations associated with direction. The scattering of the particle is due to nuclear collisions, causing the interaction with the charge distribution of an atom as a whole through nearly elastic collision. Moreover, since collision requires that the particle comes close to the atom, strong correlations between collisions occur if the particle moves at a small angle with a row of atoms; if it passes close to one atom in a row, it must

also passes close to the neighboring atoms in the same row. This leads us to the concept of string of atoms that is characterized merely by the constant distance of separation, d, of atoms placed on a straight line; we assume this as the perfect string.

When the motion of a charged particle is aligned (or at a small angle) with a string (or plane), a coherent scattering with the atoms of the string (or plane) can occur. In the low-angle approximation we can replace the potentials of the single atoms with an averaged continuous potential. The atomic string (plane) in the continuum approximation gently steers a particle away from the atoms, therefore suppressing the encounters with small impact parameters listed above. The channeling phenomenon is due to the fact that the fields of the atomic axes and planes form the potential wells, where the particle may be trapped. Particles can be trapped between planes or axes, under planar or axial channeling, respectively.

1.1.1 Continuous approximation

The continuous approximation was developed by Lindhard to describe channeling and its related phenomena, but can be extended to all orientational phenomena because the same approximations hold. Coherent effects are primary phenomena, since they govern path of particles, and not secondary ones, which are determined by the path. Thus, four basic assumptions can be introduced for particles under orientational effects. First, angles of scattering may be assumed to be small. Indeed, scattering at large angles imply complete lost of the original direction. Secondly, because particle move at small angle with respect to an aligned pattern of atoms and collisions with atoms in a crystal demand proximity, correlations between collisions occur. Third, since coherent length l of scattering process ($l = 2E/q^2$, where E is the particle energy and q the transferred momentum) is larger than lattice constant, a classical picture can be adopted. Fourth, an idealized case of a perfect lattice may be used as a first approximation.

By following such assumptions, the continuous approximation can be inferred. Under such approximation, the potential of a plane of atoms $U(c)$ can be averaged along direction parallel to plane directions. Angle θ has to be greater than scattering angle ϕ with a single atom

$$U(x) = N d_p \int \int_{-\infty}^{+\infty} dydzV(\mathbf{r}) \tag{1.1}$$

where d_p is the interplanar distance, N is the atomic density and $V(\mathbf{r})$ is the potential of a particle-atom interaction.

If the distance between the particle and the atom $r = \sqrt{x^2 + y^2 + z^2}$ is not very much larger that the screening length of the particle-atom interaction a_{TF}, the Thomas-Fermi-like potential $V(\mathbf{r})$ can be described as

$$V_{TF}(r) = \frac{Z_1 Z_2 e^2}{r} \Phi\left(\frac{r}{a_{TF}}\right) \tag{1.2}$$

where Z_1 is the particle charge and Z_2 is the atomic number of the crystalline medium, e is the elementary charge, $\Phi(r/a_{TF})$ is the screening function. In the following it is often implicitly understood that $Z_1 \ll Z_2$ so that

$$a_{TF} = 0.8853 a_B \left(Z_1^{\frac{2}{3}} + Z_2^{\frac{2}{3}}\right)^{-\frac{1}{2}} \tag{1.3}$$

where $a_B = 0.529\text{Å}$ is the Bohr radius. By using the Thomas-Fermi-like potential, interplanar potential becomes

$$U(x) = 2\pi N d_p Z_1 Z_2 e^2 a_{TF} \exp\left(-\frac{x}{a_{TF}}\right) = U_{max} \exp\left(-\frac{x}{a_{TF}}\right) \tag{1.4}$$

where U_{max} is the maximum of the potential.

Basis of the approximation relies on the qualitative assumption that many consecutive atoms contribute to deflection of a particle trajectory. Thus, for relativistic particles, the time of collision $\Delta t \approx c\Delta z$ multiplied by momentum component parallel to plane direction, $p_z \sim p\cos\theta$, has to be large compared to distance d_z between atoms along particle direction, where p is particle momentum, p_z is momentum component along particle direction and θ is angle between particle direction and crystal plane orientation. Since collision time is approximately $\sim r_{min}/(v\sin\theta)$, where r_{min} is the minimal distance of approach, the condition for continuous approximation holds

$$\frac{\Delta z}{c} p\cos\theta \approx \frac{r_{min}}{\theta} \gg d_z \tag{1.5}$$

In the most restrictive form r_{min} is determined by the condition that kinetic transverse energy can not exceed potential transverse energy at r_{min}.

$$\frac{1}{2} p\beta\theta^2 = U(r_{min}) \tag{1.6}$$

Therefore, from previous equations, a condition can be derived, for which the continuous approximation still valid

$$\frac{a_{TF}}{d_z\theta}\left(1 - \frac{p\beta}{2U_{max}}\theta^2\right) \gg 1 \tag{1.7}$$

Two terms appear in the condition. One refers to Lindhard angle of channeling $\theta_L = \sqrt{2U_{max}/(p\beta)}$, which determines maximum angle for channeling. The other term is more interesting because it implies that $\theta < a_{TF}/d_z \sim 0.5\text{Å}/1\text{Å} \sim 0.5$ is

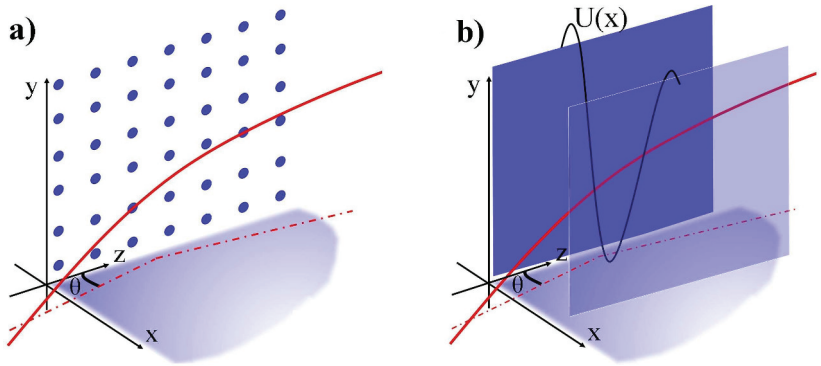

Figure 1.1: a. Trajectory of positive particle moving in a crystal misaligned with respect to the axis but at a small angle with respect to crystallographic plane. b. Continuous potential $U(x)$ is felt by the particle mainly due to the two neighboring planes. Adapted from [20].

very large compared to θ_L at high-energy. Thus, the continuous approximation is still valid for angle greater than θ_L by imposing that particle does not approach plane center closer than r_{min}.

The continuous potential approximation can be extended to a region closer than r_{min} to atomic position by treating in more detail atomic displacement in the structure. In fact, since crystal temperature is usually higher than 0 K degree, atoms vibrate around their center of mass. By averaging thermal vibration amplitude can be averaged over space and time, probability density function for the position of atoms can be derived. Thus, continuous approximation can be extended to region closer to center of vibration of atoms. Because of the averaging is due to thermal fluctuations, such approximation is not valid at very low temperature and limits for continuous approximation have to be treated carefully.

1.1.2 Potential under continuous approximation

A positive particle feels the effect of a whole plane instead of the individual atoms that compose the plane; in the conditions described before the electric field of two neighboring planes can trap the particle and so it could be channeled between the planes (see Fig. 1.1).

As a first order approximation, let us consider a perfect static lattice without atomic vibration. Several approximation can be used for the screening functions. By adopting the Lindhard approximation to the screening function

$$\Phi\left(\frac{r}{a_{TF}}\right) = 1 - \left(1 + \frac{3a^2{}_{TF}}{r^2}\right)^{-1/2} \tag{1.8}$$

the planar potential under continuous approximation is

$$U_{pl}(x) = 2\pi N d_p Z_1 Z_2 e^2 \left(\sqrt{x^2 + 3{a_{TF}}^2} - x\right) \tag{1.9}$$

The Moliére screening function [21] is widely used and is described by the analytical expression

$$\Phi\left(\frac{r}{a_{TF}}\right) = \sum_i \alpha_i \exp\left(-\frac{\beta_i r}{a_{TF}}\right) \tag{1.10}$$

where $\alpha = (0.1, 0.55, 0.35)$, $\beta = (6.0, 1.2, 0.3)$ are the Moliére's coefficients . Under such approximation the planar potential holds

$$U_{pl}(x) = 2\pi N d_p Z_1 Z_2 e^2 a_{TF} \sum_{i=1}^{3} \frac{\alpha_i}{\beta_i} \exp\left(-\frac{\beta_i x}{a_T F}\right) \tag{1.11}$$

When the particle travels aligned with a crystal axis it suffers the potential of the atomic row. The axial electric field is stronger than the planar. By averaging along the longitudinal coordinate of the string and by adopting the Lindhard approximation for the screening function, the axial continuous potential holds

$$U_{ax}(r) = \frac{Z_1 Z_2 e^2}{a_i} ln\left(1 + \frac{3{a_{TF}}^2}{r^2}\right) \tag{1.12}$$

where a_i is the interatomic spacing in the string and r is the minimum distance of the particle from the axis.

The above formulas well describe potential for a ideal case. The displacement of the lattice due to thermal vibrations of atoms in the structure can be introduced in the calculations. Thus, the static-lattice potential near the plane has to be modified at a a distance of the order of thermal vibrations root-mean square amplitude u_T. By assuming the independence of vibration for each atom, the isotropy of the displacement, the thermal vibrations can be averaged over space and time. Thus, the position of the nuclei in the atoms can be approximated by a gaussian probability function.

Because the amplitude of thermal vibration is usually small compared to an interatomic distance, the introduction of thermal vibration mainly affects the calculation of the potential near the atomic planes or axes. As an example, the interplanar distance for Si (110) planes is 1.92Å, which is ~ 25 times greater than $u_T = 0.075$Å at 300 K. The usage of a potential averaged over thermal vibration is fundamental to search for the solution of the equation of motion of quasi-channeled particles, which travel over the potential barrier and cross many planes. In fact, the sharp maximum for the ideal case is smoothed to a continuous function for the potential.

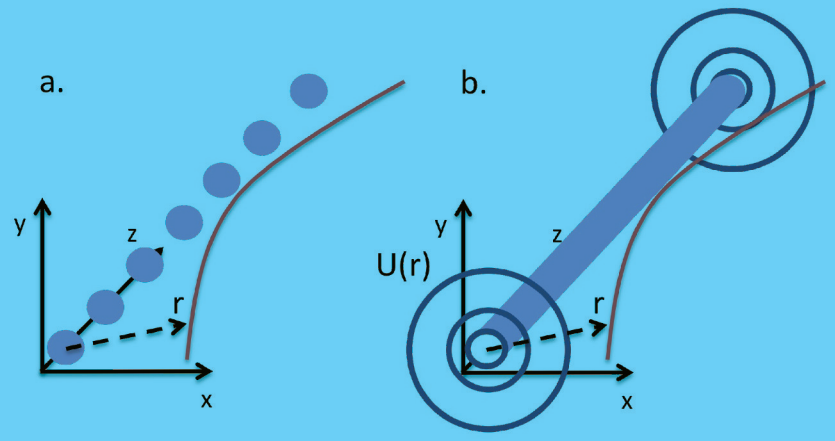

Figure 1.2: a. Trajectory of positive particle moving in a crystal aligned with respect to a crystal axis. b. Continuous potential $U(x)$ is felt by the particle mainly due to the neighboring axis

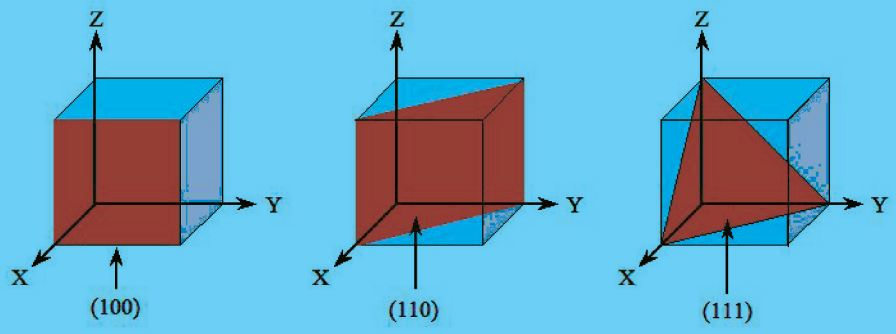

Figure 1.3: The main planes of the simple cubic lattice. The three orientations <100>, <110> and <111> are the respective direction normal to the planes.

If a charged particle moves in a crystal at low-angle with respect to a crystal plane, the potential can be approximated by the sum of the potential of the singles planes. In particular, the major contributions of the two nearest planes dominate. Thus, the potential results

$$U_{pl}(x) \approx U_{pl}(d_p/2 - x) + U_{pl}(d_p/2 + x) - 2U_{pl}(d_p/2) \tag{1.13}$$

where x is expressed in unit of the interplanar distance and $U(0) = 0$. In Fig. 1.4(a) the planar potential averaged over thermal vibration and the planar potential for the Lindhard and Moliére approximations are shown.

Most of the crystals used for channeling investigation in high energy experiments are made of silicon [23], and for some applications germanium, thanks to

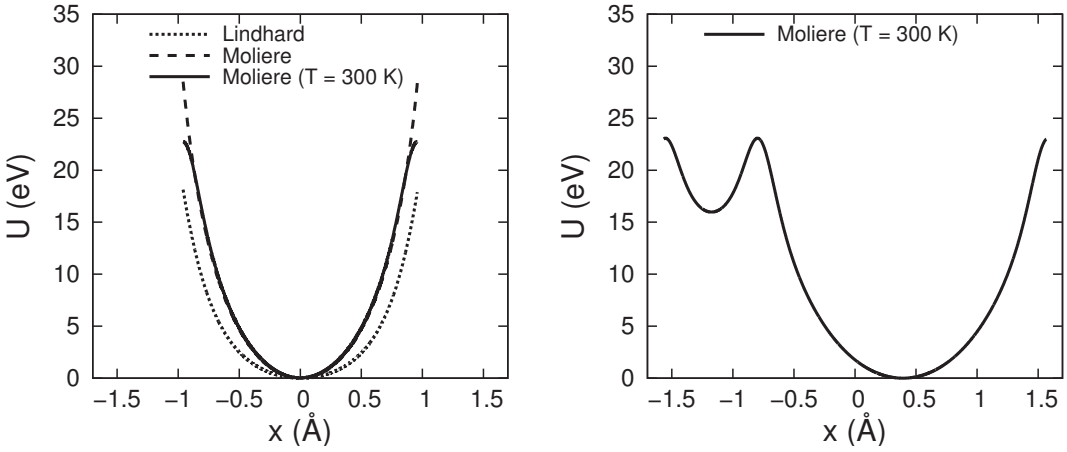

Figure 1.4: The planar continuous potential at 300 K by adopting the Moliére and the Lindhard screening functions and by averaging over thermal vibration using the Moliére screening function for the Si(110) planes (a) and for the Si(111) planes (b). Calculations were done with the ECHARM program [22].

Plane	d_p [Å]	a_{TF} [Å]	u_T [Å]	$U(x_c)$ [eV]	$U'(x_c)$ [GeV/cm]
(110)	1.92	0.194	0.075	16	5.7
(111)L	2.35	0.194	0.075	19	5.6
(111)S	0.78	0.194	0.075	4.2	3.5

Table 1.1: Parameters of some planar channels of silicon crystal. The potentials U are given at the distance $x_c = d_p/2 - 2u_T$ in the Moliére approximation.

the high standards reached by the semiconductor technology in terms of quality of the crystals. Silicon crystals belong to the diamond group and they are characterized by a covalent bond: each atom is linked to four neighbours forming a regular tetrahedron with a face centered cubic (fcc) crystalline structure. Figure 1.3 shows the principal planes of the fcc structure indicated by the Miller indices; the planes useful for channeling are (110) and (111), while (100) generates a comparatively smaller potential, therefore it is not the optimal one. In fig. 1.4 the interplanar potential U (x) for the (110) and (111) planes in silicon is shown: the (110) orientation has a regular structure with a single interatomic distance (d_p = 1.92 Å) that produces a potential well of about 22 eV; the (111) one is more complex as it is characterized by two different interatomic distances, a long one (d_L = 2.35 Å) and a short one (d_S = 0.78 Å), which give rise to a couple of potential wells, the deepest one being of about 25 eV. Table 1.1 summarizes the parameters of some planar channels of the crystal of silicon at room temperature.

1.1.3 Charged particles motion under planar channeling

A charged particle is considered to be in planar channeling when it is trapped in the potential well between two crystalline planes; this happens if the transversal component of the particle momentum (see Fig. 1.5) is not enough to overcome the barrier. In this condition, the particle experiences a series of correlated collisions; although these are quantum events, the particle motion can be described in the classical mechanics frame, thanks to the large number of energetic levels accessible in the interplanar potential. Indeed, in the harmonic potential approximation $U(x) = U_0\left(x\frac{2}{d_p}\right)^2$, the energy spacing between the levels results to be equal to $\hbar\left(\frac{8U_0}{d_p^2 M_0}\right)^2$, where M_0 is the oscillating mass. Therefore the classical approximation is valid if the condition 1.14 is fulfilled:

$$N_0 = \frac{d_p}{\hbar\sqrt{8}}\sqrt{U_0 M_0} \gg 1 \tag{1.14}$$

where N_0 is the number of the accessible energetic levels for the trapped particle. Condition 1.14 is always fulfilled for heavy particles (protons) while for light ones (electrons and positrons), the classical approach becomes valid in the 10-100 MeV range.

In the framework of the continuum approximation, the transversal momentum is much smaller than the parallel one ($p_t \ll p_l$) and thus the total energy of the system can be approximated as follows:

$$E = \sqrt{{p_x}^2 + {p_z}^2 + m^2c^4} + U(x) \simeq \frac{{p_x}^2c^2}{2E_z} + E_z + U(x) = const \tag{1.15}$$

where $E_z = \sqrt{{p_z}^2 + m^2c^4}$ is conserved, since the potential $U(x)$ does not depend on z; hence the transverse energy defined as $E_T = \frac{{p_x}^2c^2}{2E_z} + U(x)$ is conserved too. Being $p_x = p_z\theta$, and assuming $E_z \approx E$, $p_z \approx p$, using the known relation $pc^2 = vE$, where v is the particle velocity, we may rewrite E_T as:

$$E_T = \frac{pv}{2}\theta^2 + U(x) = const \tag{1.16}$$

Taking into account that $\theta = dx/dz$, Eq. 1.16 results to be:

$$E_T = \frac{pv}{2}\left(\frac{dx}{dz}\right)^2 + U(x) = const \tag{1.17}$$

Differentiating with respect to z and dividing all terms by θ, the result for the one-dimensional transverse motion in the potential $U(x)$ is:

$$pv\frac{d^2x}{dz^2} + \frac{d}{dx}U(x) = 0 \tag{1.18}$$

Equation 1.18 describes the particle transverse oscillation of the harmonic motion in the potential well under channeling condition. In the harmonic potential approximation $U(x) \simeq U_0\left(\frac{2x}{d_p}\right)$ the solution is a sinusoidal function:

$$x = \frac{d_p}{2}\sqrt{\frac{E_T}{U_0}}\sin\left(\frac{2\pi z}{\lambda} + \phi\right) \tag{1.19}$$

with the oscillation period being $\lambda = \pi d_p\sqrt{pv/2U_0}$.

The particle remains trapped within the channel if its transverse energy is lower than the maximum value of the potential barrier, i.e.:

$$E_T = \frac{pv}{2}\theta^2 + U(x) \leq U_0 \tag{1.20}$$

From Eq. 1.20, considering a particle with the maximum transverse energy ($E_T = U_0$) in the position of minimum value of the interplanar potential (i.e. $x = 0$, where $U(0) = 0$), one can obtain the maximum allowed misalignment angle for channeling

$$\theta_L = \sqrt{\frac{2U_0}{pv}} \tag{1.21}$$

θ_L being the critical angle introduced by Lindhard, for both planar and axial channeling independently of the particle charge's sign. When the incident angle of a particle with the channel direction is less than θ_L but close to the nuclei (as close as $\sim a_{TF}$), the scattering from the nuclei itself rapidly removes the particle from the channeling mode (sec. 1.1.4). For this reason a critical transverse coordinate for planar channeling of long crystals can be introduced:

$$x_c = \frac{d_p}{2} - a_{TF} \tag{1.22}$$

which leads to another common definition of the critical angle of channeling

$$\theta_c = \sqrt{\frac{2E_c}{p\beta}} \tag{1.23}$$

where $E_c = U(x_c)$ is the critical transverse energy. If a particle moves along the center line of a channel and has an incident angle with the channel direction less then θ_c we can neglect its escape from the channel and hence proper channeling takes place.

The calculations seen above with the harmonic approximation are valid in the case of motion of positively charged particles channeled between two crystallographic planes. For negative particles the planar potential is attractive and then, in the case of motion in channeling condition, the particles oscillate around

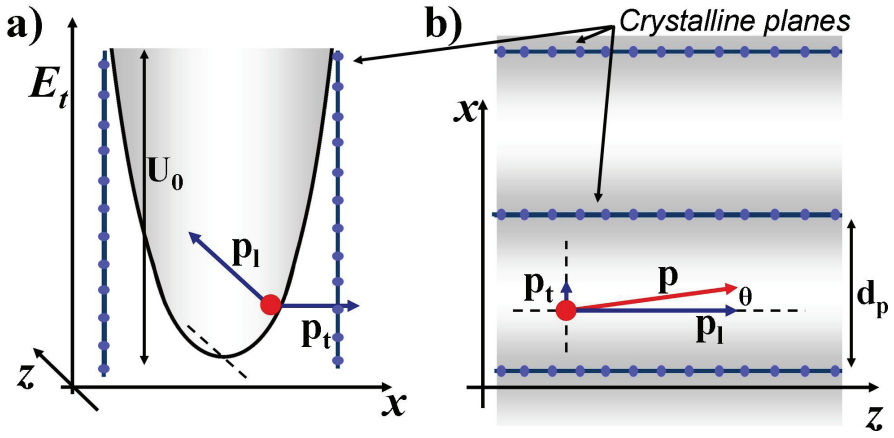

Figure 1.5: a)A positive particle bound in the interplanar continuous potential. b)Top view of the channel. Here are highlighted the components of the transverse (p_t) and longitudinal (p_l) momentum of the particle with respect to the plane direction. $\theta = p_t/p_l$ is the small misalignment angle with respect to the crystal plane.

the atomic planes (or axis), repeatedly crossing the dense layers of atomic nuclei. Therefore the probability of scattering with nuclei is higher with respect to positive particles, hence being higher the probability that the particle escapes from the channel. For this reason the dechanneling length for negative particles are much shorter than for positive ones. Fig. 1.6 shows the continuous planar potential for negative particles in the case of a silicon crystal oriented along the (110) planes; we can notice that U_{pl} is opposite to the one for positive particles. In any case, the depth U_0 does not change so $\theta_L = \sqrt{\frac{2U_0}{pv}}$ is the same for both positive and negative particles.

1.1.4 Dechanneling

Channeled particles motion is affected by incoherent scattering processes with electrons and nuclei, that cause the non-conservation of the transverse energy E_T due to the contribution of the random angle in a single event of scattering. As a result, E_T may become higher than the potential barrier, thus the particle comes out from the channel. This process is normally referred as "dechanneling". In the depth of a crystal, as well as some particles leave the channeling mode, there may be particles entering the channeling mode, thus experiencing a "feeding in" process. The mechanisms responsible for these two opposite processes are essentially the same.

Dechanneling may be caused by the multiple quasi-elastic scattering with nu-

clei or by the multiple inelastic scattering with electrons. For positive particles, the fraction of particles impinging on nuclei are rapidly dechanneled. In fact, particles captured in the potential-well with $E_T > E_c$ quickly leave the channeling mode due to the multiple Coulomb scattering with nuclei. On the contrary, channeled particles entering in between atomic planes experience soft collisions mostly.

These differences lead to the development of the "modern" description of particle dynamics and of dechanneling. The scattering during motion of positive channeled particles can be treated with the formalism of a diffusion theory, which led to the "classical" definition of dechanneling. This old definition was recently renamed "electronic dechanneling" as the process of expulsion of particles impinging close to nuclei was classified as an alternative dechanneling mechanism, referred as "nuclear dechanneling". This last mechanism was then associated also to negative particles dynamics in crystals, thus giving some important hints to the study of coherent interactions of negative particles. More details about particle dynamics and dechanneling are given in the following subsections and in the references therein.

Dechanneling in long crystals

In the depth z of a long crystal the fraction of channeled particles decreases exponentially

$$N_{ch}(z) \approx N_s e^{-z/L_e} \tag{1.24}$$

where N_s is the number of particles in stable channeling state at the crystal entry face ($z = 0$), N_{ch} is the number of channeled particle, L_e is the electronic dechanneling length, which scales with the particle momentum [24]. If a channeled particle has a transverse energy $E_T \leq E_c$ (far from nuclei), it is affected by multiple scattering with electrons. Because the electronic density is rather uniform in the channel, owing to valence electrons, the process is independent from the transverse position x of the particle but only depends on E_T. This process is slower than the one due to the strong nuclear collisions. The electronic dechanneling length for positive particles has been extensively measured in experiments [14, 25, 26].

The non-conservation of transverse energy E_T for soft interactions in long crystals can be treated though the diffusion theory, as fully described in Ref. [2]. This theory led, through several approximations, to the formula for electronic dechanneling:

$$L_e = \frac{256}{9\pi^2} \frac{p\beta}{\ln(2m_e\gamma/I) - 1} \frac{a_{TF} d_p}{Z_2 r_e m_e} \tag{1.25}$$

where m_e and r_e are the mass and the classical radius of an electron, I is the mean ionization energy and γ is the Lorentz factor.

Dechanneling in short crystals

The advent of shorter crystals allowed the observation of particle dechanneling due to multiple scattering on the atomic nuclei of the crystal. As one can see in Fig. 1.6, particles impinging close to the atomic planes are found in unstable channeling states and are dechanneled by nuclei traversing a short distance in the crystal. This effect is referred as "nuclear dechanneling". As shown in Ref. [27], with the aim to estimate the fraction of positive particles suffering nuclear dechanneling, the atomic density was assumed to have a Gaussian distribution with standard deviation equal to the atomic thermal vibration amplitude, u_t, which is 0.075 Å for Si at 273 K [2]. By assuming that the atomic density region interested by intense multiple scattering extends over 2.5σ [27] - the so-called nuclear corridor - (see Fig. 1.6) and bearing in mind that (110) interplanar distance is $d_p = 1.92$ Å, about 19.5% of particles ($5u_t/d_p \approx 0.195$) of a perfectly parallel beam were estimated to be under unstable channeling state. The strengths of dechanneling by electrons and nuclei are quite different. As an example, for 400 GeV/c protons interacting with Si (111) planes, $L_e \sim 220$ mm [23], while $L_n \sim 1.5$ mm [27], L_e and L_n being the electronic and nuclear dechanneling lengths, respectively. Dechanneled particles are found in over-barrier states and the probability to be rechanneled is negligible for a bent crystal. Dechanneling processes lead to a decay in the number of channeled particles, which can be approximated by exponential functions. The number of channeled particles at coordinate z, $N_{ch}(z)$, over the total number of particles, N_0, holds:

$$N_{ch}(z) \approx N_u e^{-z/L_n} + N_s e^{-z/L_e} \tag{1.26}$$

where N_u and N_s are the number of particles in unstable and stable channeling states at the crystal entry face ($z = 0$), respectively. For Si (110) at 273 K, $N_u \sim 19.5\% N_0$ and $N_s \sim 80.5\% N_0$.

Dechanneling of negative particles

The results obtained for the nuclear dechanneling of positive charged particles gave a fundamental input in the research of coherent effects for negative particles in crystals.

Channeling of negative particles is of special interest in view of some applications, such as beam manipulation [28–30], production of high-energy radiation in both unbent [23] and bent [31, 32] crystals, in crystalline undulators [33–35],

and as a positron source [36, 37]. The development of such applications does require a higher understanding of the contribution of incoherent interactions between channeled particles and crystals [38], in view of designing crystals with optimized geometrical parameters.

Comparatively to positive particles, experimental knowledge about channeling of negative particles had been limited due to the lack of high-energy non-radiating beams of negatively charged particles and experimental difficulties to fabricate suitable crystals. Indeed, only few years ago the possibility to steer negatively charged particle beams (in this case, 150 GeV- energy pions), through bent crystals was demonstrated at CERN [39–41]. In fact, due to incoherent interaction with the atoms, negative channeled particles have a higher probability to suffer dechanneling [2, 27] with respect to their positive counterpart. As a direct consequence, the number of particles leaving the channeling state per unit of length is higher for negative particles than for the positive ones.

For negatively charged particles, since the minimum of the potential well is located on the atomic planes, all the particles are readily directed toward the nuclear corridor. As a consequence, all negatively charged particles lie in unstable channeling states ($N_s = 0$, $N_u = N_0$) and the mechanism of dechanneling via interaction with valence electrons negligibly contributes to dechanneling with respect to nuclear dechanneling. The experimental study reported in Ref. [42] showed that the dechanneling length for negative particles is comparable to the nuclear dechanneling length for positive charges, therefore, in this case the number of channeled particles holds:

$$N_{ch}(z) \approx N_0 e^{-z/L_n} \tag{1.27}$$

In Ref. [42] it was also showed that nuclear dechanneling length is not proportional to pv, in contrast with theory used for dechanneling in long crystals [2]. New models were proposed, and experimental data with 400 GeV/c protons highlighted once again the needing of a most accurate model for the description of nuclear dechanneling with respect to the theory used for long crystals [43]. The study of dechanneling length is still an open issue, and my group at the moment is involved in this research.

Figure 1.6 shows the averaged potential (calculated as in Ref. [22]) experienced by the particles channeled between (110) silicon planes, and the compared dynamics of 150 GeV/c pions with opposite sign.

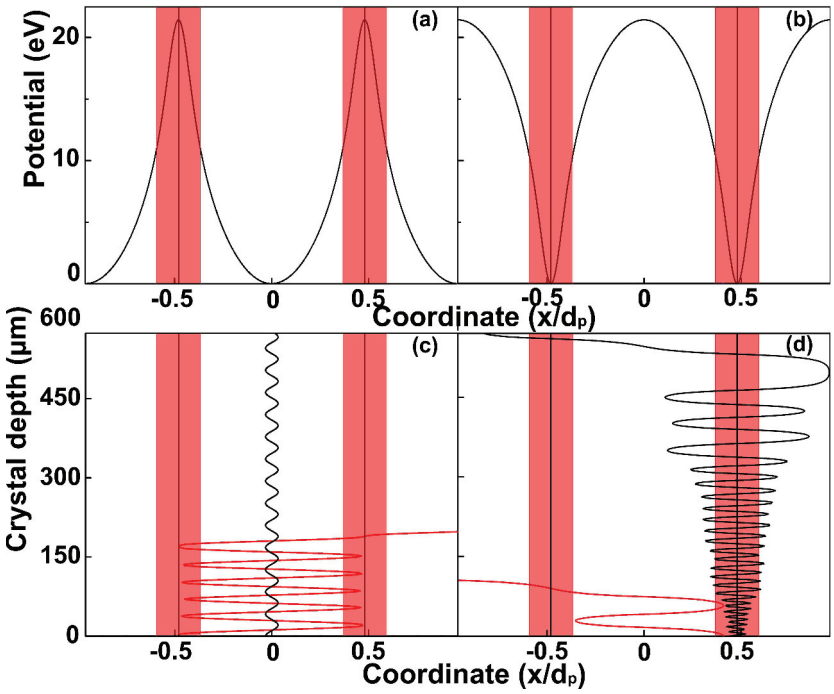

Figure 1.6: (a-b) planar potentials experienced by π^+ and π^- channeled between (110) silicon planes. Shaded regions highlight the regions of high nuclear density (nuclear corridors), vertical lines inside those regions show the positions of atomic planes. (c) Trajectories of two 150 GeV/c π^+: the trajectory of the particle with larger oscillation amplitude is for a particle whose impact parameter lays inside the region of high nuclear density (i.e. the particle is in unstable channeling state). Such a particle is dechanneled after traversing a short distance in the crystal. The other trajectory refers to a particle impinging far from atomic planes (such particle is in stable channeling states). (d) trajectories of two 150 GeV/c π^-: all negative particles pass through the high-atomic density regions and are subject to nuclear dechanneling. Adapted from ref. [42].

1.2 Coherent Interactions in Bent Crystals

1.2.1 Particle Motion in Bent Crystals

As suggested by Tsyganov in 1976, a slightly bent monocrystal could be used for steer a charged particle beam [13, 44]. In particular, channeled particles would follow the direction of the bent atomic planes (or axes), thus deviating from the initial direction by an angle equal to the one determined by crystal bending.

The motion of a positive particle within a bent planar channel can be described assuming that if the crystal has a macroscopic curvature radius (i.e. of the order of several meters), bending has no effect on the potential of the crystal

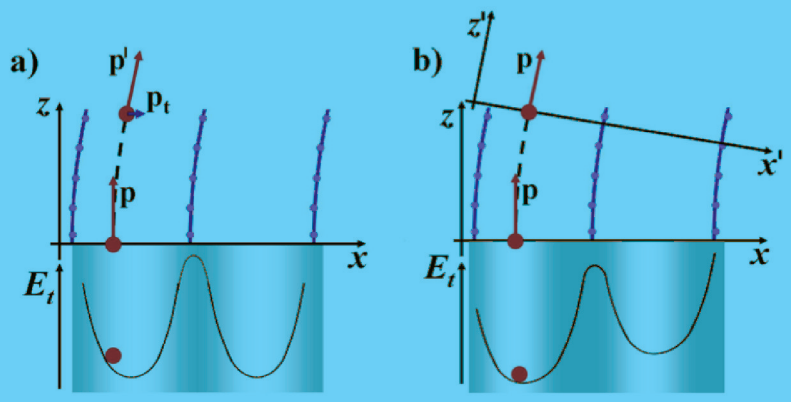

Figure 1.7: Scheme of the channeling motion of a positive particle particle that enter in the channel aligned with respect to the crystal planes: a) in the laboratory inertial frame; b) in the non inertial comoving reference system which rotates with the particle; the centrifugal force appear

lattice in the range of angstroms in the laboratory inertial frame. On the contrary, from the point of view of non-inertial reference frame (i.e. comoving with a particle channeled with zero transverse momentum along the bent planar channel) a centrifugal fictitious force appears due to the crystal deformation. Figure 1.7 shoes a scheme for this two reference frame: Fig. 1.7.a) represents the motion of a channeled particle in the laboratory; Fig. 1.7.b) describes the motion in the non-inertial comoving reference frame. In case a) the particle enters in the channel aligned with respect to the crystal planes, with $p_t = 0$, but in order to follow the channel bending in the evolution of motion, the particle acquires a non-zero transverse momentum; so the interplanar continuous potential exerts a force on it which modifies the particle momentum. Instead in case b) the particle momentum direction does not change, but a centrifugal force directed towards the external side of the channel appears.

In the comoving frame, the equation of motion 1.18 for a channeled particle becomes:

$$p\beta\frac{d^2x}{dz^2} + U'(x) + \frac{p\beta}{R(z)} = 0 \tag{1.28}$$

where x, z are the particles coordinates in this frame and $1/R(z)$ is the local curvature of the channel. If the bending radius R is independent of z, the particle moves as if it was in an effective interplanar potential of the form:

$$U_{eff}(x) = U(x) + \frac{p\beta}{R}x \tag{1.29}$$

with a transverse energy $E_T = \frac{p\beta}{2}\theta^2 + U_{eff}(x)$.

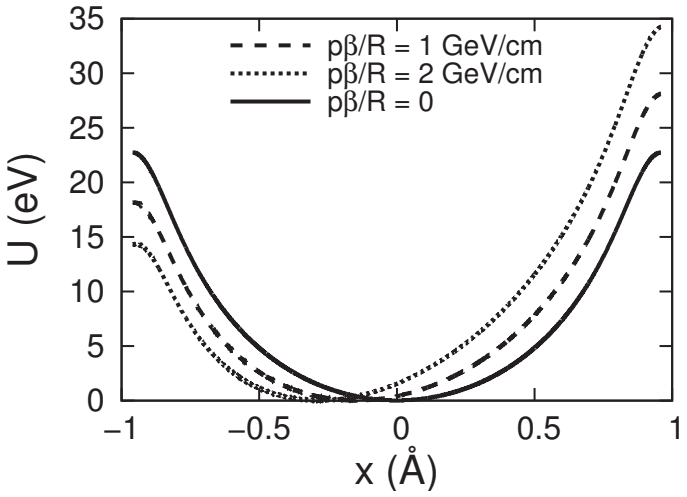

Figure 1.8: The interplanar potential in Moliére approximation for Si (110) (solid line) and the effective potential for $p\beta/R$ of 1 GeV/cm (dashed line) and 2 GeV/cm (dotted line). Calculations were done with the ECHARM program [22].

In Fig. 1.8 some examples of the potential $U_{eff}(x)$ for different ratios $p\beta/R$ in comparison with the undisturbed potential $U(x)$ for the Si planes (110) are shown.

As one can see, as the ratio pv/R increases, the depth of the effective potential well decreases and its minimum value is shifted towards the atomic plane; thus at some critical $(pv/R)_c$ the well disappears and channeling is no longer possible. The critical bending curvature is defined by the maximal interplanar electric field ε_{max} near the atomic plane.It is possible to define a critical radius R_c:

$$R_c = \frac{p\beta}{e\varepsilon_{max}} \tag{1.30}$$

According to Biryukov we should use $U'(x_c)$ instead of $e\varepsilon_{max}$ and so redefine R_c

$$R_c = \frac{p\beta}{U'(x_c)} \tag{1.31}$$

Moreover the critical energy in the case of bent crystal is $E_c(R_c/R) = E_{c,0}(1 - R_c/R)^2$, where E_c is the critical transverse energy in the straight crystal. In this way, it is possible to define a new critical angle $\theta_c(R_c/R)$ for bent crystals:

$$\theta_c(R_c/R) = \theta_{c,0}\,(1 - R_c/R) \tag{1.32}$$

where $\theta_{c,0} = \sqrt{2U_c/(p\beta)}$ is the critical angle of channeling for a straight crystal. From Eq. 1.32 we can notice that θ_c is reduced from a factor $(1 - R_c/R)$ with respect to straight crystals.

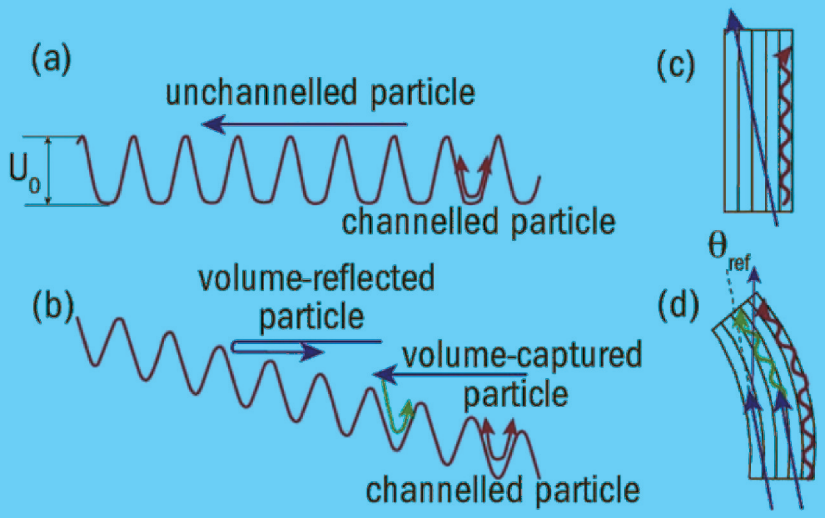

Figure 1.9: (a)-(c) Channeled and unchanneled particle in a straight crystal; (b)-(d) particle in channeling, VR and VC conditions in a bent crystal [49].

1.2.2 Quasichanneling

When a particle moves in the crystal volume with a transverse energy higher than the planar potential barrier, but with small angle to the atomic planes ($\theta > \theta_c$), it experiences the influence of the continuous potential, thus resulting in some kind of particle dynamics being possible only in bent crystals. This type of particles are called quasichanneled particles or above-barrier particles [45–47].

For quasichanneled particles two different effects have been discovered, the volume capture (VC) [48] and the volume reflection (VR) [18]. In Fig. 1.9 the different effects due to influence of the continuous planar potential, in case of straight and bent crystal, are schematically shown. Fig. 1.9(a)-(c) represents a schematic depiction of motion for an unchanneled particle and a channeled one in a straight crystal in the plane (x, E_T) (a) and in the plane (x, z), (c); instead in Fig. 1.9(b)-(d) the motion of positive particles in channeling, VR and VC conditions is shown in the planes (x, E_T) and (x, z). In next paragraphs this two effects will be described in more detail.

Volume Capture

As anticipated in Sec. 1.1.4, as well as particles may leave the channel, there could be particles entering in the channeling mode: this process, called feeding in, is expected since for any trajectory of a particle in a crystal a time-reversed trajectory is possible. In straight crystals, these two opposite effects are due to scattering processes: the first one is the transition of a particle from the channeled

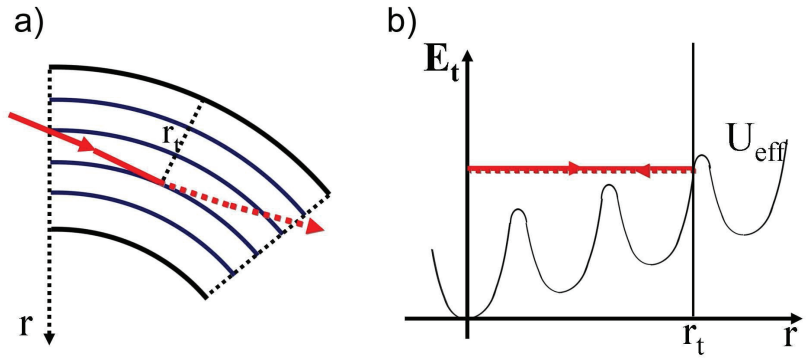

Figure 1.10: Reflection of a charged particle in the crystal volume at the rotating radial coordinate r_t: a) schematic depiction of volume reflection; b) phase space of the particle transversal energy as a function of the radial coordinate [31].

beam to the random one ('over barrier'), instead the second describes the transition where a random particle could be captured into a channeled state. According to Lindhard's reversibility rule [12], the probability of this two opposite transitions is the same.

Volume capture is the feed-in process of channeling in bent crystal [15, 50]. Some particles of the beam may be captured in planar channeling conditions because in the region of tangency with the bent planes VC becomes possible for any unchanneled particle. As a result VC in bent crystals is more efficient than the feeding-in mechanism in straight ones, so we expect that the feed-out mechanism increases according to the reversibility rule. In fact, in comparison with the case of straight crystals, the dechanneling probability is higher because the potential well E_c and in turn the critical angle θ_c are lower. Moreover we can notice that the probability for dechanneling (volume capture) depends strongly on the bending radius: it is higher at higher curvatures. Such effect takes place even without an account of incoherent scattering. In addition, at higher energy this effect becomes more noticeable for both positive and negative particles (see Ref. [51]).

Volume Reflection

When a quasichanneled particle moves through a bent crystal in approximation of continuous planar potential, it can be deflected on average in a direction opposite to the one of the crystal bending by an angle of order $\sim \theta_L = \sqrt{2U_0/pv}$ with a small spread. This means that in a bent crystal the average exit angle of unchanneled particle is not equal to the average incident angle.

In the depth of a bent crystal it can happen that particle trajectory becomes tangential to the crystallographic planes, thus tangent to the planar potential,

because of the curvature of the planes (see Fig. 1.10.b)). This condition can be fulfilled in a broad angular range in the volume of the crystal. The angular acceptance is equal to the bending angle of the crystal, which is equal to l/R, being l is the crystal length, since bent crystal exposes such a continuous interval of angles to incoming beam.

For a bend radius $R \gg R_c$, the volume reflection angle for positive particles is $\theta_{VR} \approx 2\theta_c$, while for negative particles is smaller, because of the different shape of the effective interplanar potential [52]. The reflecting points for a negative particle are more flat so that they accomplish a longer path near turning points with respect to positive particles (see Fig. 1.6).

For smaller R, i.e. when $R \gg R_c$ is not valid, the deflection angle θ_{VR} is just below $2\theta_c$, because a higher crystal curvature allows the reflection to occur in points in which the interplanar potential is less intense. In this case the efficiency grows due to the increase of the reflective area. This case is described in detail in Ref. [53]. In comparison with channeling, VR has a greater angular acceptance, but it provides a smaller angular deflection, since $\theta_{VR} \sim \theta_L$. In addition, VR efficiency is higher at a higher curvature, because the competitive mechanism of VC has a higher probability at lower curvature. Moreover, since the volume capture probability scales as $E^{-2/3}$, VR efficiency increase with E. All the peculiarities just described made the interest onto VR growing significatively in view of applications in high energy physics, as an attractive alternative to channeling.

To give a comprehensive overview of coherent effect in a bent crystal, we can consider the crystal orientation angle θ_0 and the deflection angles of particles θ_x being counted from the direction of the incident beam axis and the initial direction of the particle momentum, respectively. The direction to the crystal bend side is defined as a positive one. When the crystal orientation angles $|\theta(r)| < \theta_c$ the beam particles can be captured into the channeling regime at the crystal entrance, where θ_c is the critical angle for channeling. VR of particles is realized when the orientation angles are in the interval $-\alpha < \theta_0 < -\theta_c$. The particles volume captured into the channeling regime near the tangency point can follow by the bent channels and be deflected by the angles up to $\alpha - |\theta_0|$.

By considering a positive particle beam interacting with a bent crystal, a VR deflection angle $\theta_{vr} = 1.4\theta_c$ μrad is obtained. The distribution has tail stretched to the bend side, which is produced by particles captured into the channeling regime in the tangency area. Some part of volume captured particles quickly leaves the channeling regime due to the same multiple scattering but others pass by the bent channels up to the crystal exit. The VR efficiency P_{vr} is the beam part shifting as a whole with the deflection angles $\theta_x < \theta_b = \theta_{vr} + 3\sigma_{vr}$, where θ_b is the boundary between the reflected beam and particles volume captured into the channeling states. The value of the volume captured beam part determines the

VR inefficiency $\epsilon_{in,vr} = 1 - P_{vr}$.

Multi Volume Reflection in Multi-Crystals

The deflection angles of particles due to volume reflection are comparatively small with respect to channeling, and becomes even smaller at higher energies. A possibility to increase the particle deflection angles using the sequence of a few short bent crystals working in the regime of VR has been studied recently [28, 54, 55]. The sequences of two and five quasi-mosaic crystals and the multi-strips joint by a single frame were used in these studies, respectively. It was shown that the beam deflection angles increase proportionally to the number of the sequence crystals.

The beam deflection efficiency by the crystal sequence should decrease with increasing the number of reflections because of the beam fractions volume captured into the channeling states in each of the crystals. The beam deflection efficiency due to multiple volume reflections (MVR) in N crystals can be estimated in the first order approximation of independent events as

$$P_{mr}(N) = P_{vr}^N = (1 - \epsilon_{vr,in})^N \approx 1 - N\epsilon_{vr,in} \tag{1.33}$$

However, the measured deflection efficiency is higher. Fig. 1.11 helps to understand the situation. The beam part marked 1, which was only considered for the estimate (1), makes two subsequent reflections with the mean angle θ_{vr} passing two bent crystals and obtains the mean deflection angle $2\theta_{vr}$. A smaller beam part 2 is volume captured in the first crystal but has a tangency point with the bent planes in the second crystal. Here many of the particles 2 are reflected obtaining the mean deflection angle θ_{vr}. So, particles volume captured in one of the sequence crystals also participate in the multiple volume reflection but they obtain a smaller deflection.

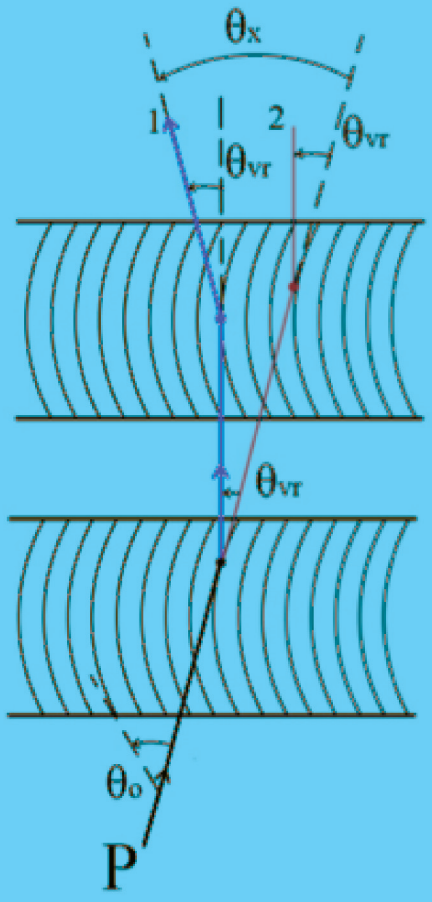

Figure 1.11: Schematic picture of the sequence of two bent crystals with the particle trajectories. 1 - a particle having volume reflections in both crystals near the tangency points with bent planes. 2 - a particle volume captured in the first crystal and then volume reflected in the second one (for a simplicity the trajectory part after VC is shown by red as a prolongation of the trajectory before VC). θ_0 is the crystal orientation angle, θ_x is the deflection angle of the particle 1, θ_{vr} is the VR deflection angle.

Chapter 2

Fabrication and bending of crystals for channeling

Channeling of high-energy particle beams in bent crystals has progressed significantly in the past due to the advent of new schemes and techniques in the production of crystals.

Since the first generation of high energy channeling experiments, dated in the 80's, [5, 56–58], silicon was employed as prime material because it is commercially available as high-quality single crystals, which are obtained via melting-growing methods [59] and present a very low dislocation density and low contaminant concentration. First prototypes were some centimetres thick along the beam, and were bent by means of mechanical devices. The primary bending imposed to the crystal was used for particle beams manipulation. Despite of the simplicity of this geometry, some important limitations manifested soon, for instance the impossibility to reduce crystal length below few centimetres, as well as the rather high non-uniformity of bending radius.

With the aim of realizing shorter crystals, and to provide a more uniform bending radius, a second generation of bent crystals was proposed. Secondary bending, which accompany the main imposed primary bending, were employed to steer charged particles. Among them, the "anticlastic deformation" (AD) was exploited to realize strip-like crystals [60], while the "quasi-mosaic" (QM) effect was used to realize quasi-mosaic crystals [61]. Secondary curvatures are a fraction of the imposed main one, therefore they result to be more easily and precisely adjustable. As further advantage, the usage of secondary bending, which arises also in regions of the crystals not in contact with the bending device, allowed the realization of mechanical holders which can be placed far from the particle beam. Moreover, secondary bending can be imparted in a shorter dimension with respect to the principal one, thus allowing the realization of crystals far shorter with respect to first generation crystals. Together with crystal geometries, innovative preparation

techniques were developed in order to obtain crystals with surfaces of higher quality [62–65]. As an alternative scheme, to deflect a charged particles beam, straight crystals whose thickness is half of the oscillation length for planar channeling can be used. For this purpose, micrometric and nanometric flat membranes were produced and tested [66–68].

In most recent years, the techniques of fabrication and bending technologies were further optimized. This led to the fabrication of a silicon strip crystal suitable for the collimation of LHC for the UA9 experiment [4], first long strips prototypes for parasitic extraction of high energy beams in the framework for the CRYSBEAM project, a silicon multistrip optimized for the collimation in the SPS, silicon quasimosaic crystals for studying particle dynamics and accompanying radiation emission of sub-GeV and GeV electrons at MAMI [69–71] and SLAC [72], and silicon membranes for correlations studies with sub-GeV electrons. In this chapter, state-of-the-art techniques in crystal fabrication, bending and characterization will be shown. Part of the techniques were already presented in Ref. [73], whose this thesis represents the continuation.

2.1 Strip-like silicon crystals manufacturing

Strip-like crystals were successful employed in channeling experiment in the last decade. Typically, crystals for channelling were diced from a wafer or ingot through either a mechanical cut or a laser beam. Both methods introduce lattice imperfections such as dislocations or amorphization of the crystal surface. In the case of mechanical dicing, the extension of the damaged area is of the order of the grit size of the diamond powders in the blade and may extend deep into the crystal by several micrometres, while a laser cut may induce remelting and fast cooling of the edges leading to the presence of amorphous layers. The damaged layer has a detrimental effect since it does not act as an active layer for channeling. First specimens were fabricated via mechanical dicing of all crystal surfaces, both normal (entry face) and parallel to the beam direction [74]. The Ferrara group introduced a method for isotropic chemical etching to remove the portion of the crystal damaged by the cut [62–64] and then an alternative procedure relying solely on chemical methods such as photolitography and anisotropic wet etching [65]. Such methods were borrowed from micro-fabrication techniques of silicon, and revisited and adapted to the case of sample preparation for channeling. First prototypes prepared by the Ferrara group with such methods were already fully characterized and tested, as reported in articles together with fabrication methods [62–65].

Up to now, the elective application of bent crystals in accelerator physics is the crystal-assisted collimation of the beam circulating in the LHC. This requires crystals of very high quality both in bulk and surfaces, and very finely adjusted

parameters (i.e. length and bending radius). In order to make strip crystals a good candidate for the collimation in LHC, the techniques for fabrication and characterization were furthermore optimized.

For instance, the flatness of the parallel face and the miscut, which is the angle between the optical surface and crystalline planes, required to be strongly improved. To accomplish this request, a method for the precise characterization of the miscut of starting silicon wafers, consisting of using a high resolution X-rays diffractometer together with a custom autocollimator, was developed. After that, the finest available polishing technique of optical surfaces, accompanied with a strong reduction of the miscut, was done via a high precision magnetorheological finishing technology, in collaboration with the QED Technologies company.

A new generation of holders was designed. The longest dimension of strips was reduced from 70 mm to 55 mm. This allowed the usage of 4 inches starting wafers, which can be machined more easily with respect to 6 inches wafers, as well as a significant reduction of dimension and weight of crystal within the holder. New materials were employed to realize the holder, for instance titanium, due to compatibility constraint with the ultra-high vacuum of the LHC pipe. Moreover, the clamping system and the mechanism to reduce torsion via screws were optimized.

Characterization method were also improved. The long-term used white light interferometry for surface characterization was supported by the already mentioned X-rays diffractometer together with autocollimator. The diffractometer was also used to directly measure principal bending, anticlastic bending and torsion, thanks to purposely designed mechanical supports for mounting bent crystals onto the cradle. A new infrared light interferometer was used to map the thickness of the starting wafers with nanometric precision, as well as to measure the length along the beam of the strips.

All the fabrication and characterization methods will be presented in details in this section.

2.1.1 Surface treatments

As described in Ref. [75] and shown in Fig. 2.1, channeling, and thus extraction and collimation, is possible only if beam particles hit the crystal with an impact parameter b large enough to overcome possible surface imperfections, and with an angle b' small enough to be within the critical angle for planar channeling. For the case of LHC, critical angle for planar channeling was found to be 1.8 μrad for 7 TeV protons in Si (110) planes. As a consequence, the surface roughness R_A of the lateral face of the crystal (i.e. the face parallel to beam direction) is required to be lower than the impact parameter of the beam halo ($\sim$ 100 nm for LHC). As well as the surface roughness, the quality of the cutting is a crucial parameter. In particular, the miscut angle, which is the misalignment between orientation of

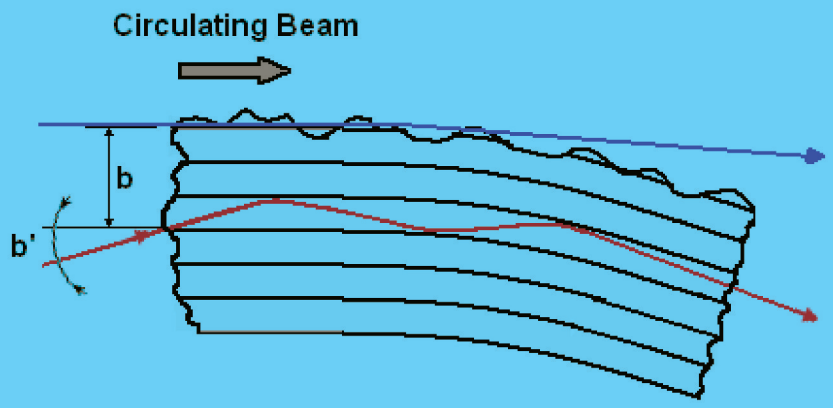

Figure 2.1: Schematic (not to scale) of the application of crystal for beam steering. The impact parameter b and the impinging angle of beam b' are shown. The surface roughness R_a of the lateral face of the crystal (parallel to beam direction) is required to be lower than the impact parameter b ($\sim$ 100 nm for beam halo of LHC) for beam steering using the channeling effect.

Figure 2.2: Crystal planes indicating preferred (a) and unwanted (b) miscut.

the optical wafer surface and the crystallographic planes, should be very low, in order to increase the crystal portion available for channeling and to facilitate the optical pre-alignement of the crystal with respect to the beam. The miscut can have positive or negative angles with respect to the planes (see Fig. 2.2), where the latter is very undesirable, because channeled particles can leave the crystals without passing the full length and therefore experience a smaller bending angle. The role of miscut have been better understood in very last years, thanks to the validation of simulations within an experiment of crystal-assisted collimation in the SPS. For instance, a strip crystal with a miscut of 200μrad doubled the beam loss with respect to a crystal with no miscut, while keeping above 90% channeling efficiency [76].

Preliminary low-miscut wafer selection Wafers with the lowest available nominal miscut ($<$ 0.01 °) of the double-sided polished surfaces are provided by

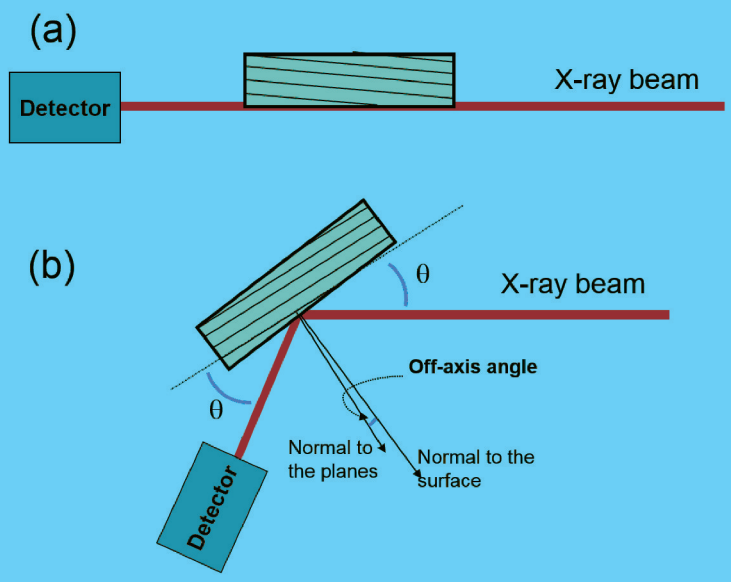

Figure 2.3: Scheme of the setup and the method for miscut characterization with high resolution X-rays diffractometer, aimed to the preliminary selection of low-miscut wafers. The surface is aligned with respect to the beam (a). Signal from a Bragg plane reflection is found when the sample is rotated by the miscut angle (b).

semiconductor materials manufacturers. A preliminary measurement of the miscut is done with a high resolution X-rays diffractometer (Panalytical X'PERT^3 MRD XL) in order to do a pre-selections of wafers with a miscut lower than 100 μrad for the successive steps of strip production. The procedure is shown in Fig. 2.3. In more detail, a collimated X-rays beam with low divergence is delivered forward to the triple-axis proportional detector. The wafer is mounted onto a high precision goniometer with 3 linear and 3 angular degrees of freedom, and placed in a position where the beam is partially intercepted. The optical surface is aligned to the beam by finding the angular positions where the detected signal is at the maximum. From this reference position (Fig. 2.3.a) , crystal and detector are rotated according to the condition for Bragg diffraction (i.e. $2d \sin\theta = n\lambda$, where d is the interplanar distance, n is a positive integer, and λ is the wavelength of incident wave). From this position, the signal from a Bragg plane will be found rotating the crystal of an angle corresponding to the miscut angle (Fig. 2.3.b). Such a measurement presents a very low casual error, being angular steps of mechanical movements very low. However, a comparatively high systematic error affects the measurement. This is caused by mechanical plays of the goniometric motors, which arise in moving the sample from the alignment position to the Bragg position. Mechanical plays of different motors may be also coupled. Moreover, due to the not

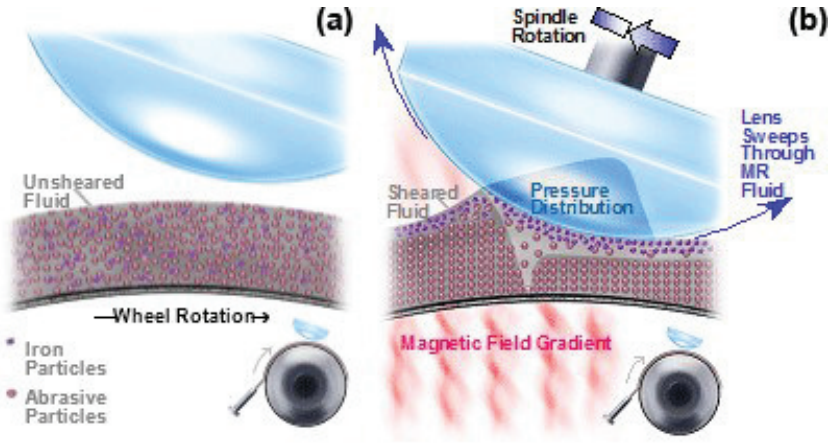

Figure 2.4: (a) Creation of MRF polishing "spot". With the magnetic field off, there is a random distribution of iron and abrasive particles in the ribbon of fluid being transported by the rotating wheel. (b) When the field is turned on, the iron particles align and form chains giving to the fluid structure and stiffness. In addition, the water and abrasives moves to the surface because the iron particles are attracted toward the wheel. When the workpiece is inserted into the fluid, the converging gap creates a highly sheared fluid layer that removes material with very low normal forces acting on the individual abrasive particles. Courtesy of P. Dumas.

perfect flatness of wafer surface, miscut also varies along the surface, for instance a total thickness variation of 2 μm over the area of a 4-inches wafer may cause a miscut uncertainty of few tens μrad. The first step proposed for miscut reduction is the flatness improvement of the starting wafer, as shown in next paragraph.

Magnetorheological Finishing (MRF) MRF is a precision polishing method developed by QED Technologies (QED). It is a deterministic finishing process that has the demonstrated ability to produce optical surfaces with an accuracy better than 30 nm peak to valley (PV) and surface micro-roughness less than 1 nm rms on optical glasses, single crystals (such as calcium fluoride and silicon), and glass-ceramics over areas as large as few mm^2.

The MRF process is based on the use of magnetorheological fluid, whose unique property is that its viscosity changes by several orders of magnitude when introduced into a local magnetic field, essentially turning from a liquid to a quasi-solid in milliseconds. In QED's use of this property, the fluid is pumped onto and around a rotating spherical wheel, with the wheel acting as a conveyor of sorts. The fluid forms a "ribbon" on the wheel, and as the ribbon passes through an area in which a local, high intensity, magnetic field has been created, its viscosity greatly increases. By introducing the surface to be polished into this high

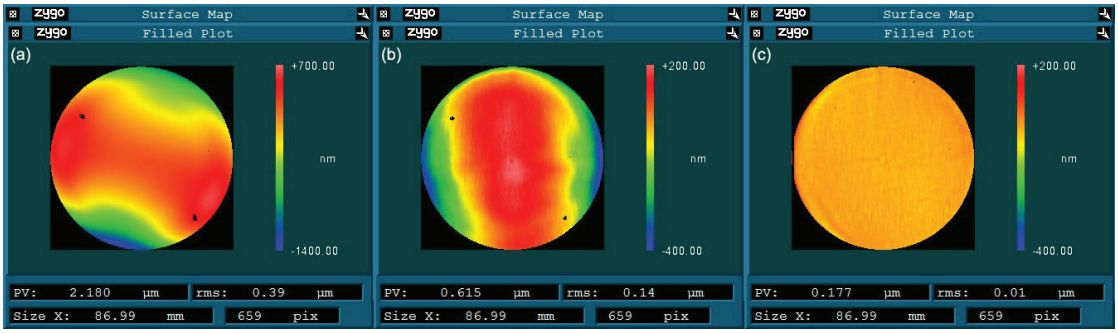

Figure 2.5: (a) Interferometric characterization of wafer surface prior to polishing operations shows surface flatness of 0.39 μm. (b) After a first polishing run with a high removal rate MRF fluid surface flatness is improved to a value of 0.14 μm. (c) After a second polishing run using a low removal rate fluid, surface flatness improves to only 0.01 μm. Courtesy of P. Dumas.

viscosity area, local, shear-based material removal can be created. By controlling the shape and other parameters that affect the removal, QED can create a sub-aperture polishing tool and deterministic process that has long term stability and relatively high removal rates on most optical materials. Coupling this with empirically proven algorithms, software code, and a refined graphical user interface, QED provides a user-friendly, production-worthy machine that is capable of finishing optical components to the most stringent tolerances, virtually regardless of size, shape or geometry.

With the aim to improve surface flatness while keeping the crystalline quality unaltered, we conducted a deep and definitive study of the surface of silicon wafers treated through MRF polishing. Pre-selected silicon wafers were polished in order to improve flatness from 0.39 μm (rms) to 0.01 μ (rms) over an aperture of 87 mm diameter. MRF polishing were carried in two steps. In the first polishing step the wafer were treated using a fluid capable of a high removal rate, this reduction of surface rms to 0.15 μm. In a second step, a fluid offering a lower removal rate fluid were used, bringing the surface flatness to the final value of 0.01μm. Before and after each polishing step flatness were measured with a Zygo interferometer operating in Fizeau configuration. see figure 2.5.

The crystalline quality of the treated surface has been characterized by means of high-resolution x-ray diffraction (HR-XRD) and Rutherford back scattering in channeling mode (RBS-c). Such techniques, well established for the determination of crystalline quality, highlighted the absence of any lattice damage induced to the silicon wafer, demonstrating the possibility to apply MRF polishing to delicate substrates as silicon wafers are.

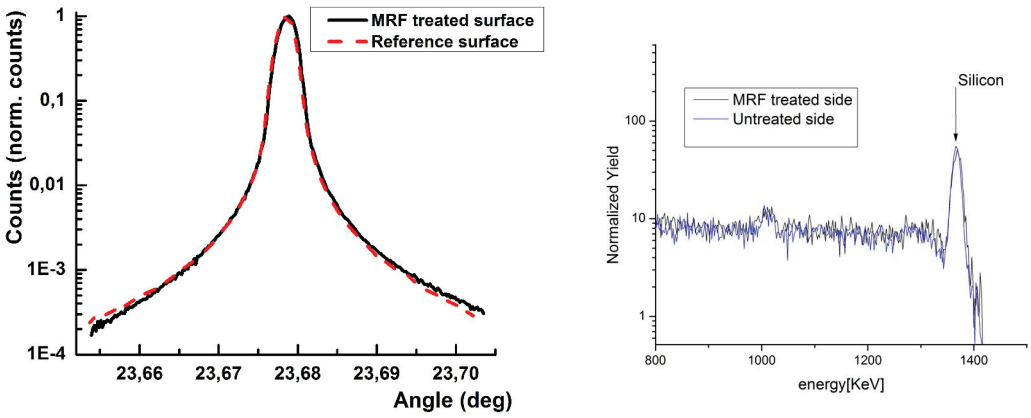

(a) (b)

Figure 2.6: High resolution x-ray diffraction rocking curve (a) and Rutherford back scattering in channeling mode (RBS-c) respectively on a Silicon MRF treated surface and on a reference surface. Noticeable differences are not observed, thus MRF does not induce any lattice damage to silicon. Courtesy of D. De Salvador.

Miscut fine measurement with autocollimator To suppress the systematic error due to mechanical plays, the setup for the miscut measurement was improved by introducing a custom autocollimator. An autocollimator is an optical instrument that is used to measure small angles with very high sensitivity. As such, the autocollimator has a wide variety of applications including precision alignment, detection of angular movement, verification of angle standards, and angular monitoring over long periods. The autocollimator projects a beam of collimated light. An external reflector reflects all or part of the beam back into the instrument where the beam is focused and detected by a photodetector. The autocollimator measures the deviation between the emitted beam and the reflected beam. Because the autocollimator uses light to measure angles, it never comes into contact with the test surface. For the miscut measurement, a custom autocollimator was designed for working into the closed space of the diffractometer, together with physical supports and connections. Design and commissioning of the instrument was done by A. Mazzolari in collaboration with E. Bagli, who developed a dedicated software. For miscut measurement, crystal is mounted on XRD and oriented to excite Bragg deflection (Fig. 2.8.a). Crystal is then rotated of 180° around the y-axis. Bragg deflection is lost due both to miscut and rotational stage mechanical plays. Mechanical plays are then compensated by means of the autocollimator (Fig. 2.8.b). After that, from this position Bragg deflection is found again, and the miscut with its sign can be determined (Fig. 2.8.c).

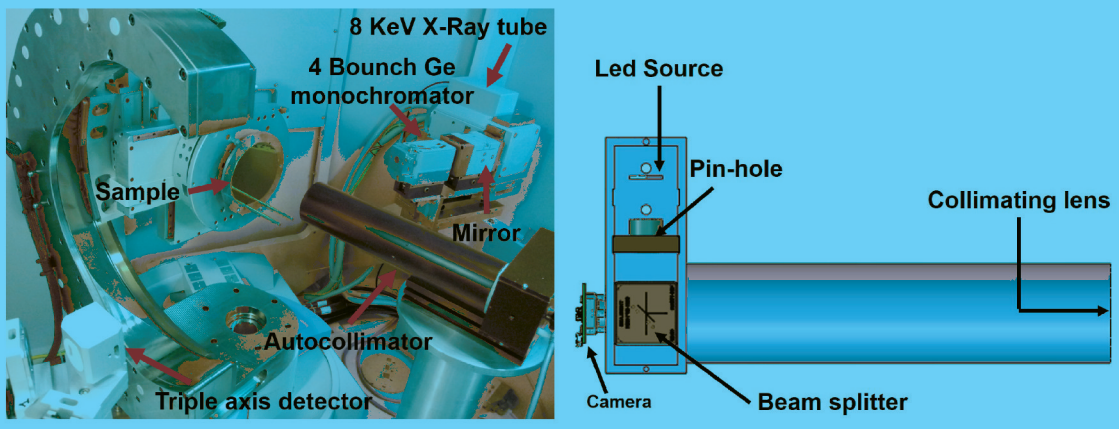

(a) (b)

Figure 2.7: Setup for miscut measurement with high resolution X-rays diffractometer and custom autocollimator (a), and design of the autocollimator developed by INFN Ferrara in collaboration with Panalytical (b, courtesy of A. Mazzolari).

Miscut reduction and polishing Once precisely measured the miscut, it is possible to schedule a further MRF step for reducing miscut while preserving the flatness of the surface. For instance, one of the pre-selected wafer presented a miscut equal to (73 ± 2) μrad befor treatment, and then presented a miscut of just (5 ± 2) μrad after it. This result is of fundamental importance, since it made possible the production of strip-like bent silicon crystals which perfectrly fulfils the requirements for the collimation in the LHC.

2.1.2 Anisotropic shaping

With the aim to realize strip crystals without inducing any lattice damage during their fabrication, a fabrication technique based on silicon anistrotropic etching was developed at SSL few years ago [65] and is still used now. This mode allows to engrave a silicon crystal and, differently from the isotropic etching allows to realize complex structures in silicon, among them also multi-strip crystals, which will be described later. In contrast to previously used isotropic etchings [64], there is class of chemical reactions based on alkaline solutions whose erosion rate depends on the crystalline orientation. In particular, (110) planes show the highest etch rate, (111) planes are the most resistant and (100) are in between. Anisotropic etching is a widely employed technique in modern micro-machining of silicon [77]. Thus, with proper choice of the components of the solution, anisotropic erosion would results in a high-precision cut of a crystal (see Fig. 2.10). A widely used silicon anisotropic etchant is Potassium Hydroxide (KOH). With the identification of H_2O

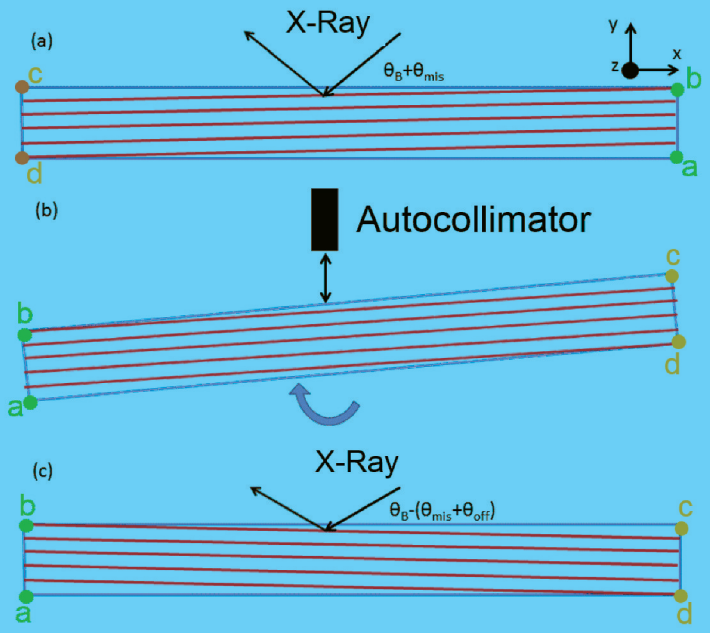

Figure 2.8: Method for miscut characterization with high resolution X-rays diffractometer and autocollimator. Mounted crystal is oriented to excite Bragg deflection (a). Crystal rotated of 180° around the y-axis. Bragg deflection is lost due both to miscut and rotational stage mechanical plays. Mechanical plays are compensated by means of the autocollimator (b). Bragg deflection is found again and miscut is determined (c).

and OH^- as reactant, the overall reaction is given by Eq. 2.1.

$$Si + 2H_2O + 2OH^- \rightarrow 2H_2 + SiO_2(OH)_2^{2-} \tag{2.1}$$

Empirically [78] it have been found that for KOH solutions with concentrations in the range 10-60%, the silicon etch rate R is given by Eq. 2.2.

$$R = k_0[H_2O]^4[KOH]^{1/4}e^{-E_a/kT} \tag{2.2}$$

where $k_0 = 4500\mu$m/h*(mol/L)$^{-4.25}$ and $E_a = 0.60$ eV for (110) planes, while $k_0 = 2480$ μm/h*(mol/L)$^{-4.25}$ and $E_a = 0.595$ eV for (100) planes. Table 2.1 summarizes etch rate for different planes of Silicon.

Silicon strip crystals were obtained by exploiting the strong anisotropy of silicon etch rate in KOH solutions. As shown in Fig. 2.9, a 100 nm layer of amorphous silicon nitride (Si_3N_4) was deposited onto all the faces of the wafer through Low-Pressure Chemical Vapor Deposition (LPCVD). A pattern representing the shape of the final crystals was carved into the silicon nitride layer by means of a standard photolithographic technique [77]. In more details, a Microposit S-1813

Crystallographic orientation	Etch rate (μm/min)
(100)	0.797
(110)	1.455
(211)	1.319
(221)	0.714
(311)	1.436
(331)	1.160
(111)	0.005

Table 2.1: Etch rate for different silicon planes in 30% KOH at 70°C [78]. Anisotropic etching in KOH is possible since (110) planes are etching much faster than (111) planes.

positive-photoresist layer was spun onto the top surface of the wafer. The masking pattern containing the shape of the strips was aligned with the wafer's flat. By exposing the masked photoresist to UV-light and then treating it with a developer solution, the photoresist was selectively removed. The uncovered silicon nitride areas were then removed with a 7:1 NH_4F-HF mixture [79], leaving uncovered silicon areas. The remaining photoresist was then completely removed. The wafer was immersed in KOH solution (40% weight concentration) with the Si_3N_4 pattern as a masking layer and kept at 70°C until the holes in the uncovered regions on the wafer were completed. For the experimental parameters of the solution we chose, the etch rate of (111) planes is negligible with respect to the (110) planes so that chemical erosion proceeds as depicted in Fig. 2.10. The protecting layer of Si_3N_4 is finally removed from lateral surfaces using HF 49%, leaving a wafer with regularly equi-shaped rectangular slots. Then, the wafer can be cut in such a way to achieve either a batch of independent strips (Fig.2.11c) or a rigid frame interconnecting a series of regularly positioned strips (Fig. 2.11b). First strips produced with this method were sized as (0.5-2) mm in the beam direction, (0.3-0.5) mm in the horizontal transverse direction (corresponding to the thickness of the starting wafer) and 70 mm in the vertical transverse direction (i.e. the direction of the principal bending). Strip dimension were tuned to match the requirements for application in the CERN SPS external lines, respectively H8, which operates with 400 GeV protons [80], and H4, which operates with 120-150 GeV negative particles [40]. The other geometry was studied to excite multiple volume reflection as a result of deflection of the particles with each strip [54]. More recently, thanks to newly-designed holders, the longest dimension of strips was reduced from 70 mm to 55 mm, thus allowing the usage of 4 inches starting wafers, which can be machined more easily with respect to 6 inches wafers. The length of the strip along the beam was sized also to other different length, for instance 4 mm for the LHC. Similarly, spacing and thickness of multi-strip crystals varies in the range 0.5 to 2 mm. More

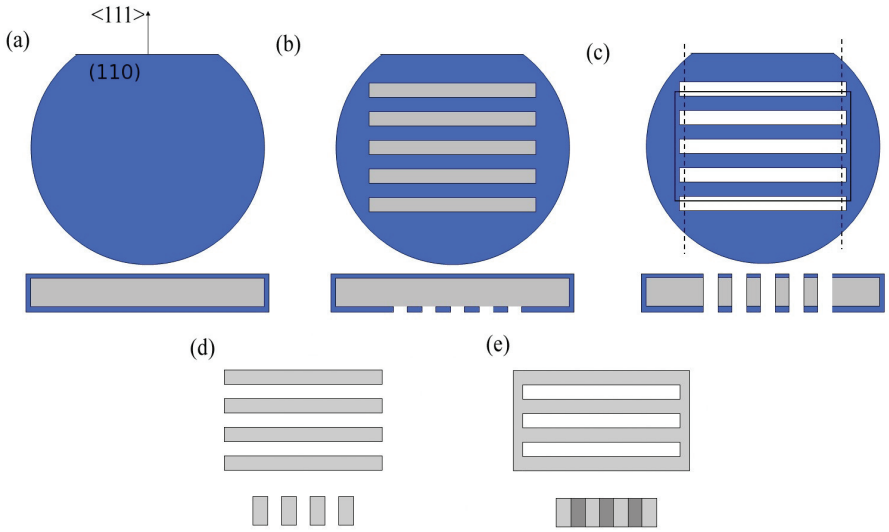

Figure 2.9: Fabrication of crystals for channeling (not to a scale) [65]: (a) deposition of a uniform 100-nm thick Si_3N_4 layer, (b) pattering of Si_3N_4, (c) anisotropic KOH etching and mechanical dicing along either the dashed line to release a series of independent strip-like crystals or the solid line to manufacture a multi-strip crystal with a frame, (d, e) final removal of the Si_3N_4 film. Masking by KOH resistant Si_3N_4 thin film patterned onto the surfaces of the Si crystal allows fabrication of rather complex geometries.

generally, the pattern of the photolithographic mask enables the achievement of a strip with any size of more complex structures that can be achieved by dicing the wafer parallel or perpendicularly to the lattice directions.

2.2 Strip-like crystals bending

Elastic strips or tapes (wires) are commonly used in industrial applications. When such strips are bent, the longitudinal strains, which are purposely induced, are accompanied by lateral strains in the width direction of the strip. As a result, the strip takes the shape of a saddle, i.e., it bends to a surface in which the two principal curvatures are opposite in sign. This effect is referred to as anticlastic deformation (AD). For an amorphous material, if the longitudinal radius of curvature, i.e. the primary radius of curvature, R into which the strip is being bent, is large, the cross section is found to deform to an arc of a circle with secondary radius $R_A = R/v$, where v is Poisson's ratio [81]. Thus, although the extent of AD is not large, it may cause practical difficulties. As an example, the edges of the magnetic tapes used in computer applications are found to wear because of it. Similar difficulties are encountered in the bending of the long metallic plates used

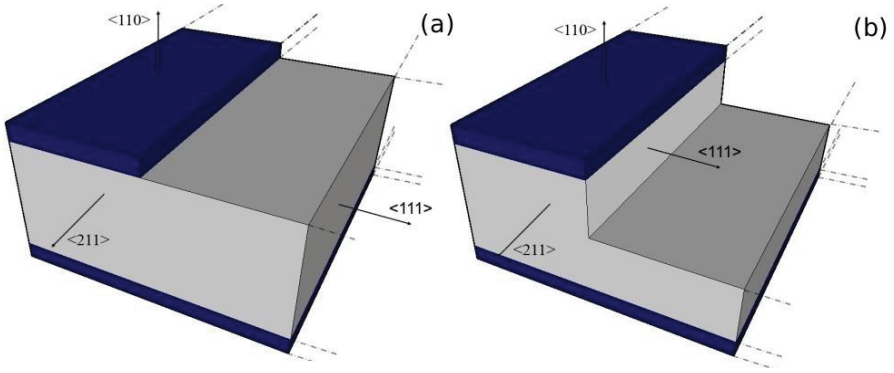

Figure 2.10: Schematic view of fabrication of a silicon crystal via anisotropic etching: (a) sample after patterning with Si_3N_4 (dark regions) and prior to chemical attack; (b) the unmasked areas undergo etching along the <110> direction while negligible erosion occurs along the <111> direction. Proper timing allows one to make controlled indentations or complete cut of the sample. Adapted from Ref. [65].

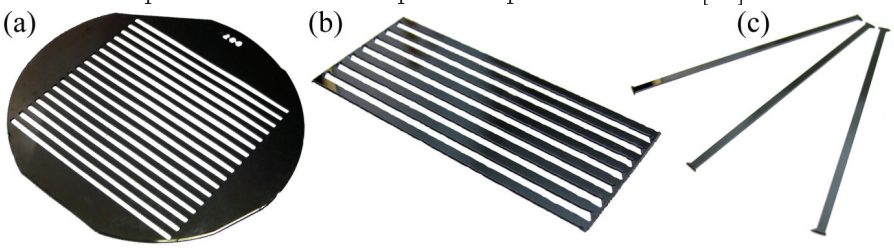

Figure 2.11: From left to right: a 4" silicon wafer with full passing holes realized by anisotropic etching (a). A silicon multistrip (b) and silicon strips (c) obtained by mechanical dicing of the wafer. Adapted from Ref. [65].

to form the adjustable working sections of wind tunnels. The consequent AD of the plates is found to interfere with the air flow. Although possible remedies to counteract anticlastic deformation do exist, e.g. by proper tapering of the edges on the concave sides of the tapes or plates, there are applications in which AD is desirable. A significant example is particle-beam steering through channeling in a crystal. As one might expect, AD of an anisotropic material, as needed for channeling experiments, would lead to significant dependence of the curvature ratio R/R_A on the chosen crystallographic direction.

2.2.1 Anticlastic deformation in an anisotropic material

I here report some concepts of anticlastic deformation in a isotropic material that are necessary for understanding further modelling. A typical strip crystals is $70\times2\times0.5$ mm^3 wide (see Fig. 2.12). Thereby, the shape of the crystal is such

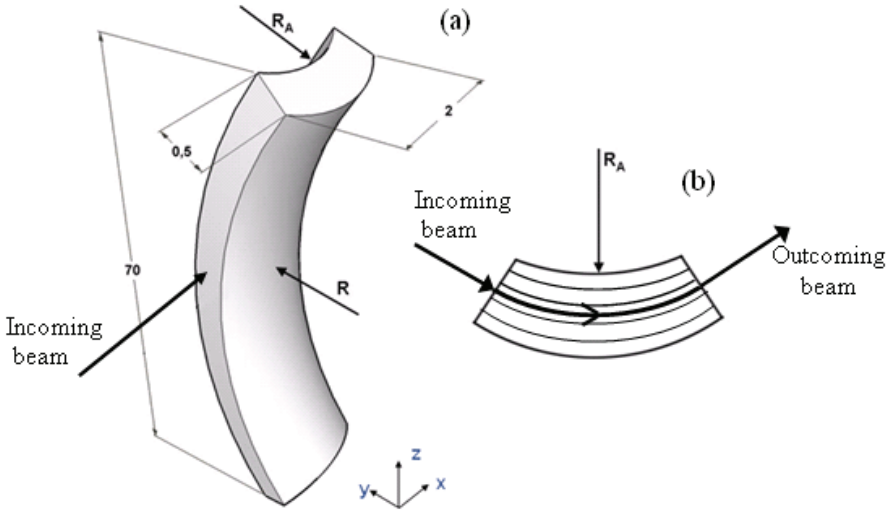

Figure 2.12: Sketch of a bent silicon strip for channeling experiments [82]. Anticlastic deformation with radius R_A arises as a result of primary bending with radius R. Quotes are expressed in mm and represent typical values for high-energy experiments. (b) Cross-section of the crystal; the incoming particles are captured by the potential of atomic planes and the beam is being deflected.

that the theory of a mechanical beam can be worked out extensively.

Crystalline silicon exhibits Face-Centered Cubic (FCC) symmetry and diamond lattice with each atom on the centre of a tetrahedron with four nearest-neighbour atoms at the four vertexes. Thereby, Young's modulus and Poisson's ratio are direction dependent [83]. As for any FCC symmetry, the elastic properties are completely characterized by only 3 independent constants. For Si, the compliance matrix, $\mathbf{S}$, referred to the canonical base $<\mathbf{e}> = \{ <100>, <010>, <001>\}$, where $<100>$, $<010>$, $<001>$ are main crystalline axes of the cubic cell, takes the form of Eq. 2.3.

$$\mathbf{S}^{<e>} = \begin{bmatrix} 7.678 & -2.144 & -2.144 & 0 & 0 & 0 \\ & 7.678 & -2.144 & 0 & 0 & 0 \\ & & 7.678 & 0 & 0 & 0 \\ & & & 12.531 & 0 & 0 \\ & Sym & & & 12.531 & 0 \\ & & & & & 12.531 \end{bmatrix} \times 10^{-3} MPa \quad (2.3)$$

In channelling experiments, the crystal is bent to a relatively modest curvature. The primary deformation is imparted at the edges of the strip through a mechanical couple of moment M by clamping onto a rigid holder which will be described later. Such a system can be modelled as a homogeneous and anisotropic

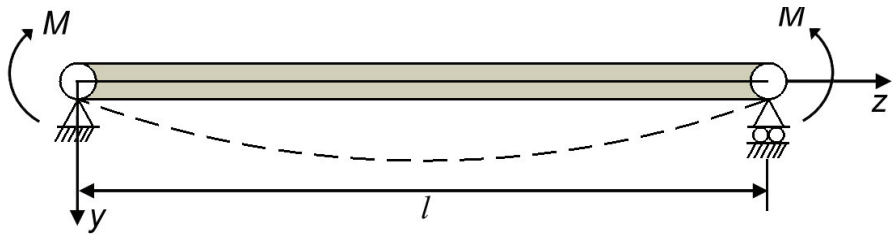

Figure 2.13: Schematic representation of bending of a beam of length l under the action of a couple of moments applied at its ends [82].

bar under infinitesimal deformations and small displacement. The strip is supported at its ends by kinematics and concentrated guides, and bent by a point-like couple of forces at its edges, as shown in Fig. 2.13. The displacement of the strip along y direction $v(x, y, z)$ is given by equation 2.4, from Ref. [84]:

$$v(x, y, z) = \frac{1}{2a_{13}R}[-a_{13}x^2 + a_{23}y^2 + a_{33}(lz - z^2) - a_{35}xz] \tag{2.4}$$

where a_{ij} are the 6×6 coefficients of $\mathbf{S}^{<e>}$. Presence of the z^2 term is related to the imposed principal bending while the x^2 term shows that $x - y$ cross section is deformed as a parabola, giving rise to anticlastic bending, whose magnitude is linearly proportional to the imposed bending. The most directly observable physical quantity is the principal curvature while anticlastic deformation is quantified by the secondary curvature. Thus, the ratio R_A/R determines the extent of anticlastic deformation in dimensionless units. Differently from the case of an isotropic material, the ratio between anticlastic and principal bendings is determined by the two components of the elastic compliance tensor. For our applications, the region of interest is the central part of the crystal so that R_A/R is calculated at x=0, y=0, z=l/2, thus being expressed by Eq. 2.5:

$$\frac{R_A}{R} = -\frac{a_{33}}{a_{13}} \tag{2.5}$$

It should be remarked that a_{33} cannot vanish; thereby it is impossible to find a bent silicon crystal without anticlastic deformation. Moreover, R and R_A have opposite signs, i.e., the crystal takes the shape of a saddle. It should be remarked that Eq. 2.4 holds for crystals narrow enough in the width direction such to develop a plain stress regime. In fact, by increasing the crystal width b, the system tends to behave like a plate under plain strain condition, thus preventing anticlastic deformation [85]. As reported in [85–87], an estimator of this behaviour is the "Searle parameter" defined by Eq. 2.6:

$$\beta = \frac{b^2}{Rt} \tag{2.6}$$

where t is crystal thickness. If $\beta < 1$, anticlastic bending arises on the whole crystal width (beam-like behaviour). Conversely, if $\beta \gg 1$, anticlastic bending results to be confined only in the external regions of the crystal (plate like behaviour). As will be demonstrated in the following, we will deal with the case $\beta \ll 1$ for strips. The ratio in Eq. 2.6 is orientation dependent so that designing a bent crystal for channeling and volume reflection experiments demands its knowledge for any orientation of the strip. For planar channeling and volume reflection, the (110) planes were found to be best efficient, namely the crystal is to be oriented with such axis along y axis in Fig. 2.13. The remaining two directions are to be chosen and R/R_A should be studied as a function of the base,$<\mathbf{m}>$, with the vectors parallel to the sides of the crystal. Thereby, the compliance tensor in the base $<\mathbf{m}>$ is linked to $\mathbf{S}^{<\mathbf{e}>}$ through the similarity transformation expressed by Eq. 2.7:

$$\mathbf{S}^{<\mathbf{e}>} = \mathbf{K}\mathbf{S}^{<\mathbf{e}>}\mathbf{K}^T \tag{2.7}$$

being $\mathbf{K}$ the rotation matrix connecting the $<\mathbf{e}>$ base to the $<\mathbf{m}>$ base.

The orientational dependence of strained silicon strips have been deeply investigated, and the results were published in Ref. [82]. To do that, several crystals of size $2{\times}0.5{\times}70$ mm^3 were diced from a 0.5 mm thick (110) silicon wafer, and the induced lattice damage was removed by isotropic etching decribed in Ref. [64]. The wafer's "flat", i.e., the cut done by the manufacturer for better usage of the wafer was parallel to the $(1\bar{1}0)$ plane. The crystals were cut at some inclination, θ, with respect to the flat (see Fig. 2.14 and Tab. 2.2) and all of them were oriented with the $<110>$ direction along y axis. The ratio R_A/R was studied by bending the crystal through the holder typically used in channeling experiments and which will be described later.

The principal and anticlastic radii were measured by means of a white-light profilometer (Veeco NT1100) capable of recording the profiles of the bent crystal with height resolution of 3 nm. In order to make the surface orientation independent from the alignment with respect to the profilometer objective, tilt and piston terms were removed via software. Figure. 2.15 shows a typical profile of the strip taken in a central region 2×2 mm^2 wide, which exhibits a saddle-like surface as predicted by elasticity theory. Figure. 2.17 illustrates the experimentally recorded levels of R_A/R for the values of θ in Tab. 2.2. Clear signature of orientation dependence is observed with the ratio R_A/R attaining its maximum for the direction $<1/\sqrt{2}\ \ 1/\sqrt{2}\ \ 1>$ and its minimum for the direction $<100>$. Such trend reflects the behaviour of Poisson coefficient for a (110) plane [83]. Moreover, it should be

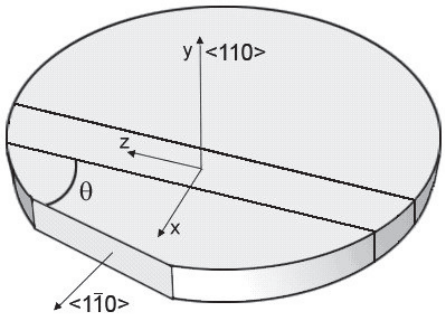

Figure 2.14: Silicon crystals are diced from a (110) wafer with the longest dimension of 70 mm at several angles θ with respect to the wafer's flat. The Y axis is always the <110> direction, while x and z vary as function of θ [82].

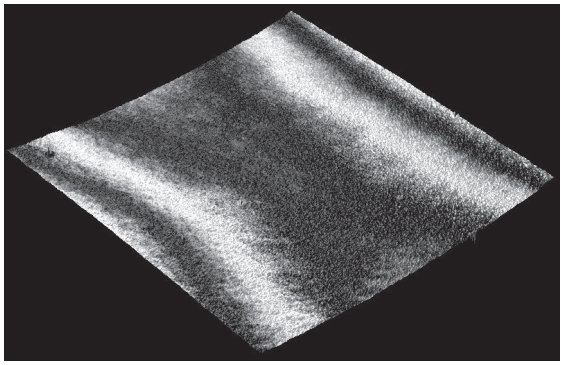

Figure 2.15: Deformation of the crystal surface when bent by the holder. The crystal is diced at $\theta = 35.26°$. A saddle deformation is visible thanks to interference fringes [82].

noticed that the crystalline orientation $\theta = 35.26°$ corresponds to a crystal with the <111> axis along the beam direction, i.e., the most favourable condition to study axial channeling. The expected ratio of $|R_A/R|$ versus the angle θ, reported in Fig. 2.17, has been obtained analytically by calculating the ratio $|a_{33}/a_{13}|$, which is the Poisson ratio for the corresponding crystalline direction, according to classical mechanical beam theory. Figure 2.17 also includes experimental results for the ratio $|R_A/R|$, which are in good agreement to theoretical values for each crystalline direction.

It should be remarked that Eq. 2.5 holds true for the ideal case of concentrated supports at the edges of the strip but, in practice, clamping of the crystal mounted on the holder occurs over a finite region. Thereby, distortion of the shape of the bent crystal from a saddle is expected, particularly in proximity of the holder jaws. With the purpose of taking into account information about the portion of crystal not influenced by the presence of holder jaws, Finite Element Method (FEM) simulations based on STRAUS7 software (release 2.3.3) were worked out

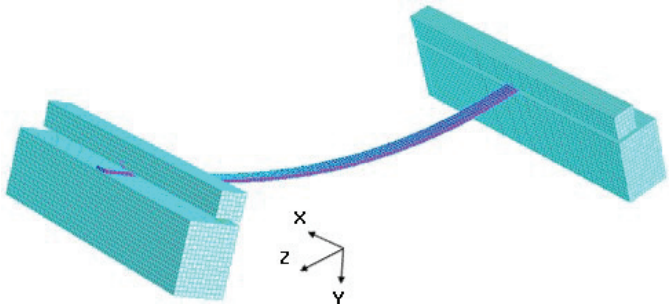

Figure 2.16: Mesh of a Si strip mounted on the holder jaws for Finite Element Mode simulations (b). The strip ($2 \times 0.5 \times 70mm^3$) was simulated by 528-brick elements, whereas 36496 bricks elements model the holder supports [82].

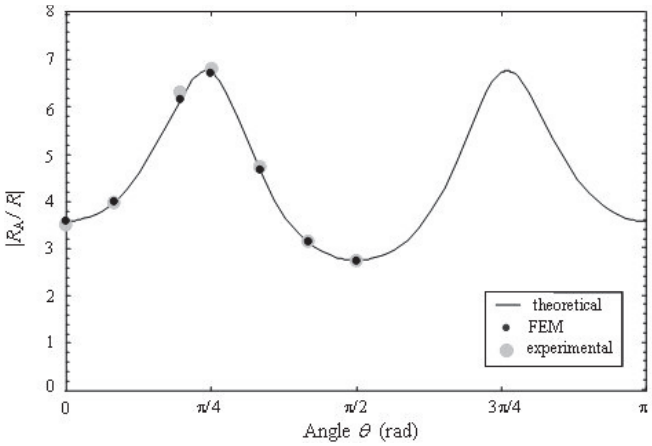

Figure 2.17: Ratio $|R_A/R|$ as function of θ (for its definition see Fig. 2.14). Experimental data are compared with FEM simulation and with the model. The figure shows that the ratio $|R_A/R|$ is direction dependent as expected from a crystal [82].

considering the geometry of the holder (see Fig. 2.16), which is routinely used in channeling experiment.

2.2.2 Holders for strips and multistrips

In order to impart to the crystal the desired bending and to keep it in position with respect to the beam, special holders have been designed. Two different kind of holders were realized to bend single strip crystals or multi-strip crystals.

Holder for strip crystals The holders to bend single strip crystals were initially designed in collaboration with the Russian Institute for High Energy Physics IHEP, and are based on deformation control technology. Since 2007 holders for strips

θ (deg)	R_A/R (measured)	R_A/R (theoretical)	R_A/R (FEM)
0	-3.52	-3.59	-3.58
15	-3.98	-4.00	-4.00
35.26	-6.31	-6.20	-6.15
45	-6.82	-6.80	-6.73
60	-4.72	-4.70	-4.67
75	-3.16	-3.15	-3.14
90	-2.75	-2.76	-2.75

Table 2.2: Ratio between anticlastic and principal bending radii as a function of θ: comparison between theoretical model, measurements and FEM simulations [82].

and multi-strip crystals have been designed in mechanical workshop of physics department and INFN of Ferrara University. Acting on the bolts highlighted in red in Fig 2.18 the holder is mechanically deformed allowing adjustment of the relative distance of the surfaces over which crystal lean on. Adjusting the distance between such surfaces it is possible to adjust the main crystal bending radius, and keeping in mind the expected ratio between anticlastic and main bending radius it is possible to obtain the wanted deflection angle. Such scheme provides flexibility for bending though, on the other hand, mechanical strain due to holder deformation propagates through the holder and alters planarity and parallelism of surfaces where crystal lean on inducing torsion on the crystal. In order to correct for torsional effects a screw (highlighted in green) is used. Such screw-based torsion compensation system demonstrated to be very effective, allowing to obtain torsions of less than 1μrad/mm.

State-of-the art technology is represented by the holders used to bend a 4 mm strip for LHC collimation. The holder used to bend the crystal shown in Fig. 2.19 is composed of a total of 14 parts, i.e.:

- 1 "main component", made of Titanium grade V manufactured by "Cinel - Instruments for Research and Industry" in May 2015 by means of milling and and electro-discharge machining operations. Between milling and electro-discharge machining the part was subject to a thermal annealing in order to release the mechanical stress generated in the first operation (see table 2.20 for more details). Thermal annealing was conducted on May 4th 2015, while electro-discharge machining was conducted on May 6th 2015. Titanium grade V was supplied by "Stupino Titanium Company";
- 6 dowel pins, diameter 2-H7 mm, made of Titanium grade V, provided by "Cinel - Instruments for Research and Industry" on May 2015. Those parts were manufactured by mans of turning operations. Titanium grade V was supplied by "Stupino Titanium Company";

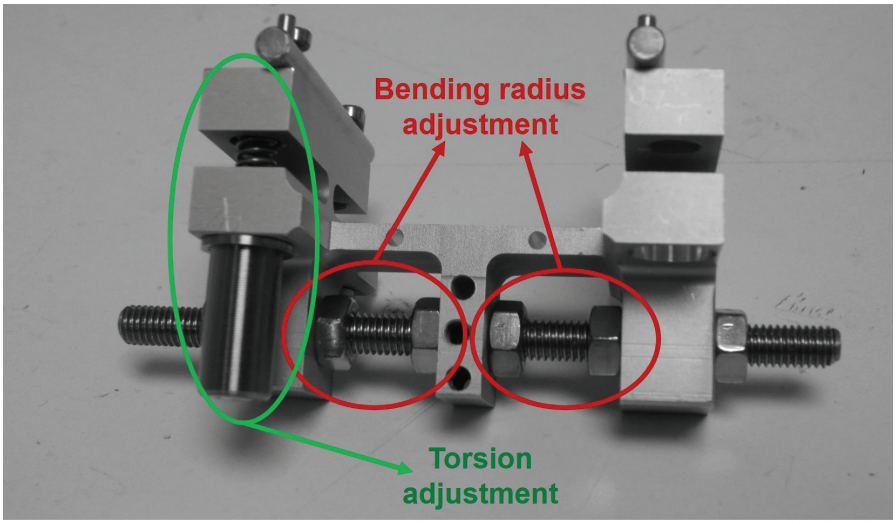

Figure 2.18: Bending holder for strip crystals. Mechanisms for bending and torsion adjustment are highlighted in the figure and explained in the text.

- 1 threaded bar M5x0.25, made of Titanium grade V and manufactured by the company the "Biomeccanica Srl" in April 2015 by means of turning operations. Prime Titanim grade V was supplied by "Tifast SRL";
- 6 nuts M5x0.25, made of Titanium grade V and manufactured by the company the "Biomeccanica Srl" in April 2015 by means of turning operations. Prime Titanim grade V was supplied by "Tifast SRL";
- 4 screws M2, made of stainless steel 316 LN, provided by "Bulloneria Morelli Di R. Morelli & C. Sas" on May 2015.

The total weight of holder assembly results to be 93.0±0.1 g. On May 2015 all the titanium parts were subject to thermal annealing in order to relieve stresses generated during their machining. See Table 2.20 for details on the thermal annealing procedure.

Holder for multistrip crystals Non flatness of surfaces where the crystal lean on is not important for the single-strip crystal, but is crucial for a good reciprocal alignment of the strips in a multi-crystal. In order to minimize the deformations induced on such surfaces by the mechanical deformations imparted to the holder, a new bendng device was designed. I here adapt the description of holders for multistrips given in Ref. [88]. Figure 2.21a is a schematic of the holder realized for multi-crystals, whose details can be appreciated in the exploded view of Fig. 2.21b. A rigid frame of two unparallel cavities serves to host the edges of the multi-crystal with the components to fasten it to the holder itself. The cavities are reciprocally inclined in order to impart to the crystal the wanted curvature.

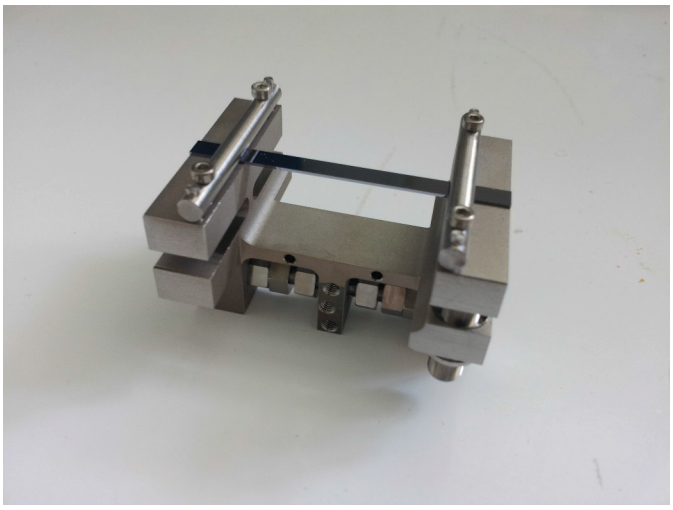

Figure 2.19: One of the latest silicon bent strips. Crystal parameters and holder materials are optimized for the collimation of the 7 TeV proton beam circulating into LHC.

Time (min)	Temperature	Pressure (mbar)
0	Room temperature	$1.26\text{x}10^{-6}$
30	350 °C	$3.24\text{x}10^{-6}$
40	350 °C	$3.24\text{x}10^{-6}$
70	700 °C	$3\text{x}10^{-5}$
250	700 °C	$3\text{x}10^{-5}$
1080	Room temperature (radiative cooling)	$1.23\text{x}10^{-6}$

Figure 2.20: Thermal annealing steps performed on titanium components composing the holder assembly bending the crystals STF105 and STF106, which were realized for working in the collimation of the LHC proton beam. Courtesy of A. Mazzolari.

The holder was electro-eroded from a mono-block of ergal which was selected because of its good elastic properties and the possibility to be used under vacuum environment. Electro-erosion guaranteed very precise sizing, low roughness and high planarity of the surfaces. Two stainless $9\times9\times30$ mm^3 parallelepiped at each of the crystal edges were used to clamp the crystal. Steel was used because it can be worked mechanically with high accuracy and importantly it offers a relatively high Young modulus. Glass might be an alternative material that can be finished with superior planarity though its lower Young modulus caused it to deform under the action of the screws. The surfaces in contact to the crystal (9×30 mm^2) were manufactured with very high planarity over the whole surface (measured to be $\sim$ 150 nm excluding the 1 mm edge of the block). Final clamping was achieved

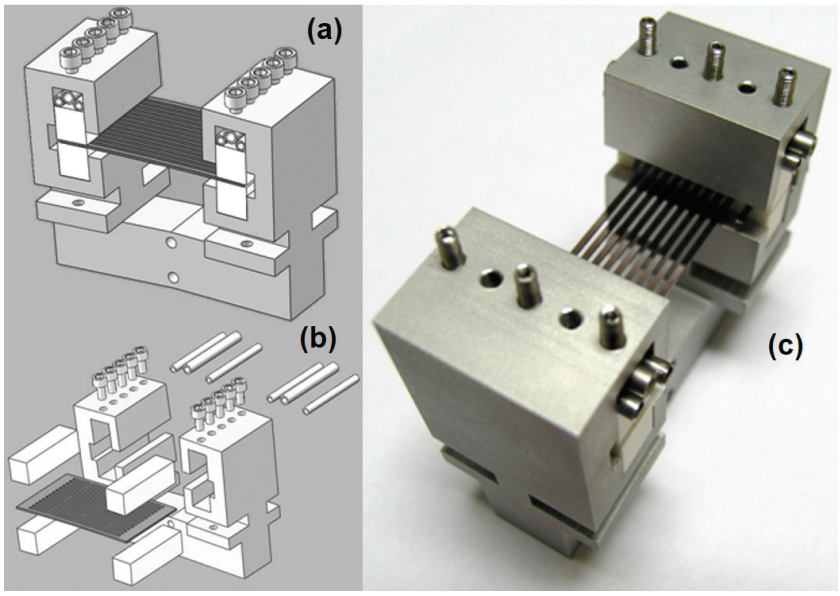

Figure 2.21: Schematic view of a multi-strip crystal assembled on its holder(a), exploded view of the holder and crystal assembly (b), and photo of multi-strip mounted in the holder (c). Adapted from Ref. [88].

thanks to an array of five low-thread screws at each of the crystal edges. The localized deformation field induced by the screws as applied directly onto the parallelepipeds was found to alter the parallelism of the strips, thereby a damping system of three pipes at each side softened the deformation. The pipes were made of harmonic steel. Another critical point was the thickness of the parallelepipeds in the direction perpendicular to the crystal. In fact, such dimension was empirically chosen to be sufficiently thick as to make the total misalignment of the strip to be sufficiently mild. Finally, the wafer from which the crystal was fabricated should exhibit a planarity comparable to that of the parallelepiped onto which the crystal is laid. For the prototype described in Ref. [88], a 1.5 μm planarity 4" silicon wafer was used as a starting material, and were then was brought to 300 nm planarity over areas of $9\times27\text{mm}^2$ by means of polishing operations. The multi-crystal was inserted and fastened into the holder for bending (See Fig. 2.21c).

2.2.3 Characterization methods

In order to manufacture and bend a crystal with the desired parameters (bending radius, torsion, ecc), a crucial importance is given by characterization methods, which were performed with instruments available at SSL Ferrara.

The newest measurement instrument is the FOGALE T-MAP IR shown in

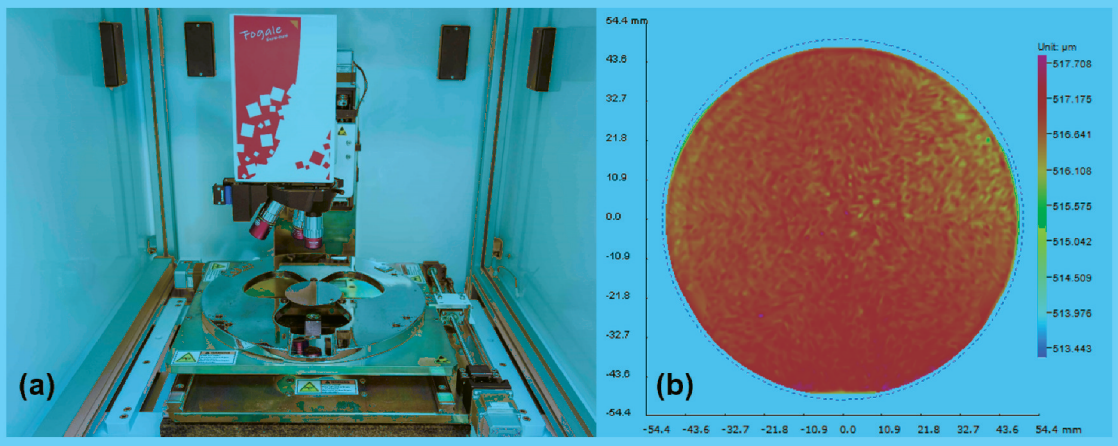

Figure 2.22: Photo of the Fogale T-Map IR interferometer (a) during a thickness measurement (b) of a silicon wafer.

Fig. 2.22a, which is an Infra-Red (IR) interferometer designed for the semiconductor applications. The T-MAP IR relies on the measurement principle of low coherence interferometry, in particular the optical probe directs a 1310 nm IR light through the substrate material and send back the light reflected by each layer interface (including the air-substrate interface) to the control module. With this instrument several characteristics of the substrate such as thickness, bow, warp and individual thickness of stacked layers, for all kind of substrate without metal coating can be measured. Wafers with a size from 2" to 300 mm and a totat thickness ranging from 5 μm to 5 mm can be placed onto specific sample holders. The minimum thickness of the individual layer of the stack is 3 μm, and thickness can be measured with 0.1 μm resolution and 0.1 μm accuracy in a spot sized down to 5 μm.

As shown in Fig. 2.22b, a fine map of the thickness (0.1 $\times$ 0.1 mm) of starting wafers was done. This is important in order to eventually reject starting wafers with a bad thickness uniformity, and to more precisely estimate the thickness of the wafer, which will correspond to the transverse thickness of final silicon strips. After strip shaping, strip dimension along the beam can be measured with the same procedure. The uncertainty of thickness determination, considering thickness variations and systematic errors, is estimated to be around 20 μm.

A bending moment applied to a crystal causes the deformation of the surface, as well as for the inner crystallographic planes. Therefore, by analyzing the crystal surface, we can determine the deformation of the crystalline planes. Crystal surface can be characterized with a WYKO NT1100 white light interferometer. In more details, the NT1100 utilizes white light interferometry for non-contact high resolution 3D surface measurements, from sub-nanometer roughness to millimeter-high

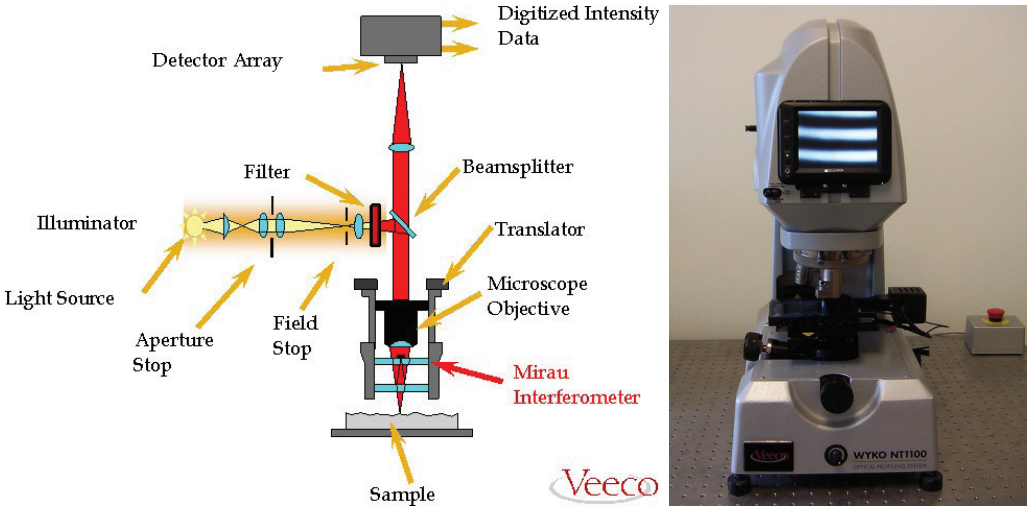

Figure 2.23: Working scheme (a) and photo of the white light interferometer WYKO NT1100 available at SSL.

steps. Two different techniques, respectively named optical phase-shifting (referred as PSI mode) and white light vertical scanning interferometry (VSI mode) allows a wide range of morphological measurements, from sub-nanometer roughness to millimeter-high steps. The PSI mode uses red light, has 1 μm of horizontal- and 1 nm of vertical- resolution and is capable of measuring a roughness up to 160 μm, while the VSI mode uses white light, has a vertical resolution of 1 μm and can be used to characterize surfaces with a roughness up to 2 mm. For strip crystals, the effective deformation imparted by the bending holder can be estimated with the procedure shown in Fig. 2.24. In more details, strip suface is measured before (Fig. 2.24(a)) and after (Fig. 2.24(b)) bending. The substraction gives a map of the effective deformation (see Fig. 2.24(c) and 2.24(d)), which can be used to estimate bent crystal geometrical parameters such as principal- and anticlastic-bending radius and torsion. Once done that, we can finely adjust principal bending and, in turn, anticlastic bending, as well as reducing unwanted torsion, and then measure again the deformation. These operations are repeated few times, until the desired deformation is obtained. The interferometric characterization gives a result with an uncertainty estimated to be around 5-10 % for typical principal bending radiuses, which are of the order of $1 \div 10$ m, and torsion with a precision below 10 μrad/mm.

After the surface analysis, bent crystals are characterized by means of a high-resolution X-rays diffractometer (Panalytical X'PERT^3 MRD (XL)). A 8 keV X-rays beam is delivered by a tube with Cu target through a Goebel mirror [89]

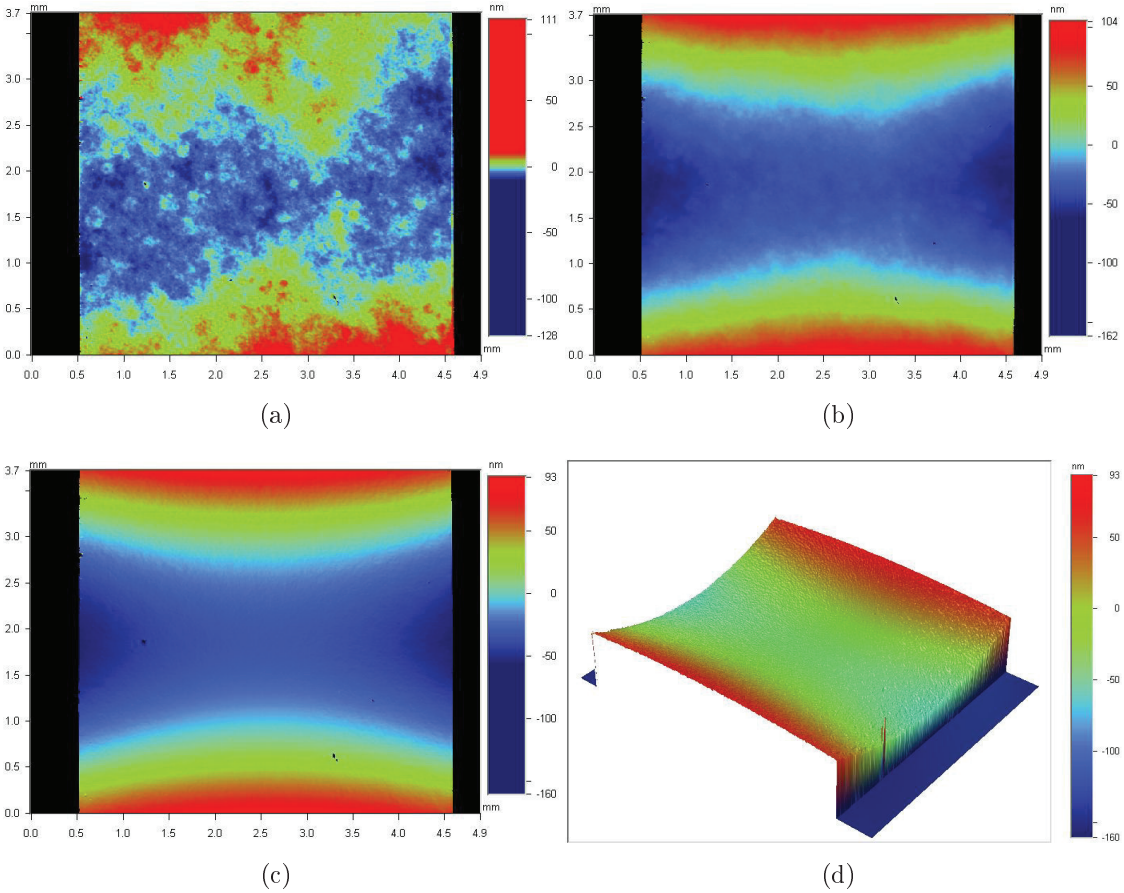

Figure 2.24: Determination of strip crystal deformation by means of interferometric characterization of crystal surface with WYKO NT1100 in PSI mode: surface of unbent strip (a), surface of bent strip (b), effective bending (c) obtained as difference between (b) and (a), and a 3D representation of effective bending (d).

followed by a four bounch Bartels germanium monochromator [90]. The sample is mounted onto a MRD cradle, which is moved by the high-resolution X'Pert PRO goniometer. This system combines all the functionality of an open Eulerian cradle with translations in x-, y- and z-directions. The motorization and precision of its five movements ensure sample positioning with 0.01 mm accuracy in x- and y-direction, 0.0001 mm in z direction, 0.0001° for rotation in the ω axis and 0.0001° in the χ axis.

As an example, I here describe the procedure of anticlastic deformation measurement procedure shown in Fig. 2.25. Bent strip is mounted onto the cradle with a purposely design support, aligned in vertical position and centered with respect to the beam in ordered to excite bragg reflection of the (110) planes. The inclina-

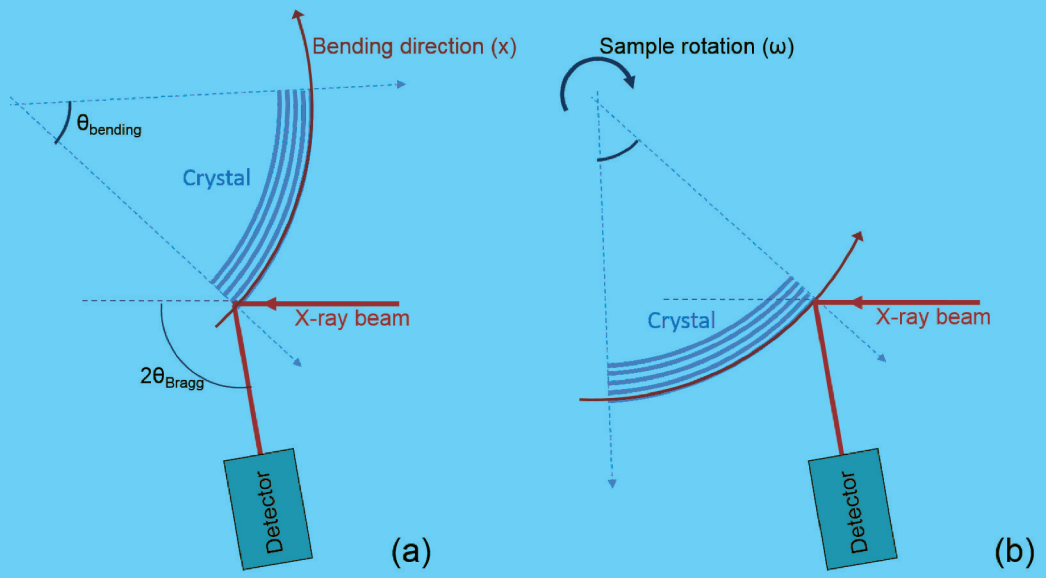

Figure 2.25: Procedure for bending determination with X-rays diffractometer. Rocking curve is measured for X-rays beam impinging on a side of the surface of the crystal (a) and then on the opposite side (b). Angular shift of the RC corresponds to the total bending angle.

tion of atomic planes in the horizontal direction slightly changes due to anticlastic deformation. By moving the crystal in the horizontal direction we can change the position of the crystal where the X-rays beam impinges, and observe a rocking curve shift, as highlighted in Fig. 2.26(b). The total shift along the horizontal direction corresponds to the effective bending angle for channeled particles, which can be measured with an uncertainty below 5%, and eventually down to 1-2 % by improving measurement setup with an autocollimator, as we did for the finest miscut determination described in Sec. 2.1.1. Moreover, by measuring the rocking curve peak position in various intermediate positions, we are capable of checking bending uniformity along the horizontal direction.

A RC shift may arise also when moving the crystal in the vertical direction. This effect is a consequence of crystal torsion. By measuring RC at various vertical positions of the crystal we can locally determine crystal torsion.

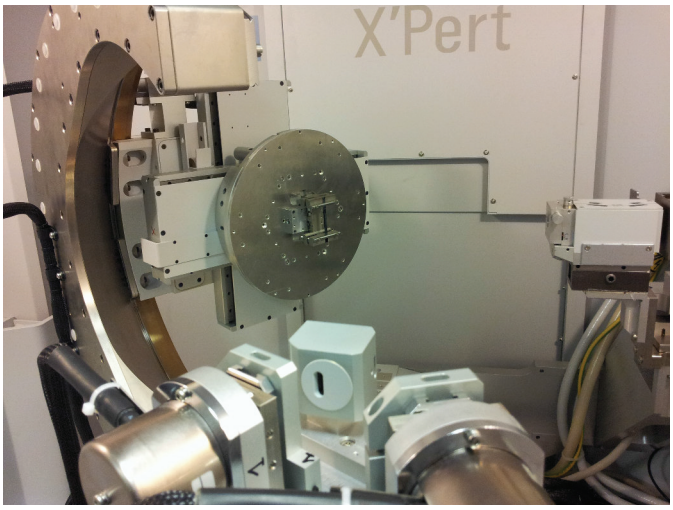

(a)

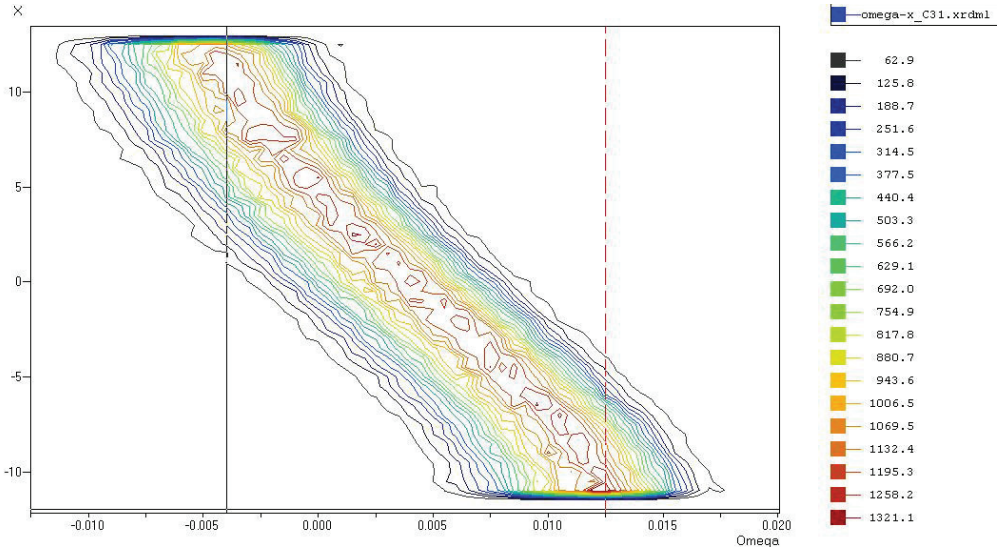

(b)

Figure 2.26: Anticlastic measurement with X-rays diffractometer. Photo of the setup (a) and series of Rocking Curve measurement as a function of the point of impinging of the X-rays beam along the anticlastic bending of the crystal (b).

2.3 Most significant strip crystals manufactured

Since the beginning of my phD, we fabricated and bent several silicon strips, with different characteristics, according to the specific requirements of each application. I here report a description of the most significant ones.

2.3.1 Strip crystals for the collimation in LHC

The leading edge of strip technology is represented by the prototypes realized for the collimation of the proton beam circulating in LHC, which is the aim of the UA9 experiment at CERN. Bending holder is made of titanium grade V, treated with dedicated thermal cycles to relax stress arising due to machining, as reported in Sec. 2.2.2. Starting wafers with (110)-oriented surface were treated with Magnetorheological finishing, before shaping strips with a thickness along the beam of 4 mm. After bending, torsion was adjusted with screws having an extremely low pitch (0.2 mm). Bending angle and torsion characterization were performed by means of white light interferometry and high-resolution X-rays diffractometer. One of them (STF75, see Fig. 2.27) has been installed in the LHC pipe in April 2014, then tested for LHC proton beam collimation in August- and November-2015. A spare crystal with the same characteristics (STF76) was also characterized at the extracted lines SPS-H8 at CERN in several test beams with various ion beams. In 2015 new strips (STF105 and STF106) were mounted onto new holders with optimized torsion and bending angle, despite strips were obtained from wafers which were not treated with MRF, thus resulting in a comparatively higher muscut. Geometrical parameters of the two strips are shown in Table 2.3.

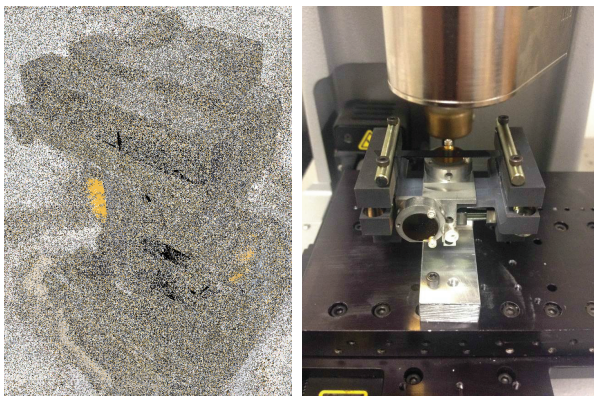

(a) (b)

Figure 2.27: Photo of strip crystal ST75 manufactured at SSL Ferrara and tested in LHC (a) and during interferometric characterization (b). Mirrors were installed for laser alignment.

Parameter	Expected	STF75	STF76	STF105	STF106
Thickness along the beam (mm)	∼4	4.10±0.02	4.10±0.02	4.07±0.02	4.08±0.02
Bending angle (interferometer, μrad)	∼50	52±2	52±2	51±5	46±5
Bending angle (X-rays, μrad)	∼50	51±1	53±1	49±3	41.5±1.5
Miscut (X-rays + autocollimator, μrad)	<10	6±1	6±1	40±4	40±4
Torsion (interferometer, μrad/mm)	<1	6±1	6±1	<2	<2
Torsion (X-rays, μrad/mm)	<1	6±1	6±1	<2	<2
Heating compatibility	Yes	Yes	Yes	Yes	Yes

Table 2.3: Parameters of the prototypes (ST75, ST76, STF105 and STF106) of strip crystals proposed for LHC installation.

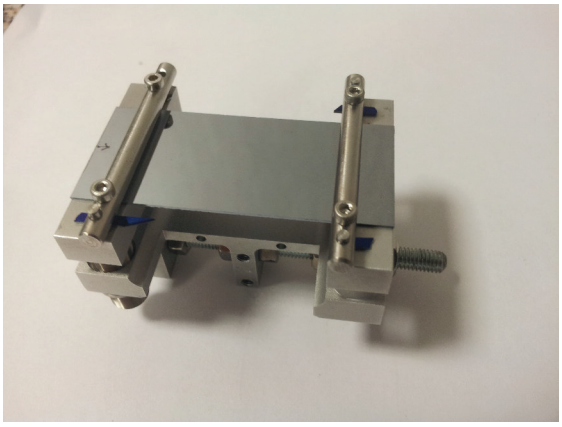

Figure 2.28: PL02 crystal mounted onto a mechanical bending holder.

Parameter	PL01	PL02	PL02B
Channeling plane	(110)	(110)	same of PL02
Channeling axis	<111>	<100>	"
Thickness along the beam (mm)	20.0±0.1	23.8±0.1	"
Transverse thickness (mm)	0.52±0.02	0.52±0.02	"
Height (mm)	55.0±0.1	55.0±0.1	"
Bending angle (interferometer, μrad)	240±40	270±50	2150±200
Torsion (interferometer, μrad/mm)	∼10	∼10	∼20

Table 2.4: Parameters of the first long crystal prototypes for the extraction.

2.3.2 Strip crystals for the extraction in LHC

For the CRYSBEAM project, which is devoted to the development of a new type of crystal-based particle beam extractor in accelerators, two prototypes (PL01 and PL02) of thin bent crystal capable of deflecting of ∼300 μrad within a long crystal (i.e. thickness along the beam >20mm) were produced, mounted onto a mechanical bending device, characterized at SSL and tested with a 400 GeV/c proton beam at the H8-SPS CERN beam line. After this, PL02 was recently modified in such a way to deflect ∼2 mrad and characterized again, thus being ready for testing with ultrarelativistic ions in the next future. The second version of the PL02 crystal is referred as "PL02B". The parameters of the CRYSBEAM crystals are reported in Table 2.4.

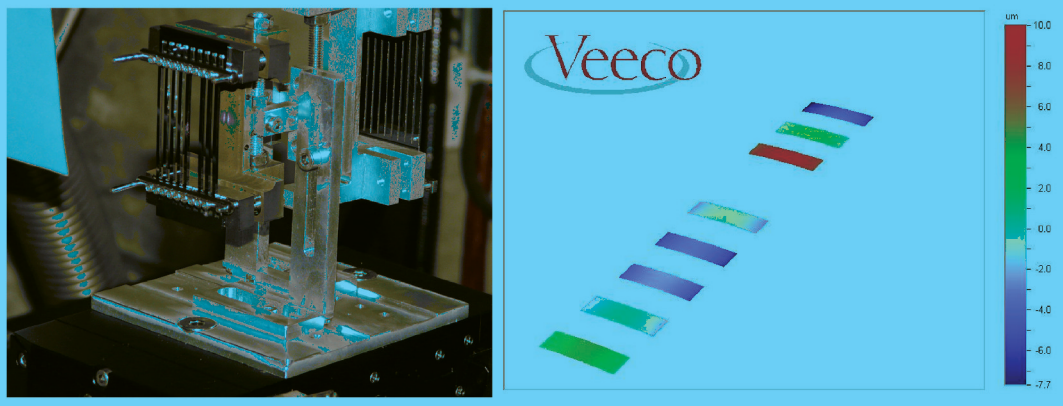

(a) (b)

Figure 2.29: Photo of the multistrip crystal MSTF13 manufactured at SSL Ferrara mounted for test at H8-SPS (a). Interferometric characterization of MSTF13 (b).

2.3.3 Multistrip crystal for collimation in SPS

In the framework of the UA9 experiment, multistrip crystals were proposed as an alternative scheme with respect to channeling for the crystal-assisted collimation of the Super Proton Synchrotron (SPS). In this case, deflection is provided by the multiple volume reflection effect described in Sec. 1.2.2. We realized a prototype in 2014 (MSTF13) which was characterized at the line external line H8 with pions of energy 180 GeV in December 2014 (see Fig. 2.29(a)), then installed in the SPS in January 2015 . Multistrip was realized with silicon prime material, and is composed of 8 aligned strips with a thickness along the beam of 1.28 mm for each strip. Strips were mechanically shaped in such a way to obtain (110) channeling planes, and the entry face with respect to the beam parallel to the (100) plane. This particular cristallographic orientation allowed to prevent the intrinsic torsion which normally accompanyies bending, as we found with the AniCryDe code [91], and to obtain a stronger anticlastic bending with respect to strip with (111) entry face, being the R_A/R ratio equal to 2.75 (see Table 2.2 and Ref. [82]). Prechar-acterization results are shown in Fig. 2.29(b) and Table 2.5. Anticlastic bending radius was found by multiplying the measured value of the principal radius for the R_A/R ratio. The angular acceptance for VR in a strip is equal to channeling angle, which can be estimated considering the l/R_A ratio. By combining this information with the measured relative misalignment of the strips, we estimated that 7 of 8 strips are aligned in such a way to provide multiple volume reflection within an angular range of about 125 μrad, as shown in Fig. 2.30.

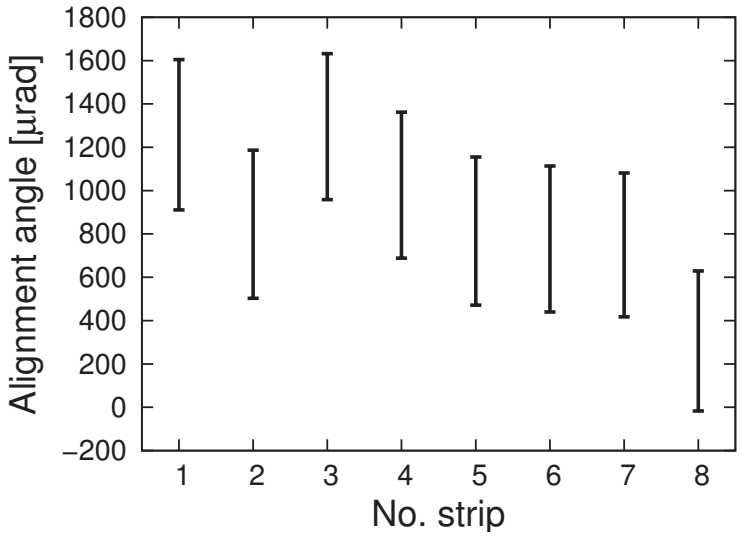

Figure 2.30: Alignment of single strips in multistrip MSTF13. Error bars represent the angular acceptance for VR in each strip. From this plot, we found angular region of about 125 μrad where 7 strips are aligned and can provide multiple volume reflection.

No. strip	R (m)	R_A (m)	CH angle (μrad)	Orientation (μrad)
1	0.67	1.84±0.09	695±35	1258
2	0.68	1.87±0.09	684±34	845
3	0.69	1.90±0.09	675±34	1295
4	0.69	1.90±0.09	675±34	1025
5	0.68	1.87±0.09	684±34	813
6	0.69	1.90±0.09	675±34	777
7	0.70	1.92±0.10	665±33	749
8	0.72	1.98±0.10	646±32	306

Table 2.5: White light characterization of the MSTF13 multistrip. Anticlastic bending (R_A) was obtained by multiplying the measured principal radius (R) for the R_A/R ratio, which is equal to 2.75 in this case, as explained in the text. for each strip, channeling angle corresponds to the VR acceptance used to estimate the MVR acceptance.

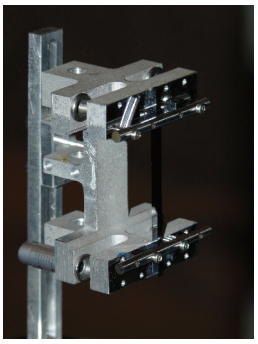

Parameter	ST1001
Channeling plane	(111)
Channeling axis	<110>
Thickness along the beam (mm)	2.00±0.02
Transverse thickness (mm)	2.00±0.1
Height (mm)	55.0±0.1
Bending angle (μrad)	160±20
Torsion (μrad/mm)	<2

Figure 2.31 & Table 2.5: Photo and parameters of the ST1001 crystal fabricated for the INFN CHANEL experiment

2.3.4 Strip crystal for negative particles manipulation

Strip crystals have been produced also for the INFN CHANEL experiment, which is devoted to the investigation of the dynamics of coherent interactions of negatively charged lepton beams, in particular electrons. Crystals have been optimized for operations at CERN-SPS H4 extracted beamline, where beams of electrons, hadrons and muons in the 10-400 GeV/c energy range are delivered. The length along the beam was reduced to be of the order of dechanneling length, which is of about 0.93 mm for 150 GeV-energy negative pions, and is a matter of study for electrons at this energy. At the same time, transverse thickness is maximized in order to improve statistics durig the experiment, and bending angle was chosen according to parameters given by the experimental setup. Moreover, crystalline direction was chosen to give the (111) planes for channeling. This choice was done to improve steering efficiency, since for negative particles the (111) planar potential well is deeper with respect to the (110) well.

2.4 Quasi-mosaic bent silicon crystals

For the crystal-assisted manipulation of charged particle beams, an alternative geometry based on the secondary curvature caused by the quasi-mosaic (QM) effect can be used. The quasi-mosaic effect is a secondary deformation caused by anisotropic effects, which was quantitatively explained for the first time by O. Sumbaev in 1957 in terms of crystal anisotropy [92], and was then fully explained by the theory of linear elasticity in an anisotropic medium [93]. The QM curvature may arise as a secondary curvature, where planes bent by the QM effect are orthogonal to the main surface of the plate.

Crystals exploiting the quasi-mosaic effect ("QM crystals") were introduced in channeling experiments after the first observation of high-efficiency extraction and collimation of a proton beam, which was carried out with a strip-like Si crystal through anticlastic deformation in 2001 [94]. In particular, QM crystals allowed the first experimental observation of volume reflection (VR) [19], which had been predicted for many years [18]. In contrast to the scheme based on anticlastic deformation [82], a QM crystal is positioned perpendicularly to the particle beam, as shown in Fig. 2.32. A QM crystal highlights two interesting features for channeling experiments. First, it allows the interception of a broad beam because the largest face of the crystal is exposed to the beam. Second, the thickness of a QM crystal along the beam direction can be adjusted down to a few tens of micrometres, which is a value not achievable in the case of traditional bent crystals. To maximize deflection efficiency, it is important to design crystals with optimized characteristics, e.g. the crystal length along the beam direction. An important parameter to quantify the channeling efficiency is the dechanneling length (see Sec. 1.1.4), which is the average length within which a channeled particle leaves the channeling condition with a probability of $(1 - 1/e)$ [2]. To efficiently steer a charged-particle beam, the crystal thickness must not be higher than the dechanneling length, which depends on beam energy. For instance, the use of QM crystals allowed the deflection of GeV-energy protons by means of a crystal with a thickness of less than one millimetre [95].

The property of QM crystals to be thinned to a very low thickness can be even more important when the channeling of negatively charged particles is concerned. Indeed, negative particles repeatedly oscillate across crystallographic planes/axes [42]. Thus, the probability of inelastic scattering of channeled negative particles by atomic electrons, and especially the probability of multiple scattering by lattice atoms, is much higher than that in the case of positive particles. The dechanneling length of 855 MeV/c electrons channeled in (110) silicon was estimated to be 18 μm at MAMI [96], while a dechanneling length of 0.93 mm was measured with 150 GeV/c pions at CERN [42]. The use of a QM crystal for steering negative particles was proposed by Guidi et al. [97]. Then, QM crystals were effectively used for

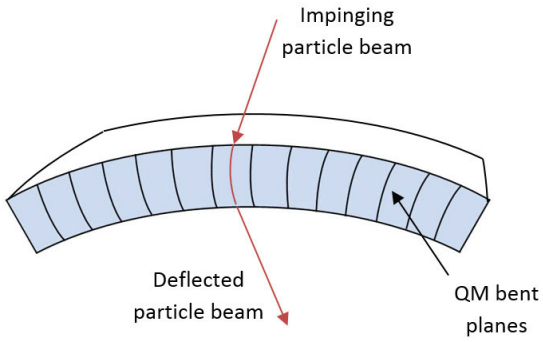

Figure 2.32: Schematic representation of a QM crystal used for steering a charged-particle beam.

this purpose in recent experiments at CERN [40], MAMI [70], and SLAC [72]. In these experiments, both channeling and VR were observed. QM crystals can also be used to study electromagnetic radiation emission accompanying coherent interactions [71].

In this section the manufacturing and characterization of bent silicon plates exploiting the quasimosaic bending is presented.

2.4.1 Fabrication technique

As described in Ref. [69], crystals were fabricated starting from a Silicon-On-Insulator (SOI) bonded wafers [98]. The SOI structure consists of a film of single crystalline silicon (device layer) separated by an electrical insulator, typically silicon dioxide (SiO_2) from the bulk substrate (handle layer). Crystals are obtained from the device layer, which must have very low thickness variations (TTV of $\sim$ 1 μm [99]). Thickness was chosen according to the required length of the crystal along the beam. The procedure of shaping is similar to the realization of silicon strips shown in Sec. 2.1.2. In more details, a 100 nm layer of amorphous silicon nitride (Si_3N_4) was deposited onto all the faces of the wafer through Low-Pressure Chemical Vapor Deposition (LPCVD). A rectangular pattern representing the shape of the final crystals was carved into the silicon nitride layer by means of a standard photolithographic technique [77]. The uncovered silicon areas, such as the entire silicon substrate and the interspace between the rectangles in the SOI layer, were etched with a KOH alkaline solution [78].

With this method, silicon crystals with the desired rectangular shape and a thickness from 10 μm to few mm can be obtained, without inducing any damage to the crystal lattice [65]. Particular care was necessary to handle with the thinnest plates in the last steps of the manufacturing procedure. The remaining Si_3N_4 and SiO_2 layers were finally removed in a HF solution. Figure 2.33 summarizes the

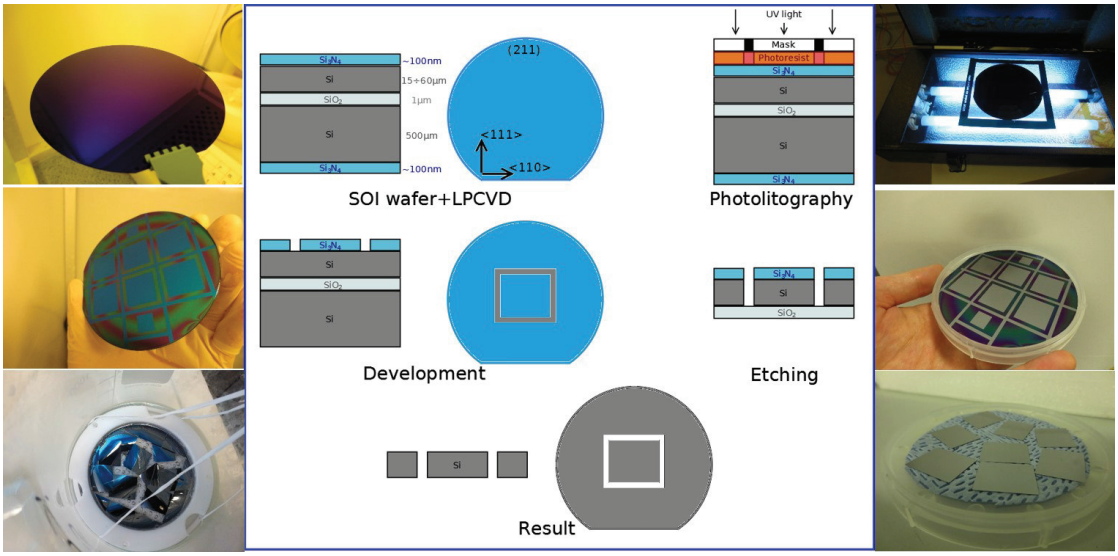

Figure 2.33: Realization of the plate-like silicon crystals (adapted from Ref. [69]). See text for the details..

manufacturing process for the realization of rectangular plate-like crystals from a (211)-oriented wafer with a ⟨111⟩- oriented flat.

2.4.2 Quasi-mosaic deformation

I here report some concepts of deformation of anisotropic materials that are necessary for understanding further modelling. A complete review of these concepts can be found in Ref. [100]. As a plate of anisotropic material is bent by a point-like mechanical couple of strength M_1 at the edges (see Fig. 2.34(a)), a deformation field (u,v,w) along the (x,y,z) directions, respectively, holds under the hypothesis of small deformations [84], as shown in Eq. 2.8 :

$$u = \frac{M_1}{2I_1}(2a_{13}xy + a_{36}y^2 + a_{35}yz) \tag{2.8a}$$

$$v = \frac{M_1}{2I_1}(-a_{13} + a_{23}y^2 + a_{33}(Lz - z^2) - a_{35}yz) \tag{2.8b}$$

$$w = \frac{M_1}{2I_1}(a_{35}xy + a_{34}y^2 + a_{33}y(2z - L)) \tag{2.8c}$$

where I_1 is the centre-mass inertia momentum of the plate in the x direction, a_{ij} the components of the compliance tensor, which are periodic functions of the crystal orientation. For an isotropic material, it holds a_{ij}=0 for either i $>$ 3 or

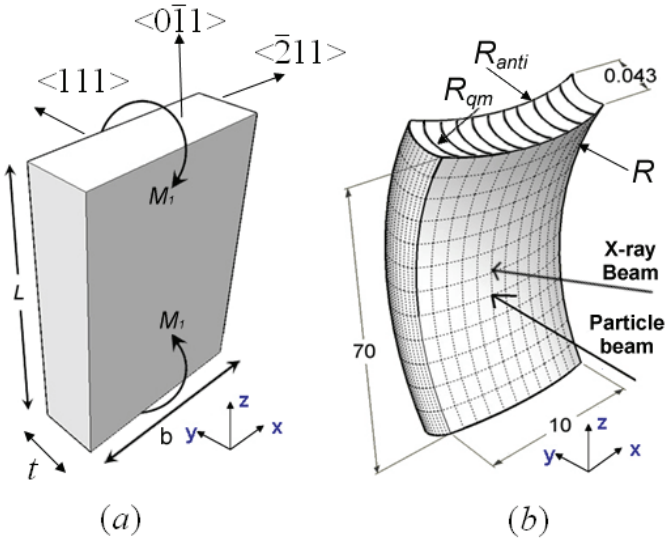

Figure 2.34: Sketch of the unbent silicon plate with height L and thickness t with the <111> crystallographic axis along y axis proposed for axial channeling studies in Ref. [97]. As a couple of forces with momentum M_1 is exerted at its edges crystal bends as in b. (b) External forces generate a primary curvature with radius R, which results in a secondary curvature with radius R_{qm} due to anisotropy-induced deformation. Unwanted anticlastic deformation with radius R_{anti} also appears as a result of primary bending.

j > 3 and i ≠ j. Anticlastic deformation, which have been already described in Sec. 2.2.1, yields a parabolic profile of deformation proportionally to a_{13}, i.e. $v \sim a_{13}x^2$, and arises in either crystalline and amorphous material. While for amorphous materials the coefficient a_{36} is always null, for monocrystalline materials it may be different from zero. In this case the couple of strength M_1 may deform the planes parallel to the coordinate plane y-z to a parabolic shape $u \sim y^2$ through coefficient a_{36}, as schematically shown in Fig. 2.34(b). This deformation is called "quasi-mosaic" (QM) [61]. If the crystal plate is cut with the crystallographic orientation as in Fig. 2.34(a), the calculation of the compliance tensor for Si shows that the a_{36} coefficient is not zero, so the QM-related bending radius equal to $R_{qm} = |a_{36}/a_{13}| \cdot R$ and anticlastic bending radius equals to $R_{anti} = |a_{33}/a_{13}| \cdot R$. Therefore, under small deformation regime, both anticlastic and QM deformations are expected in this geometry. For beam steering applications the presence of anticlastic deformation has negative effect because it limits the portion of the crystal aligned for channeling. A technique to rule out anticlastic deformation for which no external force is needed other than the bending moment M_1 was developed. In fact, anticlastic deformation can be prevented in the case of high-deformation regime, i.e., as Searle parameter β (see Eq 2.6) is much larger than the

unity. More precisely, anticlastic deformation is present on the full width of the crystal for $\beta < 1$ (low deformation regime, analytically described by Eq. 2.8) or is confined on the crystal edges for $\beta > 100$ (high deformation regime) [86, 101], so that the central part of the crystal remains flat. Indeed, since the use of very thin crystals is sometimes demanded because of short dechanneling length, the plate deformation regime may easily be attained and, in some cases, is even unavoidable (β is in fact inversely proportional to t).

In a dedicated study, reported in Ref. [97], a highly deformed silicon plate oriented as in Fig. 2.34(a) with b = 10 mm, L = 70 mm have been fabricated and characterized. The plate was diced from a 4 inches (111) Si wafer with low miscut ($< 0.05°$), thinned to t = 43 μm through a lapping machine. The crystal was bent through a mechanical holder, which ensured reproducible and stable bending. Dechanneling length for positive particles at 2 GeV in (110) silicon is about $L_D = 1$ mm, thereby for negative particles at the same energy it holds $L_D = 0.1$ mm, i.e., it by far exceeds the crystal length along the beam direction. The sizing of the crystal was suggested for operation with some GeV electron beam because there are worldwide many electron facilities operating at an energy of this order of magnitude (e.g., Refs. [102–104]), for which channeling experiments can not be performed with crystals fabricated for working with positive particles. Secondary curvature were investigated for crystals with a main radius of curvature down to 35.52 mm with a high-resolution X-rays diffractometer and the Veeco white light interferometer, respectively described in Sec. 2.2.3. Measurements revealed an anticlastic bending radius $R_{anti} = 3660$ mm on the centre of the sample, which confirms a strong reduction in anticlastic bending with respect to the predictions of small-deformation theory, for which R_{anti}, should be 173 mm. At the same time, QM curvature was found to be $R_{QM} = 148$ mm. By comparing this result to the theoretical value $R_{QM} = 121$ mm, which is the expected QM radius in the limit of the small deformation regime, one can see that the QM deformation is poorly (less than 20 %) perturbed by the high-deformation regime.

More recently we improved crystal design by exploiting the results of an analytical study aimed to the suppression of the anticlastic deformation of a bent plate. The method, which is fully explained in Ref. [105], shows that the crystal curvature in the anticlastic direction is a function of the crystal aspect ratio (length divided by width) and becomes zero at an aspect ratio dependent on the Poisson coefficient. The results of these calculations were used to design a holder for a thick QM crystal (thickness of about 0.5 mm) for the manipulation of hundred-GeV leptons at H4-SPS CERN. The dimensions of the plate were chosen to be respectively 43 and 28 mm. Such a solution was mandatory for this case, since a 0.5 mm thick plate can not be bent to the high-deformation regime exploited for anticlastic suppression of thin plates. By resizing lateral dimension of the plate

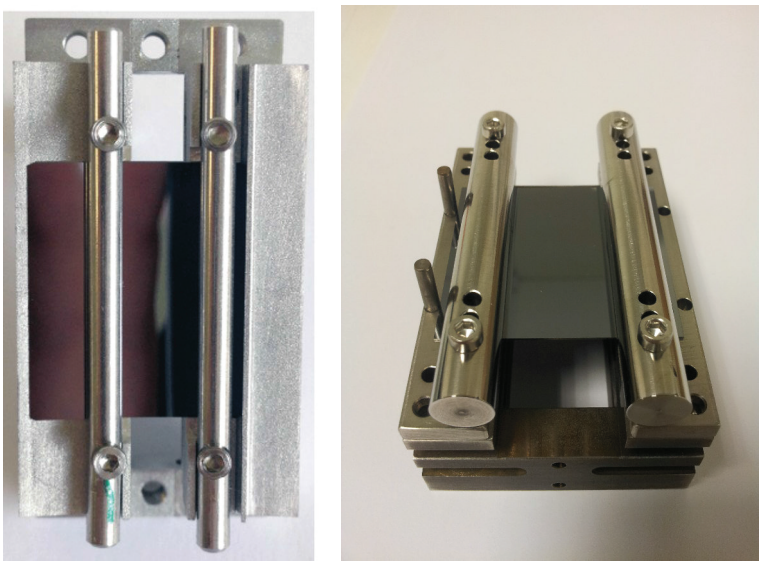

(a) (b)

Figure 2.35: (a) Photograph of bent crystals tested at SLAC. (b) Photograph of the thick QM Si sample shaped for CERN applications.

we were also able to furtherly optimize the dimensions of the newest thin crystals, which were shaped with the dimensions being respectively of 21 and 13 mm.

2.4.3 Bending devices

For channeling experiments we made use of quasi-mosaic crystals which were bent with an external holder capable of imparting a single mechanical moment to the crystal plate. The holder is typically made of duralumin or titanium; the latter is preferable if the holder has to be baked for ultra-high vacuum. As an example, we show in Fig. 2.35 the holder used for bending a QM Si crystal in an experiment performed at SLAC [72] and a bigger holder recently used to bent a thick plate ($\sim$ 500 μm) which was designed for high-energy applications.

Very recently, LNL has built a sample holder prototype aimed to bent the crystal with a remote controlled system that works in vacuum. The upgrade, never realized before, has 3 main aims:

1. giving access to the investigation of many curvatures without breaking the vacuum chamber. This will cause a considerable speed up of the data taking and a more extended set of data would be accessible;
2. the possibility to smoothly increase the curvature. This can be done with a numerical control in such a way to avoid stress concentrations and thus

preventing the breaking of the sample. Moreover, it is now possible to manage very thin and fragile samples, since the mounting and the bending steps were decoupled in this procedure;

3. the possibility to remotely correct distorsion. If the sample curvature is not perfect, the incoming angle for channeling could vary along the beam dimension (i.e. a local torsion) causing a detrimental effect on efficiency. The correction system is an additional degree of freedom which allows to compensate local torsion during the channeling experiment, while checking in real time the effect on the efficiency. This is by far the best procedure one can imagine for torsion correction that alternatively should be made off-line before the sample transport to accelerator facilities.

The system is composed of many parts, which were accurately studied, built and assembled as shown in Fig. 2.36(a). In more details, in grey you can see the piezo motor step that provides the translation of a movable part (green) with respect to a fixed one (brown). This operation can be done with 400 nm steps. On both parts, two plugs (steel cylinders, mounted as shown in Fig. 2.36(b)) are inserted. Each plug present a rabbet, where the sample is secured by means of a special gluing procedure. The plugs can freely rotate in brass holes, while being supported against vertical slipping by pins screws. The translation provided by the motor makes the two plugs getting closer, thus forcing the crystal to bent. Bending procedure, which is crytical when mounting thin plates onto fixed holders, can now be done more easily, and higher curvatures are now reacheable. Once having tuned bending radius, torsion can be finely compensated by tilting one of the plugs with a never ending piezo driven screw (yellow), which pushes a rotating part (magenta) containing the plug hole. The angular resolution of this rotation is less than 1 microradian. As shown in Fig. 2.36(b) a 15 micron thin sample was bent to a radius of curvature of 3 mm. The bending system was calibrated in order to know the primary curvature radius as a function of the number of steps of the translator motor (see Fig. 2.37). We also verified, by means of X-ray diffraction, the effective possibility to finely adjust torsion by means of the second motor. The system is ready to be installed at MAMI facility for the next channeling experiment.

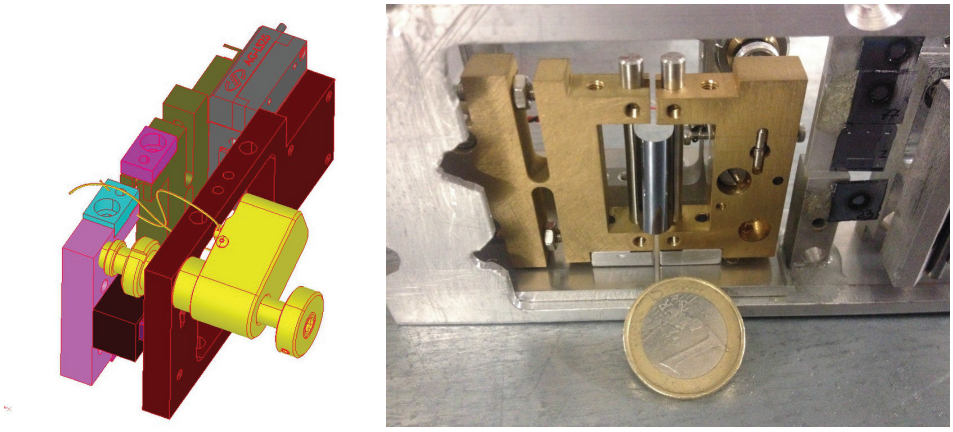

(a) (b)

Figure 2.36: CAD project 3D image of the holder(a). Photo of the realized object with a silicon sample of 15 micron thickness and 3 mm curvature radius (b). Courtesy of D. De Salvador.

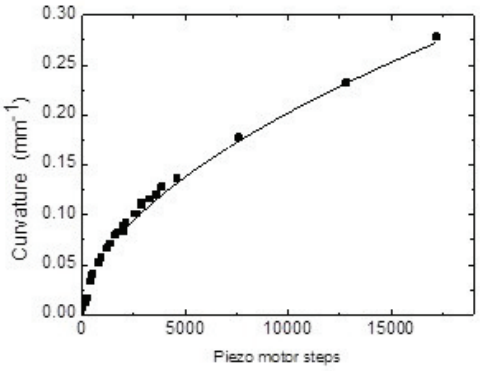

Figure 2.37: Curvature vs steps of the translator motor. Courtesy of D. De Salvador.

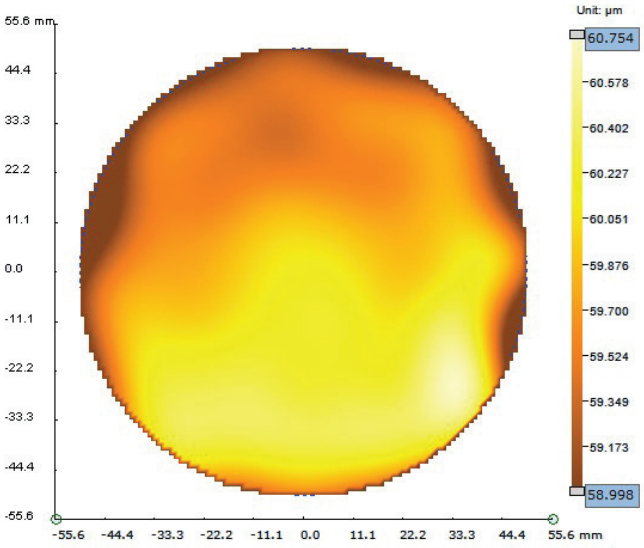

Figure 2.38: Map of the thickness of the SOI layer of the starting wafer (nominal thickness = 60 μm), performed with Fogale TMAP-4. The thickness was uniform enough to use this wafer for the production of QM crystals. Adapted from Ref. [69].

2.4.4 Characterization

Prior to experimenting the crystal on particle beams, a full set of characterizations were performed.

Firstly, infrared interferometry (Fogale TMAP-4) was used to map the thickness of the device layer in the SOI structure with nanometric accuracy. As an example, the result of such a measurement for a SOI wafer of 60 μm thickness is reported in fig. 2.38. This measurement on starting wafer is safe, since the SOI layer is supported and protected against breaking by the bulky frame.

After manufacturing and bending, white-light interferometry (Veeco NT1100) was employed to characterize the surface of the lowly-deformed bent crystals. This measurement allows to estimate principal- and anticlastic- bending. The result of the surface characterization of the QM crystal for CERN applications (see Fig. 2.35(b)) is shown in Fig. 2.39.

For highly-deformed crystals, surface characterization is not possible with the Veeco interferometer, since only a small part of a strongly bent surface can reflect light back into the microscope objective. However, being strongly-bent crystals very thin, they can be characterized in transmission mode with the X-rays diffractometer (Panalytical X'PERT MRD (XL)). In particular, a Rocking Curve (RC) measurement of the (111) planes was performed with a 8-keV X-rays beam delivered by a tube with Cu target through a Goebel mirror [89] followed

by a four bounch Bartels germanium monochromator [90]. The full widht half maximum of the rocking curve provides an estimation of the bending angle of the (111) planes. The RC characterization of the crystal studied in Ref. [72] is shown in fig. 2.40.

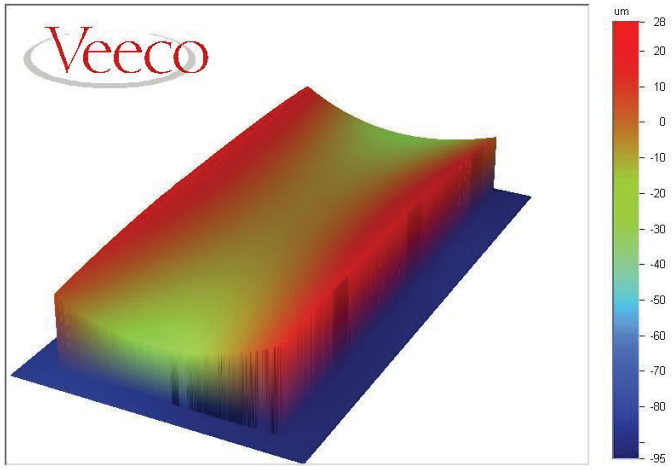

Figure 2.39: Surface characterization of the thick QM crystal used for CERN application, performed with white-light interferometry (Veeco NT1100).

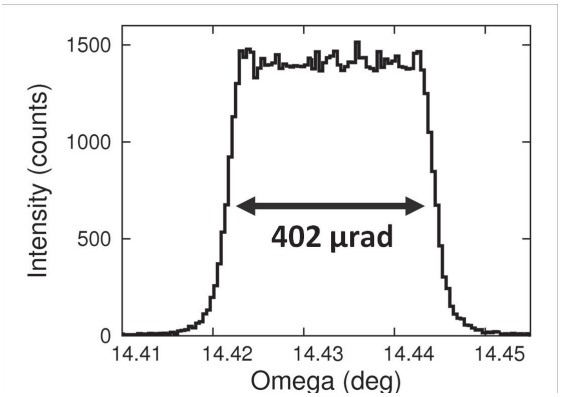

Figure 2.40: Rocking Curve measurement of the (111) planes. The measured crystal plate is 60 μm thick, therefore (111) planes are bent with a radius of 149 mm. Adapted from Ref. [69].

2.5 Thin flat silicon membranes

Membranes of micrometric lateral size and nanometric thickness offer wide opportunities in basic and applied research, as well as in technology, see e.g., the review [106]. In fact, such structures exhibit mechanical, electrical, thermal and optical properties which are unavailable in bulk materials [107–111]. Due to their limited lateral size such structures are very difficult to handle and to manipulate.

The technology of membrane fabrication has been exploited to produce thin straight crystals with micrometric-, and even nanometric- thickness for channeling experiments. Coherent interactions are studied in straight crystals mainly with the purpose of high-intensity production of electromagnetic radiation such as channeling radiation [112] and coherent bremsstrahlung [113]. Indeed, coherent interactions result in more intense and, in some cases, more monochromatic radiation generation than would occur for the case of conventional bremsstrahlung in an amorphous material [114].

In the recent past, thin membranes were employed for charged particle beam manipulation as an alternative scheme with respect to bent crystals. Indeed, the trajectories of charged particles confined under planar channeling regime [12] is characterized by oscillations whose wavelength (λ) is a function of the particle energy and the impact parameter on the atomic planes. For positively charged particles it holds $\lambda \sim d_p\sqrt{pv/2U}$, as shown in where d_p is the inter-planar distance, p the particle momentum, v the particle velocity and U the interplanar potential. Tsyganov and Taratin predicted the possibility to deflect 900 GeV/c protons by means of an unbent crystal with thickness equals half of the oscillation wavelength [115]. Only recently, thanks to the advent of sophisticated techniques for crystal fabrication [67], this mirroring effect was proven to work [66] for non-relativistic protons of 2 MeV kinetic energy in a 92-nm-thick Si crystal at the AN2000 accelerator of the LNL laboratories of INFN. Following this result, the effectiveness of the mirror effect for 400 GeV/c protons in a 26.5-μm-thick Si crystal has been studied in an experiment at the external lines of CERN-SPS [68], making the mirror effect an attractive alternative to bent crystals for efficient manipulation of high-energy particles.

I recently manufactured similar crystalline membranes for an experimental study aimed to demonstrate the incoherent scattering suppression by collision correlations in oriented crystals. In particular, crystalline membranes with a thickness of about 30 μm were produced for a scattering experiment with the sub-GeV electron beam available at MAMI. To do an effective comparison between scattering in misaligned crystals and amorphous silicon, we produced in collaboration with LNL some amorphous silicon membranes with the same effective thickness along the beam, i.e. the same number of atoms per unit of area. Since the effect we are seeking for corresponds to a fine correction, a particular care in sample prepara-

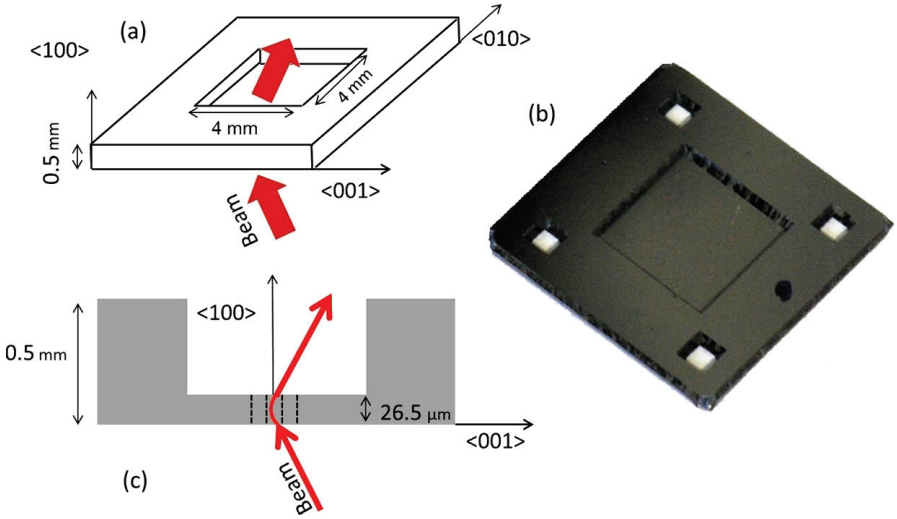

Figure 2.41: (a) Sketch of the ultra-thin Si crystal that highlights the crystallographic orientations; the arrows indicate the direction of the mirrored proton beam, which impinges on an active area 4 × 4 mm2 large and 26.5 μm thick, surrounded by a 500 μm thick frame. (b) Picture of the thin Si crystal. (c) Lateral view of the crystal, with crystallographic orientation highlighted; arrows represent the incidence and outgoing direction of particle beam mirrored by the Si (001) crystal planes (dashed lines). The figure is adapted from Ref. [68]. See text for the manufacturing procedure details.

tion, and a high precision in the estimation of all the experimental parameters, such as sample thickness and density, is demanded. In this section I will provide a description of the fabrication procedure and of the characterization methods for either crystalline- and amorphous- silicon membranes.

2.5.1 Fabrication of crystalline membranes

As described in Ref. [68], the prime material for crystalline membranes fabrication was a (100) oriented Si wafer. Starting wafer was then treated through techniques borrowed from silicon micromachining and described in Sec. 2.1.2. In particular, a Si crystal with lateral sizes of 4×4 mm^2 was fabricated via anisotropic etching [65] (see Fig. 2.41a). All the wafer surfaces were coated with 100 nm silicon nitride deposited through low-pressure chemical vapor deposition, which was then patterned through photolithography techniques to remove the coated film from selected areas. The lateral size of the crystal was optimized to obtain a thin silicon membrane surrounded by a bulky frame of 500 μm, in such a way to assure easy handling and to prevent deformations (or breaking) of the crystal during the channeling experiment. The wafer was immersed in a KOH solution, resulting in

thinning of the uncoated areas. A precise calibration of the silicon etching rate allowed stopping the thinning process once an ultra-thin silicon membrane with the desired thickness was left. Fig. 2.41b shows a picture of the Si membrane manufactured for proving the mirroring effect at CERN [68].

2.5.2 Fabrication of amorphous membranes

The prime material for amorphous membranes fabrication was a randomly oriented Si wafer. All the wafer surfaces were coated with 100 nm silicon nitride (Si_3N_4) deposited through low-pressure chemical vapor deposition. A 30 μm layer of amorphous silicon is deposed onto one side of the wafer by means of a sputtering deposition [116], provided by LNL. Due to the different thermal expansion coefficient between the silicon wafer and the deposited amorphous film, the cooling down of the crystal after the deposition is accompanied by a tensile stress on the Si substrate. This effect has been widely studied in silicon industry, since it is considered a parasitic effect of film deposition. In particular, as shown in Fig. 2.42, wafer assumed a cilindrical shape with a curvature radius of about 24 cm, measured with the Veeco white light interferometer. A thermal annealing procedure was done to relax the amorphous layer. The procedure cosisted on heating all the structure to 500°, and then on a slow cooling down, in order to avoid the formation of crystalline domains into the film. Once stress is relaxed, squared samples with 10 mm×10 mm of shape were diced with the DAD Disco 3220 available at SSL (see Fig. 2.43). Squared samples were then masked with Kapton tape in such a way to cover the entire sample except a circular spot of about 3 mm of diameter on the opposite side with respect to the amorphous layer, as shown in Fig. 2.44(a). In order to remove the bulky silicon in the region of the circular spot, we etched the whole crystal in an acid solution made of HF, HNO_3, and CH_3COOH (HNA) [117]. Such etching mixture is widely used in silicon micromachining. Nitric acid readily oxidizes Si to SiO_2, which is eroded by HF, acetic acid serves as a solvent and makes the reaction more controllable. Such etching mixture is particularly suited to etch silicon isotropically, i.e. with the same rate independently of the crystallographic orientation. Silicon etching proceeds through the reaction shown in Eq. 2.9.

$$3Si + 12HF + 4HNO_3 \rightarrow 3SiF_4 + 4NO + 8H_2O \tag{2.9}$$

The reaction proceeds till the bulky frame is completely removed in the region of interest. The amorphous layer is not etched by the HNA solution since it is protected by the silicon nitride layer, which acts as etch-stopper. Once done that, the etch-stopping layer is removed with HF, and Kapton tape is ripped out. With this procedure, thin amorphous Si membranes with a diameter of $\sim$ 3 mm

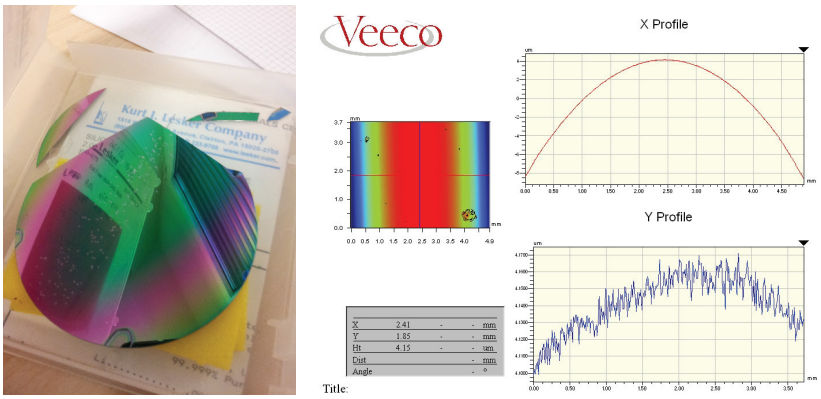

(a) (b)

Figure 2.42: Result of amorphous silicon deposition (a). Interferometric characterization of the surface shows a cylindrical profile with bending radius of $\sim$ 24 cm.

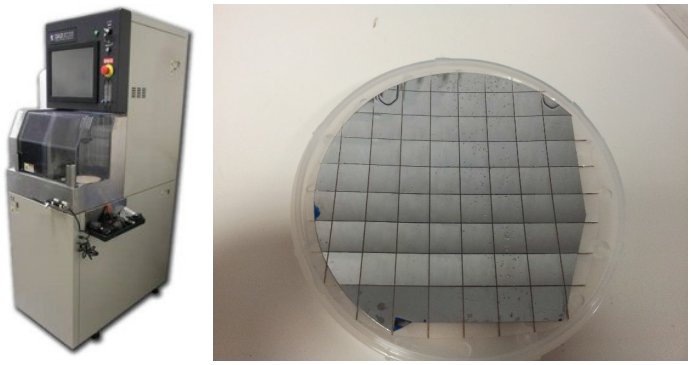

(a) (b)

Figure 2.43: Dicing machine DAD Disco 3220 (a) used to cut 10 mm×10 mm squared samples (b). This operation is done after the annealing process.

surrounded by a solid Si support are obtained, as shown in Fig. 2.44(b).

2.5.3 Characterization of membranes

Crystalline membranes realized for proving the mirroring effect have been characterized in the past by means of HRXRD and planar channeling of 2 MeV protons, as described in Ref. [67]. Such characterizations proved both the high crystalline quality of the membrane and the possibility to manipulate trajectories of high energy particle beams by means of unbent crystals.

Aimed to the study of incoherent scattering suppression in oriented crystal on which we are still working on, a precise determination the number of atoms in the

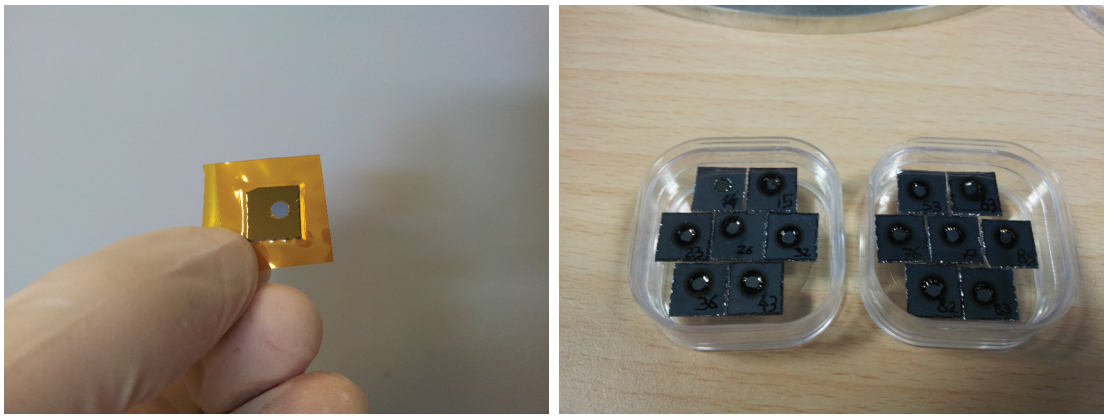

(a) (b)

Figure 2.44: Square samples masked with Kapton tape for wet etching (a). Final result of fabrication procedure (b).

beam direction both for amorphous and silicon is needed. To do that, I performed thickness and density measurements. A map of thickness of the entire membrane was measured with an infrared interferometer (FOGALE T-MAP 4, see Sec. 2.2.3 for more details on the instrument). Figure 2.45 shows a very fine thickness map (0.01×0.01 mm) of a crystalline membrane (a) and an amorphous membrane (b) respectively. The thickness of each membrane in the center of the samples was determined with a precision of less than 30 nm.

Beside, photon attenuation measurements were performed with a monochromatic and collimated 8-keV x-rays beam delivered by a high resolution X-rays diffractometer (Panalytical X'PERT MRD (XL)) into the center of the membranes, as schematically shown in Fig. 2.46. Photon intensity attenuation can be described with the Beer-Lambert law [118], i.e. the intensity as an exponential function of traversed distance, as shown in Eq. 2.10.

$$I = I_0 \exp(-\mu_l x) \tag{2.10}$$

Several cycles of intensity measurements (I, integrated over a long period to improve statistics) were done. Such measurements were alternated with direct beam intensity measurement (I_0) in order to compensate the unavoidable drift of the beam intensity which normally occours during data taking. Moreover, an angular scan of the sample orientation was done for crystalline membranes, in order to avoid solid states effects in crystals, as explained in Ref. [119].

Finally, by combining thickness- and x-rays attenuation- measurements, we were able to estimate the linear attenuation coefficient, which is proportional to the density of the sample. In particular, for crystalline membranes the coefficient

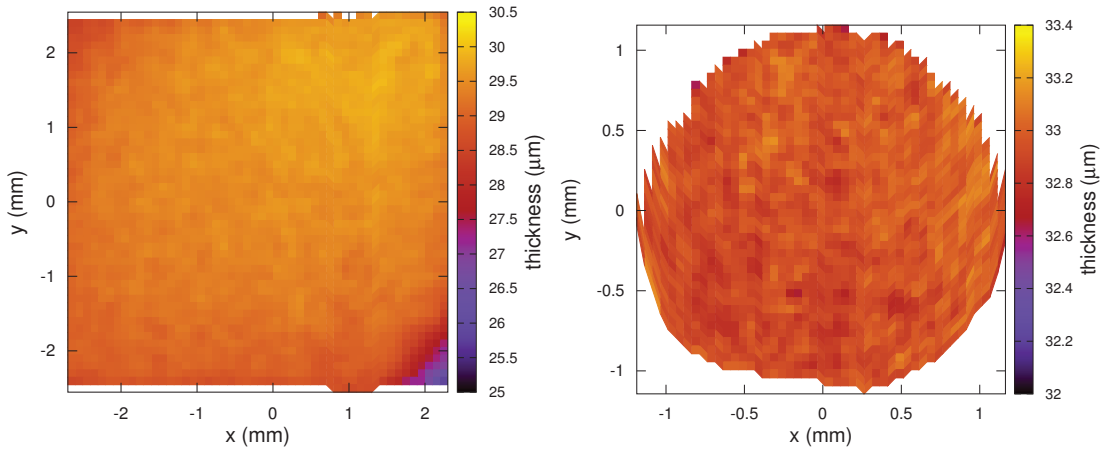

Figure 2.45: Thickness measurement of a Si crystalline membrane (a) and an amorphous membrane (b) performed with FOGALE T-MAP 4 Infrared Interferometer.

was estimated to be $\mu_l = (143.83 \pm 0.06)\mu\text{m}^{-1}$, which is in good agreement with the abundant literature on the topic, reported in a review by Creagh [120]. For the amorphous specimens, density was found to be about 4% higher with respect to crystal. This result was found for all the samples obtained with one deposition. Results of characterization are reported in Table 2.6.

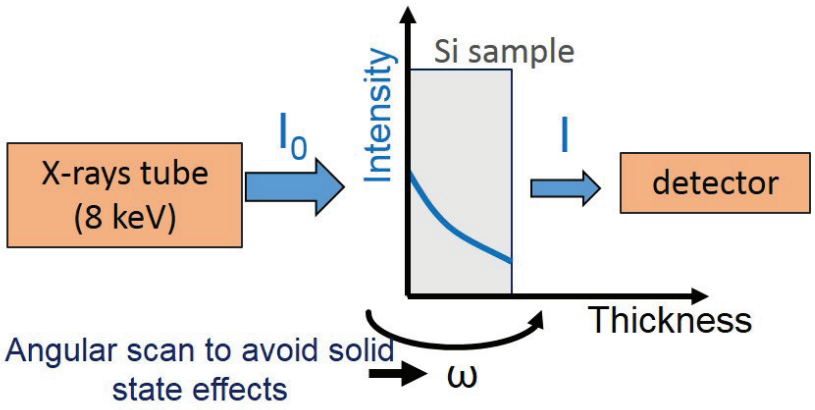

Figure 2.46: X-rays attenuation measurement through silicon membranes.

	Attenuation	Thickness (μm)	Density (/Cry02)
Cry02	0.61165±0.00009	34.179±0.011	1.0000±0.0004
Cry08	not measured	29.325±0.018	same of Cry02
Amo23	0.67181±0.00009	26.666±0.026	1.0372±0.0010
Amo77	0.61039±0.00009	32.951±0.005	1.0416±0.0003
Amo83	0.64213±0.00008	29.717±0.021	1.0363±0.0008

Table 2.6: Characterization of crystalline- and amorphous- silicon membranes.

Chapter 3

Coherent interactions of sub-GeV and GeV electrons for beam steering and high intense e.m. radiation generation

Crystal assisted beam manipulation has been extensively investigated for positively charged particle beams, spanning from MeV [66] to 1 GeV [19], to hundreds GeV [94] up to TeV energies [121], while, comparatively very little has been achieved concerning the steering of negatively charged particle beams via channeling in bent crystals. In fact, the trajectories of channeled positive particles are bounded far from the region with the highest atomic density, therefore they do not significantly suffer collisions on them. On the contrary, negative particles repeatedly oscillate across the crystallographic planes/axes, leading to a higher dechanneling probability with respect to positive charges [42]. In first experiments attempting the steering of negative-particle beams through bent crystals, all the channeled particles were scattered out of the crystal and no particle arrived at the angle of the nominal deflection of the crystal [122, 123] because crystals with length much larger than the dechanneling length were used. Only few years ago, the possibility to steer negatively charged particle beams through bent crystals at the full bending angle was demonstrated with 150 GeV- energy pions at CERN [39–41].

Manipulation of negative charged particles at $\sim$ GeV energy with bent crystals is of special interest, since the possibility to steer sub-GeV and GeV electron beams via channeling and VR in bent crystals would open up a new challenge for e.m. radiation generation in bent crystals within the energy range accessible by many electron accelerators worldwide. In fact, there is some wealth of data concerning the radiation emitted by electrons in straight crystals in the sub-GeV/GeV energy range interesting for X- or γ-ray sources, while no data for radiation with bent

crystals does exist in the literature. Among the possible applications, the crystal-assisted collimation in future $e^{\pm}$ colliders will be possible by combining beam steering and intense radiation generation. Moreover, the radiation accompanying volume reflection (VR) in curved crystals can be exploited for a γ-source with low-emittance beams. The few existing studies on VR radiation have been done with hundreds-GeV beams [31, 124–127], while only recently first results with sub-GeV electron beams were achieved by our group [71]. Furthermore, an elective application is the realization of a periodically bent crystals acting as an innovative high-intensity radiation source [33, 35, 128, 129], for which a better understanding of particle dynamics in bent crystals and the accompanying radiation emission is demanded.

Our group has been involved in a campaign of coherent interactions experiments in the last few years in the framework of the INFN CSN V experiments Ice-Rad (2013-2014) and Chanel (2015-present). I was involved in this campaing since the beginning of my phD for the manufacturing and characterization of the crystals used, and for the active participation to data taking at MAMI. In this chapter, experimental results about beam steering and radiation emission obtained with sub-GeV electrons at MAMI (adapted from Refs. [70, 71, 130] and with GeV electrons at SLAC (adapted from Refs. [72, 131]) were reported.

3.1 Experiment with sub-GeV electrons at MAMI

3.1.1 Experimental setup at MAMI B

The MAMI complex [103] is a normal conducting continuous wave 4-stage electron accelerator located at the Institute for Nuclear Physics at the University of Mainz (Germany). It consists in a pre-accelerator (a radio frequency Linac up to 3.7 MeV) and a 4-stage acceleration cascade based on three RaceTrack Microtrons (RTM1-3) and the Harmonic Double Sided Microtron (HDSM18) [132]: it delivers 100 μA high quality electron beams with a maximum energy of 1.5 GeV. The typical energy value used for channeling studies is 855 MeV with an emittance of $\epsilon_h = 0.01$ mm mrad and $\epsilon_v = 0.001$ mm mrad in the horizontal and vertical directions, respectively. The beam was focused through dedicated quadrupole lenses/. The resulting dimension and divergence were estimated by the MAMI group with a custom beam optic program taking into account the beamline magnets current and the distance between the two vacuum chamber stations, and are respectively, $\sigma_h \sim 230$ μm and $\sigma'_h \sim 50$ μrad in the horizontal direction and $\sigma_v \sim 30$ μm and $\sigma'_v \sim 40$ μrad in the vertical one. A schematic view of the experimental setup, installed after the third acceleration stage, is shown in Figure 3.1. The main feature are the following.

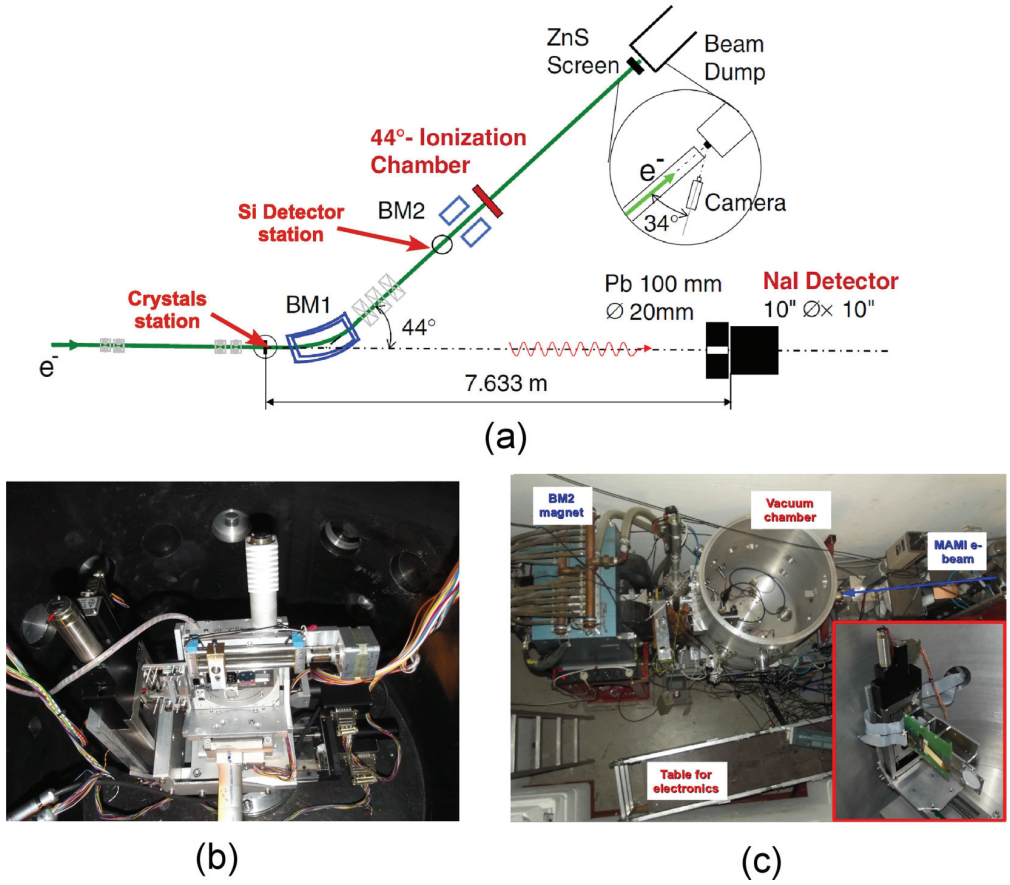

Figure 3.1: The experimental setup at MAMI. (a) A schematic top view with the electron beam coming from the left; both the deflection and the radiation parts are shown. Photo of (b) the crystals and (c) the Si detector stations. Adapted from Ref. [130].

- The 855 MeV electron beam coming from the RTM3 acceleration stage encounters a first vacuum chamber where the samples are installed on a high precision goniometric system (Figure 3.1(b)); the goniometer (from PI-MICOS33) allows 2 linear and 3 rotational degrees of freedom; the rotational stage around the vertical axis has a 2×10^{-4} deg repeatability while the tilting and the one around the beam axis have a 10^{-3} deg and 3×10^{-3} deg repeatability, respectively.
- The charged beam after the crystals is deflected by the BM1 magnet to the Si detector station provided by INFN Milano Bicocca (Figure 3.1(c)): a silicon profilometer has been mounted on a couple of remotely controlled motors (red inset in Fig. 3.1(c)), to adjust its position with respect to the incoming beam, and placed in a vacuum chamber.

- As far as the neutral particle beam is concerned, the photons produced in the interaction with the crystals follow a straight line of ~ 8 m and are detected by a NaI detector coupled to standard PhotoMultiplier Tubes (PMTs14) provided by the MAMI facility.

More technical details about the setup can be found in Ref. [130], which represents an upgrade of the MAMI setup described in Ref. [96].

3.1.2 Steering of sub-GeV electrons

I here show the results achieved by my group concerning beam steering, which are reported in Ref. [70]. An 855 MeV electron beam, available at the MAMI B facility, was conditioned to a beam size of 200 $\times$ 70 μm^2 and a divergence of 70- and 30- μrad along the horizontal and vertical directions, respectively, i.e., much less than the planar critical angle, being about 217 μrad at 855 MeV for the Si (111) planes.

A bent crystal suited for steering of sub-GeV electrons was manufactured at the Sensors and Semiconductor Laboratory (SSL) of the University of Ferrara as explained in Sec. 2.4 and Ref. [69]. It consists of a plate-like Si crystal with (30.5$\pm$0.5) μm thickness along the beam. These crystallographic orientations were selected to obtain (111) bent planes, which are the most efficient for the deflection of negative-charged particles. The 30.5 μm thick crystal was mounted onto a mechanical bending holder. A bending moment supported the crystal at two opposite edges, while it was free at the remaining edges. As one can see in Fig. 3.2, the crystal surface, which is parallel to the (211) planes, was bent along the <111> direction. In this way a secondary bending of the (111) planes was obtained due to the quasi-mosaic effect [61]. The crystal was characterized by high-resolution x-ray diffraction (Panalytical X-Pert MRD-PRO), measuring a bending radius of 33.5 mm, being approximately 23 times the critical radius for electron channeling at 855 MeV (R_c = 1.5 mm). The crystal lateral sizes were optimized to suppress parasitic anticlastic deformation across the central region of the crystal [97]. The small dimension of the beam ($\sim$ hundreds microns) as compared to the crystal surface (23 $\times$ 15 mm^2), assures that the whole beam impinged onto a uniform flat surface.

In order to excite coherent interactions between electrons and the crystal, the latter was rotated around the x-axis and, for each angular position, the particle distribution after the interaction with the crystal was recorded. The dedicated experimental setup allows the separate observation of channeled and dechanneled particles, which cannot be afforded by operating with a straight crystal. The particle distribution after interaction with the crystal as a function of the crystal-beam angle is shown in Figure 3.3. The recorded pattern very much resembles the results of a study about the interaction between a bent crystal and negative pions

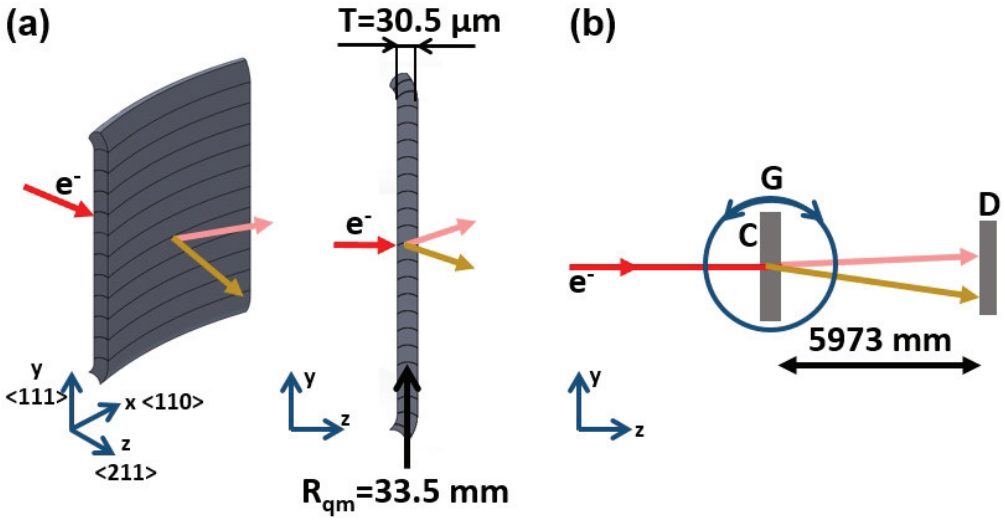

Figure 3.2: (a) Bending of a silicon plate-like crystal with properly chosen crystallographic orientations generates the quasimosaic effect, resulting in a secondary bending of the planes lying in the crystal thickness. (b) Sketch of the experimental setup. The dashed arrow indicates the incoming beam, impinging on the crystal mounted on a high-precision goniometer (G). The solid-black arrow indicates particles deflected thanks to planar channeling, while solid-white arrow correspond to overbarrier particles. A silicon detector, (D), reconstructs the beam profile after interaction with the crystal. Adapted from Ref. [70].

carried out at an energy more than two orders of magnitude higher than for this experiment [40, 133]. In particular, in regions (1) and (6), beam trajectory is never tangent to the crystalline planes so that coherent interactions are prevented. In region (2), the crystal is oriented for channeling, which arises as the beam impinges onto the crystal planes at an angle less than the critical angle for channeling (see Fig. 3.3b). Under such conditions, particles transverse motion is governed by the interatomic potential averaged along the crystal planes. However, due to multiple scattering, channeled electrons may be subject to an increase in their transverse energy and overcome the interplanar potential barrier, resulting in dechanneling (region 3). The inverse of such a process may occur, too, i.e. a non channeled electron loses part of its transverse energy due to multiple scattering and gets trapped in channeling mode. This effect is referred to as rechanneling. Aside from channeling, VR and volume capture (VC) (regions (4) and (5), respectively) manifest themselves as the trajectory of the beam becomes tangent to the bent atomic planes inside the volume of the crystal (see Fig. 3.3c). Particles subject to VR are reflected by the atomic planes, being deflected to the opposite side as that of crystal bending. In contrast, particles subject to VC are captured into the

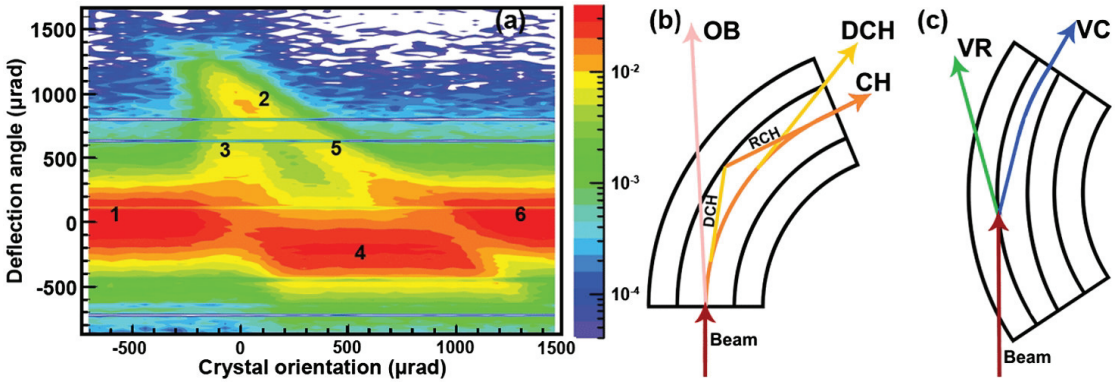

Figure 3.3: (a) an angular scan recorded during the interaction between the crystal and the 855 MeV electron beam. Six regions each, can be distinguished: (1) and (6) non-channeling regime; (2) channeling; (3) dechanneling; (4) volume reflection; and (5) volume capture. (b) The bent crystal is aligned with respect to the charged particle beam (red straight arrow) to excite planar channeling. Over-barrier particles are deflected toward the opposite side as that of crystal bending. Under-barrier particles are captured under the channeling regime (orange arrows). Due to multiple scattering, channeled particles may suffer dechanneling (yellow arrow). A fraction of dechanneled particles experiences rechanneling (RCH). (c) Bent crystal is aligned with respect to the incoming particle beam (red arrow) in such a way that the beam trajectory becomes tangent to the atomic planes inside the crystal bulk. Under such regime, either VR (green arrow) or the competitive process of volume capture (blue arrow) occurs. Adapted from Ref. [70]

channeling regime inside the crystal volume. This phenomenon has an angular acceptance equal to the crystal bending angle, unlike channeling, in which the angular acceptance is limited by the critical angle.

Figure 3.4 shows beam profiles under either channeling or VR alignment (black curves) as compared with the predictions of Monte Carlo simulations (red curves). The code uses an inter-planar potential based on measured atomic form factors for Si [134] and solves the equation of motion for the electrons interacting with the crystal. More information about the code is in Ref. [135] and references therein.

In Fig. 3.4.a, the peak on the right corresponds to the particles deflected under channeling. A Gaussian fit of the distribution highlights a deflection angle of 910±5 μrad. The fraction of deflected particles within $\pm 3\sigma$ around the channeling peak was 20.1±1.2%, a value in agreement with the simulation results (21.2%). The left peak is due to deflection of over-barrier particles , whose distribution is centered to the opposite direction as that of channeling. The distribution is asymmetric because of the contribution of rapidly dechanneled particles on the right side. The beam profile recorded for channeling was fitted as the sum of two gaussians and one exponential curves. The decay constant of the exponential term provides a

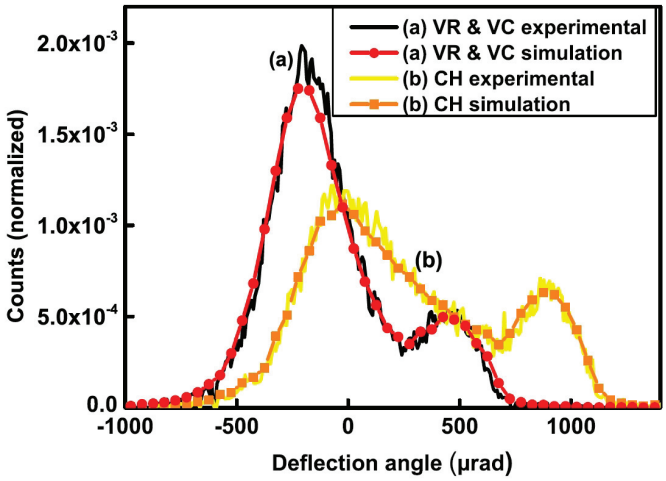

Figure 3.4: (a) Beam profile with the crystal aligned for channeling. The left peak (with maximum at $\sim$ -20 μrad) corresponds to over-barrier particles, which are slightly deflected to the side opposite to the crystal bending, the right peak owes to channeled particles. (b) Beam profile with the crystal aligned for VR. The left peak corresponds to volume-reflected particles and the right one corresponds to particles subject to volume capture. Adapted from Ref. [70].

direct experimental determination of the dechanneling length, which results to be 19.2 ± 1.5 μm. Fig. 3.4.b shows the deflection occurring as the crystal is oriented about on the middle of the VR region (450 μrad far from the channeling peak). A Gaussian fit to the reflected beam distribution yields a deflection angle of 191 ± 10 μrad with an efficiency of $76.7 \pm 1.\%$, in agreement with the prediction of the Monte Carlo simulation (75.8%). As expected, VR occurs with lower efficiency with respect to higher-energy experiments [40, 49], because of larger probability of competitive VC at lower energies [136]. In fact VC is aided by incoherent scattering, which favors the transition from over-barrier to channeling states, and that becomes stronger at lower energies [135].

Montecarlo simulations highlight also the contribution of both single and multiple rechannelings to build up the channeling peak of Fig. 3.4a. Figure 3.5 shows the fraction of channeled particles with and without taking into account the fraction of rechanneled electrons. About 55% of the particles recorded under the channeling peak has been rechanneled at least once. Analysis of simulations output shows that the dechanneling length causing an e-fold of the fraction of channeled particles for permanently channeled electrons (black-line in Fig. 3.5) is $L_{n,p} = 13.6$ μm. Dechanneling length becomes $L_n = 19.5$ μm if the total fraction of channeled particles, including the rechanneled ones, is considered (red line in Fig. 3.5). The latter value is in good agreement with the experimental result. In

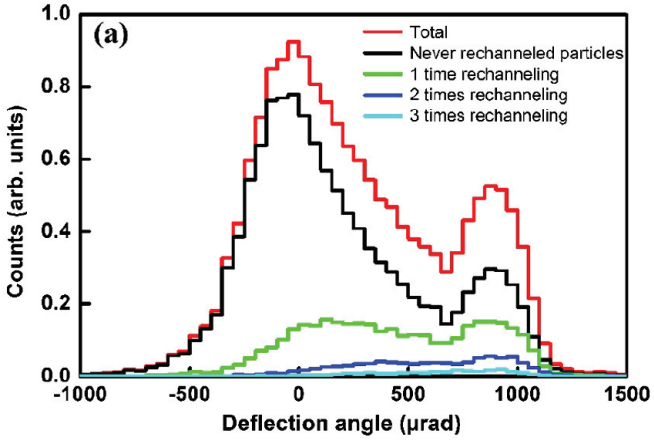

Figure 3.5: Monte-Carlo simulation of the contributions to the angular distribution originated from rechanneled particles. The red line represents the whole distribution; black line represents the particles that have never been rechanneled; green, blue and light blue lines represent the distribution of the particles rechanneled 1, 2, 3 times respectively. Adapted from Ref. [70].

particular, the strong contribution of rechanneling is expected from the reversibility rule (see Sec. 1.1.4). As there are particles that exit from the crystal channel, there have to be particles entering the channel. Since for channeled negative particles, the possibility of suffering dechanneling is increased than for positive charges due to the strong contribution of multiple scattering with nuclei, the same has to be for rechanneling, which is caused by the same phenomenon. If the particle dynamics is strongly influenced by the incoherent scattering, the same should be for the process of radiation emission. This led us to perform the radiation study reported in the next section.

3.1.3 Electromagnetic radiation emitted by Sub-GeV Electrons in a Bent Crystal

The results of the radiation study presented in this section are reported in Ref. [71]. The experimental layout is the same used for the experiment described in the previous sections, i.e. an 855 MeV electron beam delivered by the MAMI accelerator to the 30.5 μm-thick crystal already employed for beam steering measurement. The photons emitted by the electrons inside the crystal were separated by the charged beam through a bending magnet, and after 8.627 m arrived at a 25.4 $\times$ 25.4 cm^2 NaI scintillator detector. An aperture of 40-mm diameter in the lead shield surrounding the detector permitted the collection of a portion of the emitted photons, resulting in a collimator aperture of 4.63 mrad, i.e., equal to $\sim$7.8 times

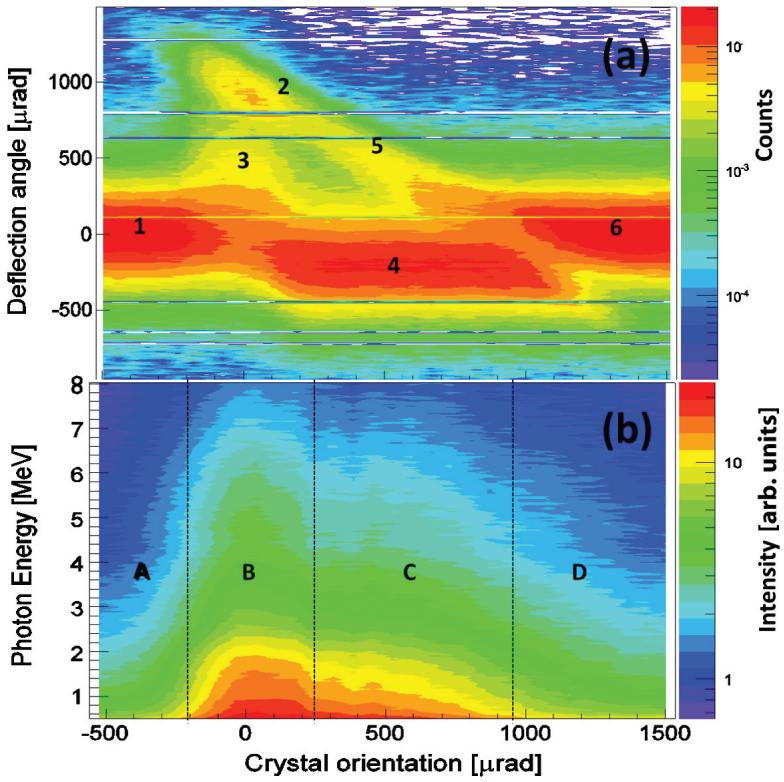

Figure 3.6: (a) Experimental deflected beam distribution vs. the incoming angle with respect to the bent (111) planes. The numbers 1-6 on the figure highlight different regions of interest: (1) and (6) crystal is misaligned, (2) channeling, (3) dechanneling, (4) VR, and (5) volume capture (VC). (b) Experimental radiation spectrum vs. the incoming angle with respect to the bent (111) planes. Regions (A) and (D) correspond to the nonchanneling case, (B) is for channeling and (C) for VR. Adapted from Ref. [71]

the $1/\gamma$ angle, for collection of most of the emitted photons. Before measuring the radiation spectra, the particle dynamics were investigated in order to ensure the proper experimental conditions for channeling and VR, while probing, at the same time, the steering capability of the crystal (see previous section).

A calibration of the detector was done as described in Ref. [137] by using the natural radioactive isotopes ^{40}K (1.461 MeV) and ^{208}Tl/^{228}Th (2.6146 MeV) which are impurities in the detector itself and in the surroundings. Then the electron beam was set at 855 MeV and the emitted photons after interaction with the crystal in random orientation have been collected by the scintillator detector. After the subtraction of the background contribution, the pure photon spectrum of emitted radiation by electrons inside the crystal is obtained.

The crystal was then rotated around the x axis and, for each angular position

(one every 0.003 degrees $\approx 52\,\mu$rad), the photon spectrum after interaction with the crystal was recorded. The experimental radiation spectrum after interaction with the crystal as a function of the crystal-to-beam angle is shown in Fig. 3.6(b). The regions (A) and (D) correspond to the nonchanneling case, (B) is for channeling and (C) for VR. For comparison, Fig. 3.6(a) displays the outgoing angle from the crystal as a function of the beam orientation with respect to the (111) planes. A direct comparison between the distributions of Figs. 3.6 (a) and (b) shows that radiation intensity is stronger than for the misaligned case (regions A and D) within all the angular acceptance of VR (corresponding to region (C)). Nevertheless, the most intense region is represented by channeling radiation (CR) of region (B). Since it is not possible to tag each photon with the deflected particles, we can not separate experimentally the contribution of volume-captured particles in radiation accompanying VR (region (C) in Fig. 3.6(b)) or the contribution of dechanneling in the CR of region (B) in Fig. 3.6(b).

Figure 3.7 (a) shows the experimental spectra for channeling (α-curve), VR (β-curve) at an incidence angle θ_{in} equal to 493 μrad from the channeling condition, and far from the (111) bent planes, at $\theta_{in} = 8726$ μrad (γ-curve). The intensities for both CR (α) and radiation accompanying VR (β) are stronger than for the case far from the bent (111) planes (γ). The experimental spectra represent the total radiation collected by the NaI detector that is proportional to the number of photons by unit time and energy. For the sake of comparison with the spectra normally displayed in the literature, Fig. 3.7 (b) highlights the spectral intensities obtained by multiplying the experimental spectra in Fig. 3.7 (a) by the photon energy, E. The spectral intensity of CR peaks for photon energies close to 1.8 MeV, which appears also in the case of VR, though less intense.

For the interpretation of experimentally recorded patterns, Monte Carlo simulations with the extension of the DYNECHARM++ code [138] including the routine RADCHARM++ for radiation computation [137, 139] were performed. The simulated spectral intensities $E(dN/dE)$ vs. E, dN/dE being the photon emission probability, for channeling (circles), VR (down triangles) and misaligned cases (stars), are also displayed in Fig. 3.7(b), showing a good agreement with experiments both in the shape and amplitude. The difference in the y-scale between experimental and simulated spectra is due to the fact that in the first case the whole radiation collected by the NaI detector is shown, while the latter represents the photon emission probability. The Monte Carlo code allows one to investigate the influence of the incoherent scattering on the process of photon emission, similarly of what has been done for particle steering. Figure 3.8 shows the simulated spectral intensity for channeling (circles and squares) and VR (down- and up-triangles) by taking (circles and down-triangles) or not taking (squares and up-triangles) into account the incoherent scattering. For comparison, the simu-

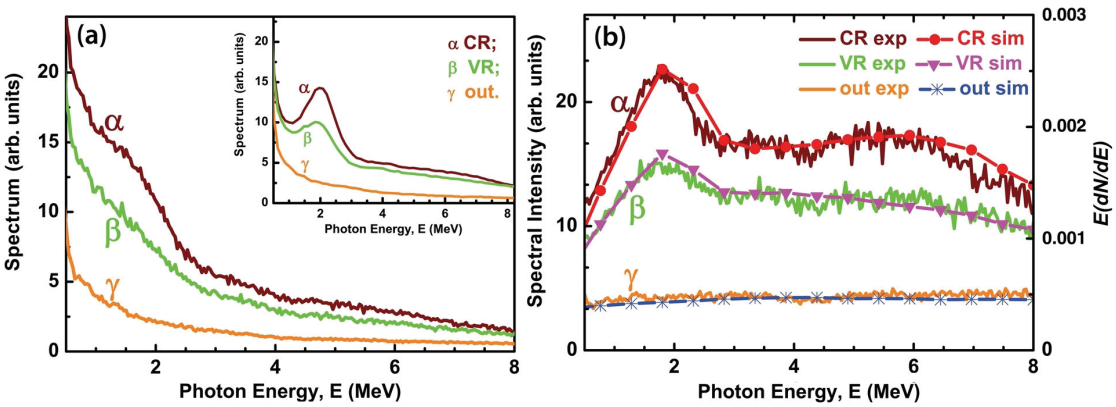

Figure 3.7: (a) Experimental radiation spectra (solid lines) for the cases of channeling ($\theta_{in} = 0$ μrad, α), VR ($\theta_{in} = 493$ μrad, β), and far from (111) bent planes ($\theta_{in} = 8726$ μrad, γ). Beam-off background has been subtracted. The experimental scale has been chosen from 0.5 MeV to 8 MeV to select the region of interest for CR. Inset of Fig. 3.7(a): experimental radiation spectra obtained with a smaller collimator aperture (4 mm instead of 40 mm) compared to Fig. 3.7(a). (b) Experimental (left scale) and simulated (right scale) radiation spectral intensities obtained by multiplying the experimental spectra in Fig. 3.7(a) by the photon energy E for the three cases. The photon emission intensity for one electron, $E(dN/dE)$, has been obtained averaging over 1000 trajectories. Adapted from Ref. [71]

lated incoherent bremsstrahlung (Bethe-Heitler) value is also shown (diamonds) on Fig. 3.8. One can notice that CR is suppressed by the effect of incoherent scattering. Indeed, incoherent scattering may lead to the dechanneling of the electrons, which causes a strong reduction in the CR intensity. On the contrary, in the case of VR the emitted radiation is intensified by the incoherent scattering, especially in the region of the CR peak. This fact has to be ascribed to the contribution of the volume-captured particles, which undergo a dynamics similar to that of channeled particles after the capture into the channel, resulting in a similar radiation process.

Through simulation it was found that the 32% of the total number of electrons are volume-captured, while the rest of thebeam particles (68%) was purely volume-reflected. Fig. 3.9 displays the contribution to the radiation accompanying VR (down triangles) of the volume-captured (circles) and the purely volume-reflected (up triangles) particles. The first case, presented in Fig. 3.9 by circles, shows the simulated spectral intensity calculated by averaging over the 32% of VC electrons. One can notice a much more peaked spectral intensity, which is typical for channeled particles, as compared to the case of the total radiation accompanying VR (down triangles). The second case, presented in Fig. 3.9 by up-triangles, shows

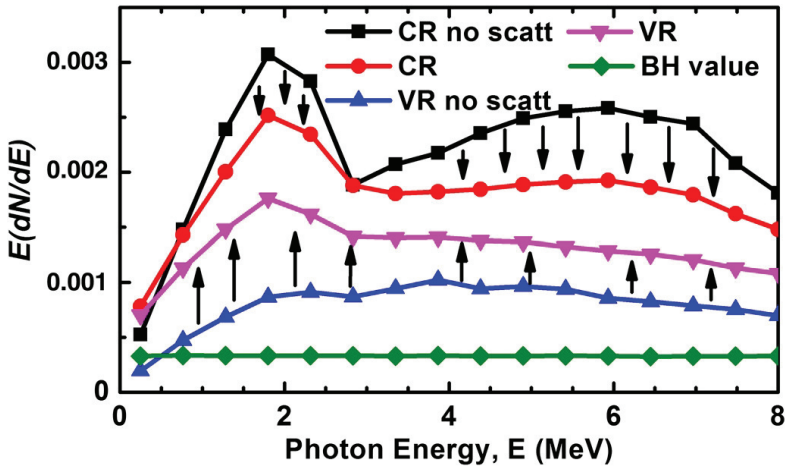

Figure 3.8: Simulated spectral intensity $E(dN/dE)$ vs photon energy E for channeling (circles and squares) and VR (down and up triangles) by taking (circles and down triangles) or not taking (squares and up triangles) into account the incoherent scattering. For comparison, the simulated Bethe-Heitler value is also shown (diamonds). The arrows directed downward underline the intensity decrease for CR caused by the incoherent scattering. The arrows directed upward underline the intensity increase, due to incoherent scattering, for the radiation accompanying VR. Adapted from Ref. [71]

a smeared spectral intensity calculated by averaging over the 68% portion of the total electrons that never fall into the planar well. The absence of sharp peaks in the spectra is ascribed to the change in the angle between particle trajectory and crystal planes, which decreases as the particle approaches the reflection point [137]. The changes in the alignment between particle trajectory and crystal planes result in a smearing of the coherent bremsstrahlung-like (CB) radiation spectrum typical of over barrier particles [31, 124, 140]. In summary, Fig. 3.9 highlights the contribution of VC particles, which maintains the electromagnetic radiation accompanying VR close in intensity to that for CR over the whole angular acceptance (see Fig. 3.6(b)). Finally, it is also important to highlight how the changing in the spectral intensities of Fig. 3.8 caused by the incoherent scattering cannot be obtained simply adding the amorphous contribution.

We repeated the measurements for CR and radiation accompanying VR with a smaller collimator aperture (4 mm instead of 40 mm) to reject the contribution of the soft radiation emitted at large angles. The spectrum measured in this configuration presents a sharper peak with respect to the higher collimator aperture (See, for a comparison, the inset of Fig. 3.7(a)). Both CR and VR radiation peak at $\sim$ 2 MeV, differently from the misaligned case in which the spectrum does not show any peak.

The radiation accompanying VR is comparable in intensity to the radiation in

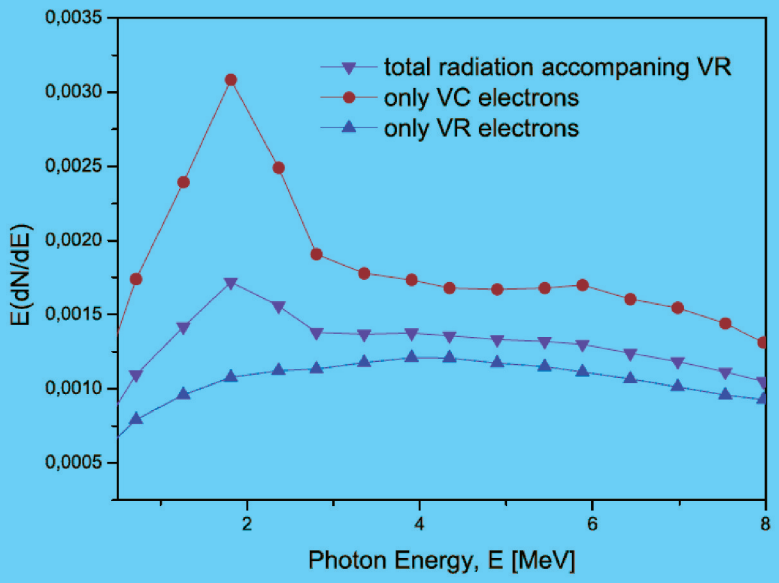

Figure 3.9: The simulated spectral intensity E(dN/dE) vs. photon energy E for the radiation accompanying VR (down triangles) and for the contribution of the 32% of VC particles (circles) and of the 68% of VR particles (up triangles). All the simulated spectral intensities are normalized to one electron trajectory. Adapted from Ref. [71]

a straight crystal, i.e., it is a sort of intermediate case between CR and CB, while it exhibits a higher flexibility in its usage as it was shown for the higher energies [126, 137]. First of all, since VR possesses an adjustable and broader angular acceptance, this effect can be used to obtain high-intensity radiation from beams with poor emittance. Secondly, being VR less sensitive to crystalline defects as compared to channeling [141], emitted radiation is not much degraded as well. This may lead to the usage of higher-Z materials such as W, which are expected to be more suitable for intense e.m. generation [141, 142] even if they cannot be grown with the same perfection as a Si crystal. Moreover, we also shown that the monochromaticity of emitted radiation can be improved with a suitable collimation system. This could make this kind of radiation a reliable alternative for a class of applications in nuclear physics and medicine, for which a nearly monochromatic MeV photon beam is needed.

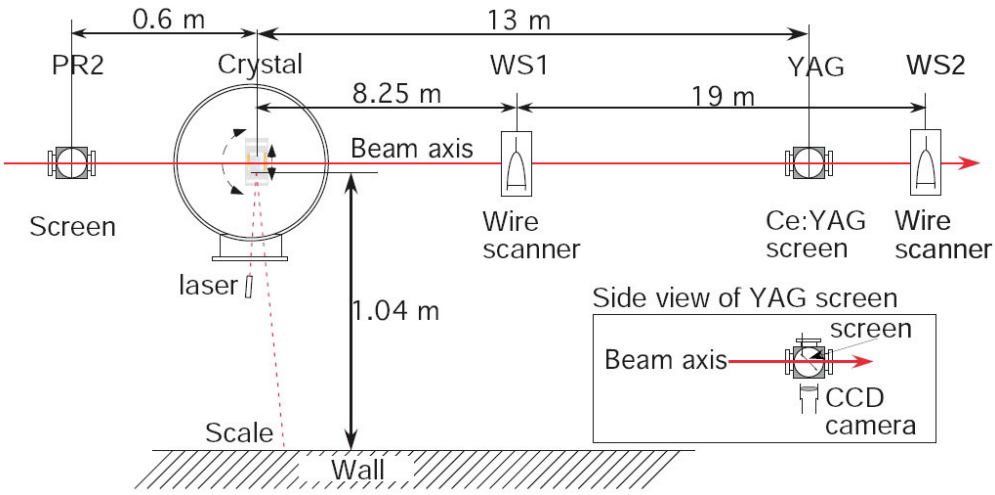

Figure 3.10: The experimental setup at the End Station A Test Beam at SLAC.. Adapted from Ref. [131].

3.2 Experiment with GeV-electrons at SLAC

3.2.1 Experimental setup at the ESTB of SLAC

The T-513 experiment is located at the End Station A (ESA) - End Station Test Beam (ESTB), which is in turn placed at the end of the SLAC LINAC. It provides the full range of electron energies up to 15.0 GeV with an intensity going from a single particle to 109 particles per bunch. The width of the beam available at the ESTB of SLAC is less than 150 μm both in the vertical and horizontal directions while the beam divergence is less than 10 μrad, much lower than the 54 μrad planar critical angle for channeling between (111) silicon planes at 15 GeV beam energy. This makes ESTB an optimal facility for the study of channeling and all the related phenomena.

The crystals are mounted in a scattering chamber in the End Station A Test Beam. The available experimental setup allows the angular alignment of the crystal for channeling and the detection of the manipulated beam [143]. A Newport AG-PR100 precision rotational stage allows the rotation of the crystal with step sizes nominally down to 5 μrad. A Newport AG-M25-27 translational stage allows the motion of the crystal into the beam as well to select the position where the beam impinges on the crystal itself. Deflected particles by means of coherent effects are currently detected with a YAG Screen and a camera placed 13 m downstream of the crystal. The detector provides the main diagnostics by monitoring the effect of the crystal on the beam. The YAG screen camera has a resolution of about 28 pixels/mm in the horizontal direction and 20 pixels/mm in the vertical one.

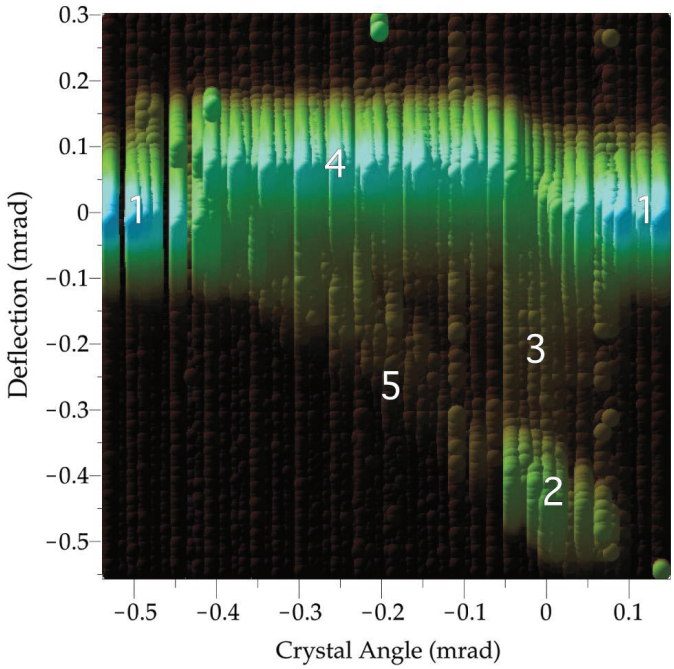

Figure 3.11: Deflection plot at 6.3 GeV beam energy. Colors correspond to log(intensity). The numbers denote the orientation of the crystal. 1: amorphous. 2: channeling. 3: dechanneling. 4: volume reflection. 5: volume capture. Adapted from Ref. [72].

3.2.2 Coherent interactions of 3.35 - 14.0 GeV Electrons in a bent Silicon Crystal

In this section I will show the results obtained in the T-513 experiment, in which I was involved for the fabrication and characterization of the bent crystal used. These results are already published in Refs. [72, 131].

The silicon (Si) crystal used in this experiment was fabricated as explained in Sec. 2.4 and Ref. [69] with crystallographic orientation chosen to produce quasi-mosaic bending of the (111) plane [61]. Its thickness was measured interferometrically to be 60 $\pm$ 1 μm. The (111) plane has a bending radius of 149 mm giving a total bending angle of the crystal of $\theta_b = 402 \pm 9$ μrad in the horizontal direction. Crystal is depicted in Fig. 2.35(a). Results of the characterization are shown in Figs. 2.38 and 2.40.

The experimental measurements were performed by rotating the crystal in small angular steps and recording an image of the circular YAG screen. The crystal deflects particles in the horizontal plane. The intensity is summed in the vertical plane, and the probability distribution is normalized as shown in Fig.

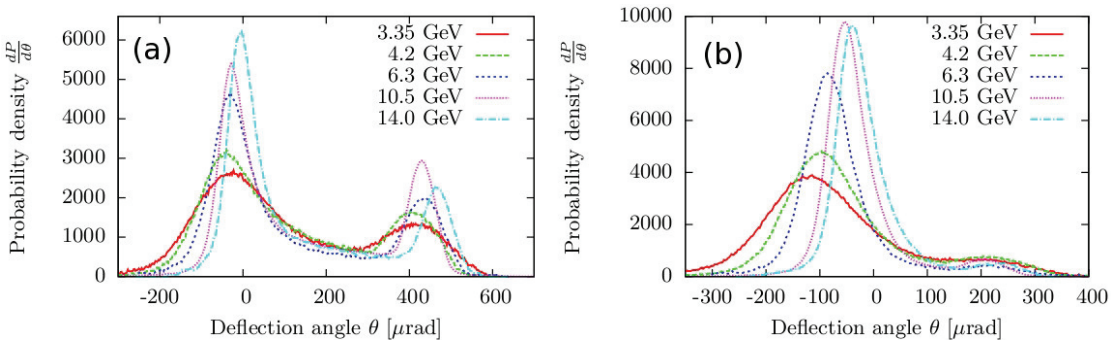

Figure 3.12: The probability density of the deflected particles when the crystal is in the channeling orientation (a), and when the crystal is at half of the full bending angle (b) for the different energies in the experiment. In (b) the large leftmost peaks are the volume reflected portions and the small rightmost peaks are the volume captured particles. Adapted from Ref. [131].

3.12a. For each crystal angle several images were taken. The distribution along the y-axis with the crystal angle along the x-axis gives the deflection plot, of which an example is shown in Fig. 3.11. One can clearly distinguish a pattern similar to the one obtained at MAMI with sub-GeV electrons (see Sec. 3.1.2). A crystal angle of 0 was chosen to be the orientation of closest direct entry of the beam into the channel as could be experimentally realized. The orientation chosen for volume reflection studies corresponds to the middle of the angular acceptance region, which is approximatively equal to the channeling deflection angle.

Channeling and volume reflection were investigated at 5 energies: 3.35, 4.2, 6.3, 10.5 and 14.0 GeV. For the cases reported in Ref. [72], i.e. 3.35 and 6.3 GeV, deflections of the beam was at 400 μrad for both energies, thus confirming the bending angle which was predicted with the characterization performed at SSL. Deflection efficiency in channeling mode was of about 22% for both energies. In the volume-reflection orientation, deflection of the beam was by 120 μrad at 3.35 GeV and by 80 μrad at 6.3 GeV, with an efficiency of 86% and 95% respectively. In Fig. 3.12 the probability density of the deflected particles is plotted for channeling and VR respectively. In channeling plots shown in Fig. 3.12(a), some general tendencies can be identified. In particular, the width of the large leftmost peak, becomes narrower as does the channeled peak due to the decreasing critical angle. In 3.12(b) the large leftmost peak due to volume reflection moves closer to the undeflected position and the width decreases as energy increases.

A simple model was used for the fitting procedure: channeled particles are assumed to be distributed according to a Gaussian distribution within the channel, while the dechanneling process may occour with constant probability, leading to an exponential decay of channeled particles. Based on the parameters of fitting func-

tions, some important parameters describing the channeling process such as the dechanneling length, the angle of volume reflection, the surface transmission and the widths of the distribution of channeled particles parallel and orthogonal to the plane, were extracted. The scattering parallel to the plane fits well with the usual functional dependence of multiple scattering [144] on energy but is larger than amorphous/random by a factor of 1.7. For the distribution of channeled particles, the mean of the angle of volume reflection and the efficiency of volume capture, were fit to power functions with a free exponent and to a exponent fixed by that predicted by 'simple' theory, i.e. $1/\sqrt{E}$ scaling for VR deflection angle and $E^{-3/2}$ for VC efficiency. In these cases, a significant deviation is seen in the exponent which indicates that the 'simple' theory may be too simple to describe the results of this experiment. The 'simple' formula for surface transmission [131], however, works out well. The dechanneling lengths observed in these experiments are significantly shorter than predicted by the 'simple' theory [145] and the dechanneling length in 'VR orientation' is seen to be consistently smaller than in 'channeling orientation. However, in the DYNECHARM simulation [138], good agreement is seen in the angular distributions of the exiting particles and the obtained dechanneling lengths.

Chapter 4

Applications of bent crystals with ultra-relativistic ions at CERN

Investigation of coherent interactions at high energies is of special interest in view of application in accelerator physics, where such phenomena can be exploited for beam manipulation through the usage of bent crystals, for either beam collimation or extraction.

In a hadron collider, such as the Large Hadron Collider (LHC), a multi-stage collimation system is used to absorb the beam halo particles preventing quenches of its superconducting magnets and reducing the background at the experiments [146]. Halo generation is a rather complex process, resulting in a diffusive growth of the oscillation amplitudes of the particles at the edge of the beam core. The increase in amplitude per turn of halo particles is in general very small (considerably smaller than 1 μm). A primary collimator is a solid-state target, which scatters halo particles due to Coulomb scattering. Then, impact parameters are increased with a massive secondary collimator-absorber located downstream the primary collimator. However, a significant probability exists for these protons to be back scattered in the vacuum pipe and produce losses in the sensitive areas of the accelerator. Tertiary collimators are used to absorb these protons. In principle, scattering of protons from the absorber back to the accelerator with stray trajectories should be strongly reduced if a bent crystal has been used as a primary collimator. The crystal indeed should deflect particles in channeling states and direct them onto the absorber far from its edge (see Fig. 4.1b). This property could also be used to keep the secondary collimators at larger amplitudes, therefore minimizing their beam coupling impedance. Experiments on the beam halo collimation with short bent crystals have been firstly performed at the U-70 [94], RHIC [147] and Tevatron [148]. In the last case, the background in the CDF experiment was reduced by using the crystal as a primary collimator by a factor of two with respect to what was obtained in the same conditions with a tungsten

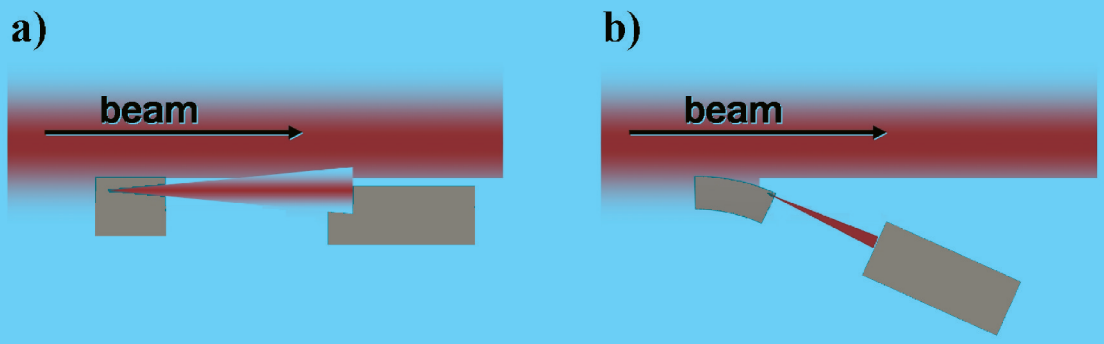

Figure 4.1: a) Traditional multi-stage collimation system: an amorphous target spreads the primary halo (creating the secondary halo) so that most of it can be intercepted by a more distant, with respect to the beam, secondary collimator; note that a real collimation system can present further collimation stages as well as shields to protect the equipment from the escaping particles. b) Crystal based collimation: a bent crystal acts as a smart primary collimator deviating (through channeling) the beam halo into the absorber [150].

primary collimator. The promising results achieved in the last years of tests of crystal-assisted collimation in the CERN Super Proton Synchrotron (SPS), in the framework of the UA9 Collaboration [3, 29, 76, 149], demonstrated the principle feasibility of such technology for the collimation of the LHC beam. Before relying on this system for the much more complex and challenging LHC upgrade, first experimental tests were very recently performed with LHC beams [4].

Particle extraction is another important process in circular accelerators, since it allows to produce high energy beams that can be used in fixed target experiments, or to test the instrumentation. The classical slow extraction method consists of a system of electrostatic and magnetic septa, which provide steering of particles towards the external beamline. A bent crystal can be used in particle extraction as a compact and passive septum characterized by a strong electric field (of the order of 10^9 - 10^{11} Vm) with a very small entrance wall that, ideally, can be just a single atomic layer. The scheme of the crystal assisted extraction is similar to the crystal collimation one: a crystal intercepts the beam halo deviating it from the circular trajectory but, differently from collimation, the extracted beam is not lost in an absorber but sent to bending magnets that bring it to the experimental areas. Depending on the required extracted beam intensity, crystal extraction can work in a "parasitic" mode, exploiting the "natural" beam halo, or in an "active" one, in which the beam halo is stimulated to increase its intensity. Crystal extraction presents several benefits with respect to the classic extraction method [94], for instance it can work in parasitic mode allowing at the same time the operation of a collider and the production of an extracted beam, it gives an extracted beam

with a time structure almost flat since the extraction mechanism does not use a resonant method, the extracted beam has a small size and a regular shape, and the polarization of the main beam is preserved during the extraction. Bent crystals were already used for beam extraction at JINR [5], IHEP [56], CERN SPS [57] and Tevatron [121]. The SPS and Tevatron tests gave an important contribution demonstrating that the extraction efficiency can increase a lot exploiting the so called multi-turn effect: being in a circular accelerator, a particle can impinge on the crystal more than once increasing the resulting channeling probability. The experimental proof of this phenomenon, already predicted in [151], led to the development of shorter crystals in order to enhance efficiency: the shorter the crystal, the lower the intensity of multiple scattering for the particles crossing it in the "amorphous" condition, so that these particles are not expelled from the nominal beam and have a second chance to be channeled. In last years, a short silicon crystal made possible to reach an extraction efficiency of about 90% with 50 GeV/c protons at U70 [152]. In the framework of the CRYSBEAM european project, beam extraction in channeling mode was recently proposed for the LHC at the nominal energy, and the Ferrara group is currently involved in this project.

Strip crystals optimized for the collimation in LHC and first prototype for extraction were fabricated and characterized at SSL as shown in Sec. 2, then, they were characterized at the extracted lines H8-SPS. On the falling of 2015, crystals for the collimation in the LHC were tested at the entry energy 450 GeV and at the nominal energy 7 TeV with protons, and with 450 GeV lead ions.

In this chapter, results of characterization of the latest strips for collimation and extraction at H8-SPS are shown and compared to the results of precharacterization at SSL. Moreover, preliminary result indicating the first evidence of channeling at the LHC were shown.

4.1 Crystal characterization at the H8 external line of SPS

4.1.1 Experimental setup

The study of channeling phenomena requires very accurate angular alignment of the silicon crystals with respect to the beam. Indeed, the critical angle for channeling is of the order of 10 μrad for 400 GeV/c protons. A charged particle telescope has been constructed by the Imperial College London group for the data taking at high rates in a CERN 400 GeV/c proton beam line. A full description of the system can be found in Ref. [153].

The objective of the system is to provide excellent angular and spatial resolution for measuring the trajectories of incident and outgoing particles. The system

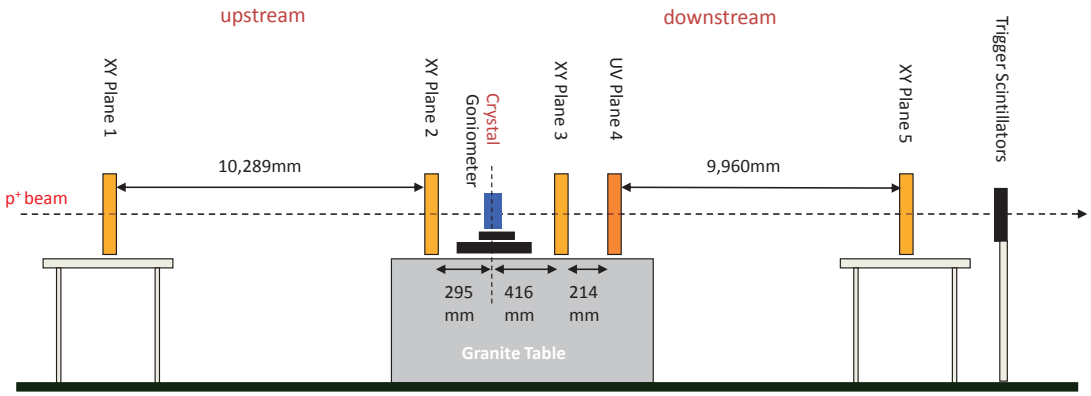

Figure 4.2: Experimental layout in the H8 beam line [153]. The UV plane denotes the rotated (45°) XY plane.

utilizes ten planes of Si microstrip sensors, arranged as five pairs each measuring two orthogonal coordinates, with an active area of 3.8×3.8 cm^2. The apparatus has a long baseline, approximately 10 m in each arm, and achieves an angular resolution in the incoming arm of 2.8 μrad and a total angular resolution on the difference of the two arms of 5.2 μrad, with performance limited by multiple scattering in the sensor layers. The Si microstrip telescope was tested in the CERN H8 beam line in September 2010. The layout of the telescope is described in Fig. 4.2.

The upstream section of the telescope for the measurement of incoming tracks is formed by planes 1 and 2 while outgoing tracks are measured using planes 3, 4 and 5. Plane 4 is a rotated XY plane (45°), used in order to resolve ambiguities in reconstruction from multiple outgoing tracks. Events were triggered on the signal coincidence recorded by a pair of plastic scintillators placed downstream the telescope. In the following I will show the results of the on beam characterization of the crystals which were presented in Sec. 2.3.

4.1.2 Strip crystals for the collimation in LHC

Several strip crystals were fabricated to be tested for the collimation of the LHC. First prototypes, i.e. the twin crystals STF75 and STF76, were fabricated and pre-characterized at SSL within the beginning of 2014, in time for mounting during the dedicated opening of LHC pipe on April 2014 during the "Long Shutdown 1" of LHC. In particular, one of the two crystal (STF75) was mounted in LHC directly after precharacterization at SSL. Only few months later it was possible to characterize the spare crystal (STF76) with high energy ion beams since activity of the SPS and its external lines restarted in late 2014. Then, in 2015, new silicon strips were fabricated and mounted onto a second generation of titanium holders (STF105 and STF106), which represent the actual state-of-the art technology for LHC collimation.

For online characterization with 400 GeV/c protons at the H8 beam line, crystals were mounted on a high resolution goniometer, and aligned to the beam in order to excite channeling. Tracking of protons trajectories before and after interaction with the crystal is performed by means of a silicon telescope [153], allowing to determine bending angle, crystal torsion and steering efficiency. Figure 4.3 shows the angular profile of deflected particles as the crystal is oriented to the beam in order to excite channeling for the STF105- and STF106- crystals respectively. Bending angle resulted to be equal respectively to 49 ± 1 μrad and 41.5 ± 1.5 μrad, while torsion is evaluated to be less than 2 μrad/mm for both crystals. This results are in agrement with those obtained in the pre-characterization at SSL, and reported in Table 2.3. As protons impinging on the crystal within an angular range of ± 2 μrad are selected a channeling steering efficiency of $(80 \pm 1)\%$ and $(81 \pm 2)\%$ for STF105 and STF106 respectively, being in agreement with the one expected for a crystal free of defects detrimental for channeling efficiency [27].

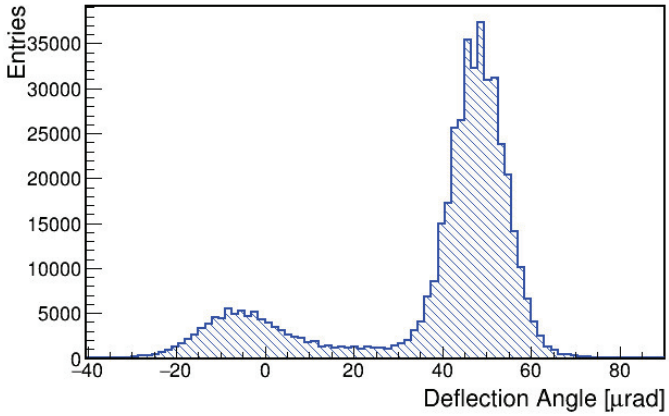

(a)

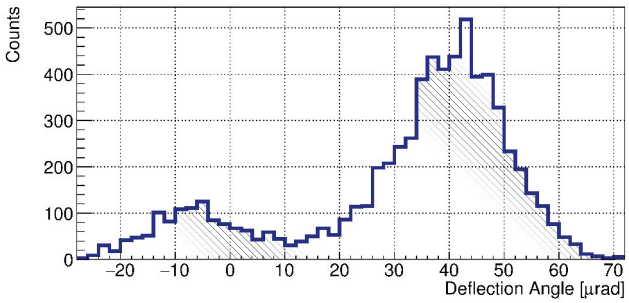

(b)

Figure 4.3: Angular distribution of 400 GeV protons after interaction with STF105 (a, courtesy of L. Bandiera) and STF106 (b, courtesy of E. Bagli) crystal as it is aligned to the beam in order to excite channeling. Only particle impinging within an angle of ± 2 μrad with respect to atomic planes are selected.

4.1.3 Strip crystals for extraction in LHC

A first campaign of measurements to test the quality and to evaluate the deflecting capability of the two realized samples (PL01 and PL02) were performed on the H8 extracted beamline from SPS at CERN in April/May 2015 and in June 2015 with a primary 400 GeV/c proton beam. This is the maximum proton beam energy available on a beam-test line, therefore being the most suitable for investigating the possibility of beam extraction at TeV energies.

For the PL02 crystal, a torsion of (12 ± 2) μrad/mm was evaluated with off-line analysis, being in agreement with the interferometric characterization. Fig. 4.4 displays the experimental deflected distribution of the beam in the horizontal direction in the case of perfect alignment with the (110) bent planes, obtained after a torsion compensation procedure. The peak on the left represents the over barrier particles that were not channeled during their motion inside the crystal, while the highest peak on the right corresponds to the channeled protons that were deflected at an angle equal to (281 ± 10) μrad. The region between the two peaks is populated by the particles that were dechanneled during their passage through the crystal. The deflection efficiency of the PL02 sample was found to be about 68%. A preliminary analysis of the angular scan of the PL01 crystal (see Fig. 4.5) allowed to estimate a bending angle of (290 ± 20) μrad. Results obtained for both crystals are in good agreement with precharacterization shown in Table 2.4.

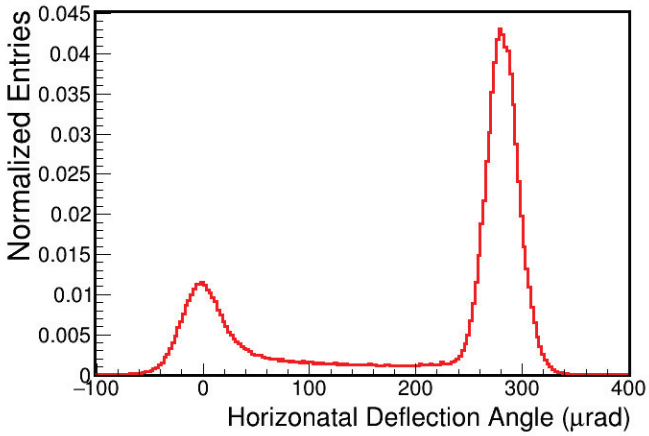

Figure 4.4: Deflected distribution of the 400 GeV/c proton beam after interaction with the PL02 crystal sample, in condition of perfect alignment with the bent (110) crystal planes. Courtesy of L. Bandiera.

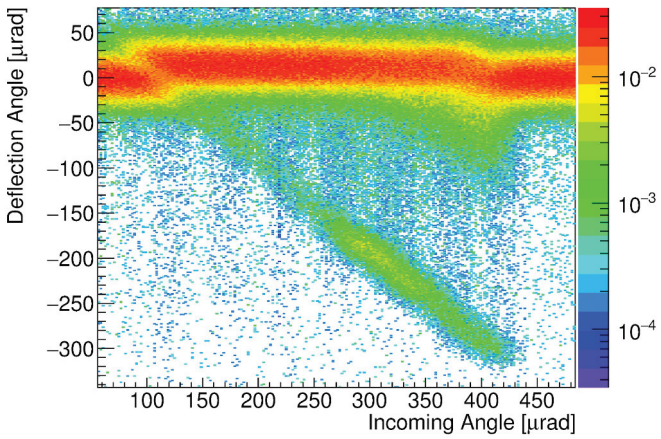

Figure 4.5: Deflected distribution vs. crystal-to-beam orientation of the 400 GeV/c proton beam after interaction with the PL01 crystal sample. Courtesy of E. Bagli.

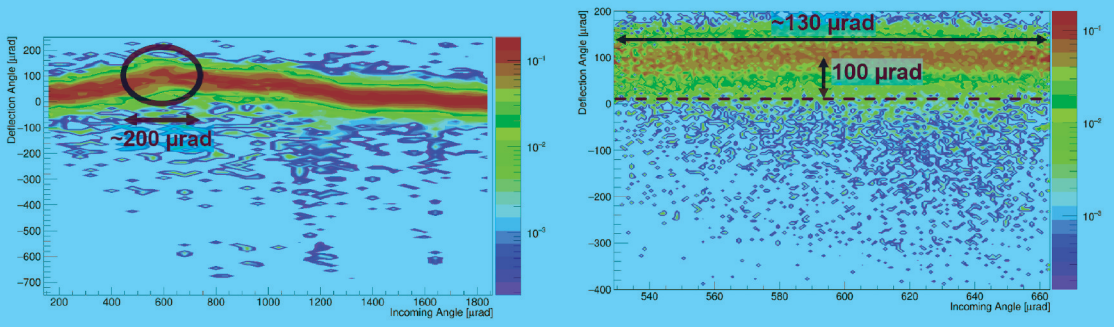

(a) (b)

Figure 4.6: Deflected distribution vs. crystal-to-beam orientation of the 180 GeV/c pion beam after interaction with the MSTF13 crystal sample: fast angular scan to identify the region of interest (a), and refined scan (b). Multiple volume reflection provides a deflection of ∼100 μrad in an angular acceptance of ∼130 μrad. Courtesy of E. Bagli.

4.1.4 Multistrip crystal for collimation in SPS

The multistrip crystal MSTF-13, which has been fabricated and pre-characterized at SSL as described in Chapter 2, was characterized on December 2014 at the external line H8 with pions of energy 180 GeV. A fast angular scan allowed to identify a region where multiple volume reflection (MVR) occours, as shown in Fig. 4.6(a). A refined scan in the region of interest highlights that MVR does not overlap with channeling region. From this scan, we estimated an angular acceptance for MVR equal to 130 μrad, which is in good agreement with the value of 125 μrad found within the precharacterization (see Sec. 2.3.3). By analyzing data recorded at a fixed position in the MVR region (see Fig. 4.7), we estimated a deflection angle of 100 μrad. Being the deflection angle for VR of about ∼16 μrad for 180 GeV pions, we confirmed that 7 strips are aligned to excite MVR. The total deflection efficiency of MVR was found to be ∼90%. After this succesful test, MSTF13 was installed in the SPS, in view of testing for the collimation.

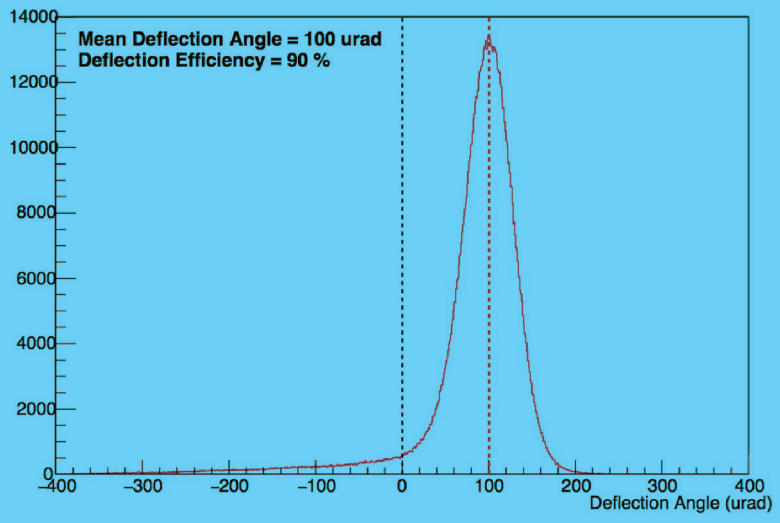

Figure 4.7: Deflected distribution vs. crystal-to-beam orientation of the 180 GeV/c proton beam after interaction with the PL01 crystal sample. Courtesy of E. Bagli.

4.2 Preliminary results of crystal assisted collimation at the LHC

Two crystals have been installed respectively in the horizontal and vertical planes of the LHC Beam 1, in the betatron collimation insertion (IR7), during the Long Shutdown 1 of the LHC in April 2014. Among them, the crystal installed on the horizontal plane is the strip crystal STF75 manufactured at SSL Ferrara, while the crystal installed in the vertical plane is a quasi-mosaic crystal produced by the PNPI institute. The main constrain considered for designing a dedicated layout was to have a minimum impact on the present collimation layout and infrastructure with a safe strategy to absorb the channeled and extracted halo [154]. The final layout, which is shown in Fig. 4.8, relies on the installation of two new devices only, i.e. two goniometers for horizontal and vertical crystals, and on the use of existing secondary collimators (TCSG) to intercept the channeled beams. The horizontal layout consists of a goniometer slot TECGH.4L7.B1 at s = 19919.24 m from IP1, and the TCSG.B4L7.B1 and TCSG.6R7.B1 used as absorbers at any energy and only at top energy, respectively. The vertical one consists of a goniometer slot TECGV.6L7.B1 at s = 19843.82 m from IP1, and the TCSG.D4L7.B1 as absorber at any energy. The three horizontal and two vertical massive absorbers 2 (TCLA) at the end of the collimation chain will be always in place. The LHC Beam Loss Monitoring (BLM) system features one ionization chamber at each collimator and several ones at each lattice magnet, in particular at the critical loss locations

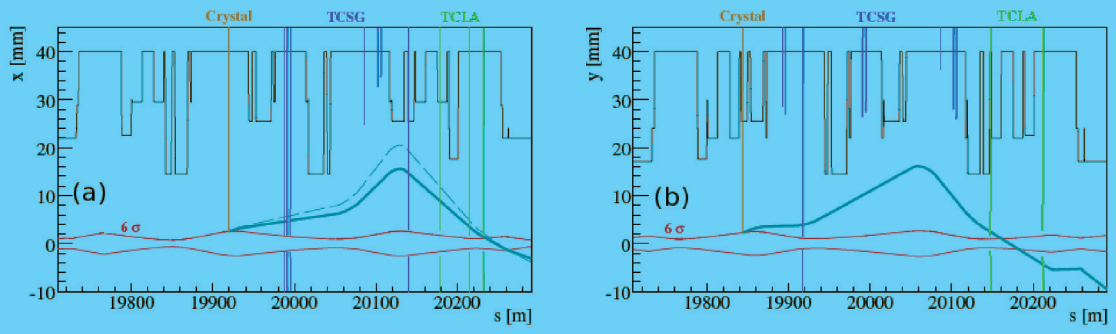

Figure 4.8: Horizontal (a) and vertical (b) layout for crystal-assisted collimation in the LHC-IR7 Beam 1, at 7 TeV. Orange line: crystal aperture (6 σ), blue lines: projection on the plane of interest of the secondary aperture (7 σ for selected TCSG, retracted otherwise) , green lines: projection on the plane of interest of the absorbers aperture (10 σ). The solid gray line is the trajectory followed by the channeled halo particles, i.e. a kick of 50 μrad is acquired, while the dashed one shows the maximum kick allowed if the configuaration (1) is used, i.e. 65 μrad. Adapted from Ref. [155].

in the IR7 Dispersion Suppressor 3 (DS). The BLM system was used for the first measurements of crystal-assisted collimation efficiency. Additional diamond BLMs are also installed to enable 2 ns acquisitions of losses at the crystals. Moreover, space reservations for future system upgrades are made, such as the installation of Cherenkov detectors in primary LHC vacuum, useful to characterize the extracted halo. More details on the setup are available in [155] and references therein.

Three Machine Development (MD) sections aimed to testing crystal-assisted collimation capatibilies were performed in 2015:

- 30/08 - both crystals were tested at injection energy (450 GeV) with protons
- 06/11 - horizontal crystal was tested at flat top (6.5 TeV) with protons
- 02/12 - both crystals tested at injection energy (450 GeV) with Pb ion beam

Operations consisted in aligning the crystal as a primary collimator, followed by a fast angular scan to find channeling position. Then, a fine angular scan is performed at different goniometer speeds. Channeled beam scan is performed with TCSG used as absorber entering in the beam with the crystal in channeling orientation. Finally, beam loss is acquired with the BLM. These initial tests were performed at reduced beam intensity, and were extremely successful, since they resulted in the first observation of channeling at the 6.5 TeV record energy, being also the first observation of channeling of the beam circulating in the LHC. The test with 450 GeV Pb ions led to the observation of channeling at record energy with heavy ions. Higher intensity tests are being prepared to clarify if bent crystals could improve the baseline LHC collimation as a further step towards the collimation upgrade in the High-Luminosity LHC project [4].

Conclusions

This thesis showed the actual state of the art in manufacturing and characterization of silicon bent crystals fabricated at the Sensor and Semiconductor Laboratory (SSL) of Ferrara for experimental studies of coherent interactions of charged particles into bent crystals.

Strip crystals exploiting anticlastic curvature, and plates exploiting the quasi mosaic effect were produced by means of techniques developed in the last decade at SSL, such as photolitography, wet etching, and mechanical dicing. Those techniques were recently enhanced by introducing further treatments, such as Magnetorheological Finishing, which allowed to fabricate crystals with ultraflat surface and miscut very close to zero, and the usage of silicon-on-insulator wafers, which permitted to fabricate crystals with a thickness down to 15 μmm.

The technology of the mechanical devices used to hold and bend crystals has been also improved. New materials were employed to realize the holders, for instance titanium, due to compatibility constraint with the ultra-high vacuum of the LHC pipe. Moreover, the clamping system and the mechanism to reduce torsion via screws were optimized.

Characterization method were also improved. The long-term used white light interferometry for surface characterization was supported by a high resolution X-rays diffractometer. The diffractometer was also used to directly measure principal bending, anticlastic bending and torsion, thanks to purposely designed mechanical supports for mounting bent crystals onto the cradle. Accuracy of the diffractometer was furtherly enhanced with a custom made autocollimator, which found an important application in miscut characterization after MRF reduction. A new infrared light interferometer was used to map the thickness of the starting wafers with nanometric precision, as well as to measure the length along the beam of the strips.

Several bent crystals were produced. For high energy applications, we realized few strip crystals for the collimation of the LHC beam, two long strip crystals for the development of a crystalline extractor for the LHC, a multistrip crystals for the collimation of the SPS beam. For low energy applications of negative particles, where comparatively thinner crystals are required, few quasi-mosaic crystals with

various thickness in the tens-μm range were fabricated and mounted onto fixed-radius bnding holders, and a 15 μm-thick plates were mounted onto a new remoted-controlled bending device developed by LNL.

Quasi-mosaic crystals were used to obtain efficient steering and to study accompanying radiation emission of sub-GeV electrons in a bent crystal at MAMI, and deflection of GeV electrons at SLAC. Crystals for high-energy application were characterized at the H8 external lines of CERN-SPS with various hundreds-GeV ion beams, which gave results in agreement with the precharacterization performed at SSL. Among these last crystals, the multistrip was installed in the SPS in view of testing it for collimation, and one strip crystal was selected to be installed in the LHC beam pipe during the Long Shutdown 1 in 2014. This crystal was very recently tested for a crystal-assisted collimation experiment with a 6.5 TeV proton beam, resulting in the first observation of channeling at this record energy, being also the first observation of channeling of the beam circulating in the LHC.

Bibliography

[1] O. S. Bruning, P. Collier, P. Lebrun, S. Myers, R. Ostojic, J. Poole, and P. Proudlock, *LHC Design Report* (CERN, Geneva, 2004), .

[2] V. Biryukov, Y. Chesnokov, and V. Kotov, *Crystal Channeling and Its Application at High-Energy Accelerators*, Accelerator Physics (Springer, 1997), ISBN 9783540607694, .

[3] W. Scandale, G. Arduini, M. Butcher, F. Cerutti, S. Gilardoni, L. Lari, A. Lechner, R. Losito, A. Masi, A. Mereghetti, et al., Phys. Lett. B **726**, 182 (2013).

[4] *CERN Bulletin Issue No. 49-50/2015. 49-50/2015* (2015), .

[5] V. Avdeichikov, V. Buldakovsky, A. Bychkov, A. Vodopianov, J. Wojtkowska, et al. (1986).

[6] G. Cavoto, *Beam Extraction with Crystal at CERN, the CRYSBEAM Project* (2014), .

[7] M. Kumakhov, Phys. Lett. A **57**, 17 (1976).

[8] D. Lohmann, J. Peise, J. Ahrens, I. Anthony, H.-J. Arends, R. Beck, R. Crawford, A. Hünger, K. Kaiser, J. Kellie, et al., Nucl. Instrum. Methods Phys. Res. A **343**, 494 (1994).

[9] J. Stark, Phys. Zs. **13**, 973 (1912).

[10] M. T. Robinson and O. S. Oen, Phys. Rev. **132**, 2385 (1963).

[11] G. R. Piercy et al., Phys. Rev. Lett. **10**, 399 (1963).

[12] J. Lindhard, *Influence of crystal lattice on motion of energetic charged particles*, Det Kongelige Danske Videnskabernes Selskab. Matematisk-fysiske meddelelser. 34, 14 (Ejnar Munksgaard, 1965), .

[13] E. Tsyganov, Tech. Rep., Fermilab (1976), preprint TM-682.

[14] A. F. Elishev *et al.*, Phys. Lett. B **88**, 387 (1979).

[15] V.A. Andreev *et al.*, Pis'ma v Zh. Eksp. Teor. Fiz. **36**, 340 (1982).

[16] V.A. Andreev *et al.*, Pis'ma v Zh. Eksp. Teor. Fiz. **38**, 58 (1984).

[17] V.A. Andreev *et al.*, Pis'ma v Zh. Eksp. Teor. Fiz. **44**, 101 (1986).

[18] A. Taratin and S. Vorobiev, Physics Letters A **119**, 425 (1987), ISSN 0375-9601, .

[19] Y. M. Ivanov, A. A. Petrunin, V. V. Skorobogatov, Y. A. Gavrikov, A. V. Gelamkov, L. P. Lapina, A. I. Schetkovsky, S. A. Vavilov, V. I. Baranov, Y. A. Chesnokov, et al., Phys. Rev. Lett. **97**, 144801 (2006), .

[20] S. Hasan, Master's thesis, University of Insubria (2007).

[21] G. Moliére, Z. Naturforsch. A **2**, 133 (1947).

[22] E. Bagli, V. Guidi, V. A. Maisheev, Phys. Rev. E **81**, 026708 (2010).

[23] R. J. Carrigan and J. Ellison, *Relativistic Channeling* (Plenum Press, 1987).

[24] G. Arduini *et al.*, Phys. Lett. B **422**, 325 (1998), ISSN 0370-2693, .

[25] J. Bak *et al.*, Nucl. Phys. B **254**, 491 (1985), ISSN 0550-3213.

[26] W.M. Gibson *et al.*, Nucl. Instrum. Methods Phys. Res., Sect. B **2**, 54 (1984), ISSN 0168-583X.

[27] W. Scandale *et al.*, Phys. Lett. B **680**, 129 (2009).

[28] W. Scandale *et al.*, Phys. Lett. B **688**, 284 (2010).

[29] W. Scandale *et al.*, Phys. Lett. B **692**, 78 (2010).

[30] W. Scandale *et al.*, Journal of Instrumentation **6**, T10002 (2011).

[31] W. Scandale, et al., Phys. Rev. A **79**, 012903 (2009).

[32] W. Scandale *et al.*, Phys. Lett. B **701**, 180 (2011), ISSN 0370-2693, .

[33] V. Baryshevsky, I. Dubovskaya, and A. Grubich, Physics Letters A **77**, 61 (1980), ISSN 0375-9601, .

[34] V. Kaplin, S. Plotnikov, and S. Vorobiev, Zh. Tekh. Fiz. **50**, 1079 (1980).

[35] M. Tabrizi, A. V. Korol, A. V. Solov'yov, and W. Greiner, Phys. Rev. Lett. **98**, 164801 (2007), .

[36] X. Artru *et al.*, Phys. Rev. ST Accel. Beams **6**, 091003 (2003).

[37] M. Satoh *et al.*, Nucl. Instrum. Methods Phys. Res., Sect. B **227**, 3 (2005), radiation from Relativistic Electrons in Periodic Structures (RREPS'03).

[38] R. A. J. Carrigan, International Journal of Modern Physics A **25S1**, 55 (2010).

[39] W. Scandale *et al.*, Phys. Lett. B **680**, 301 (2009).

[40] W. Scandale, A. Vomiero, E. Bagli, S. Baricordi, P. Dalpiaz, M. Fiorini, V. Guidi, A. Mazzolari, D. Vincenzi, R. Milan, et al., Physics Letters B **681**, 233 (2009), ISSN 0370-2693, .

[41] W. Scandale *et al.*, Phys. Lett. B **693**, 545 (2010).

[42] W. Scandale, R. Losito, E. Bagli, L. Bandiera, P. Dalpiaz, M. Fiorini, V. Guidi, A. Mazzolari, D. Vincenzi, G. D. Mea, et al., Physics Letters B **719**, 70 (2013), ISSN 0370-2693, .

[43] E. Bagli et al., The European Physical Journal C **74**, 1 (2014).

[44] E. Tsyganov, Tech. Rep., Fermilab (1976), preprint TM-684.

[45] Akhiezer A. I., Akhiezer I. A. and Shul'ga, N.F., Sov. Phys. Journal of Experimental and Theoretical Physics **49**, 631 (1979).

[46] Shul'ga, N.F., Journal of Experimental and Theoretical Physics Letters **32**, 166 (1980).

[47] A. I. Akhiezer and N. F. Shul'ga, Soviet Physics Uspekhi **25**, 541 (1982), .

[48] A. Taratin and S. Vorobiev, Nucl. Instrum. Methods Phys. Res., Sect. B **26**, 512 (1987), ISSN 0168-583X, .

[49] W. Scandale *et al.*, Phys. Rev. Lett. **98**, 154801 (2007), .

[50] Y. Chesnokov, N. Galyaev, V. Kotov, S. Tsarik, and V. Zapolsky, Nuclear Instruments and Methods in Physics Research Section B: Beam Interactions with Materials and Atoms **69**, 247 (1992), ISSN 0168-583X, .

[51] N. Shul'ga, V. Truten, V. Boyko, and A. Esaulov, Physics Letters A **376**, 2617 (2012), ISSN 0375-9601, .

[52] A. M. Taratin and S. A. Vorobiev, physica status solidi (b) **133**, 511 (1986), ISSN 1521-3951, .

[53] E. Bagli, Ph.D. thesis, Università degli Studi di Ferrara (2014).

[54] W. Scandale, A. Vomiero, S. Baricordi, P. Dalpiaz, M. Fiorini, V. Guidi,

A. Mazzolari, G. Della Mea, R. Milan, G. Ambrosi, et al., Phys. Rev. Lett. **102**, 084801 (2009), .

[55] E Bagli *et al.*, Journal of Instrumentation **7**, P04002 (2012), .

[56] A. Asseev, M. Bavizhev, E. Ludmirsky, V. Maisheev, and Y. Fedotov, Nuclear Instruments and Methods in Physics Research Section A: Accelerators, Spectrometers, Detectors and Associated Equipment **309**, 1 (1991), ISSN 0168-9002, .

[57] H. Akbari, X. Altuna, S. Bardin, R. Bellazzini, V. Biryukov, A. Brez, M. Bussa, L. Busso, A. Calcaterra, G. Carboni, et al., Physics Letters B **313**, 491 (1993), ISSN 0370-2693, .

[58] V. Baublis, I. Ivanov, I. Ivochkin, A. Khanzadeev, V. Kuryatkov, E. Lapin, N. Miftakhov, V. Morozov, S. Novikov, T. Prokofieva, et al., Nuclear Instruments and Methods in Physics Research Section B: Beam Interactions with Materials and Atoms **90**, 150 (1994), ISSN 0168-583X, .

[59] J. CZOCHRALSKI, Z. phys. Chemie. **92**, 219 (1918), .

[60] V. M. Biryukov, Y. A. Chesnokov, V. Guidi, V. I. Kotov, C. Malagù, G. Martinelli, W. Scandale, M. Stefancich, and D. Vincenzi, Review of Scientific Instruments **73** (2002).

[61] Y. Ivanov, A. Petrunin, and V. Skorobogatov, Journal of Experimental and Theoretical Physics Letters **81**, 99 (2005), ISSN 0021-3640, .

[62] V. Guidi, A. Antonini, S. Baricordi, F. Logallo, C. Malagù, E. Milan, A. Ronzoni, M. Stefancich, G. Martinelli, and A. Vomiero, Nuclear Instruments and Methods in Physics Research Section B: Beam Interactions with Materials and Atoms **234**, 40 (2005), ISSN 0168-583X, relativistic Channeling and Related Coherent Phenomena in Strong Fields, .

[63] S. Baricordi, V. M. Biryukov, A. Carnera, Y. A. Chesnokov, G. D. Mea, V. Guidi, Y. M. Ivanov, G. Martinelli, E. Milan, S. Restello, et al., Applied Physics Letters **87**, 094102 (2005), .

[64] S. Baricordi, V. Guidi, A. Mazzolari, G. Martinelli, A. Carnera, D. De Salvador, A. Sambo, G. Della Mea, R. Milan, A. Vomiero, et al., Applied Physics Letters **91**, 061908 (2007), .

[65] S. Baricordi, V. Guidi, A. Mazzolari, D. Vincenzi, and M. Ferroni, Journal of Physics D: Applied Physics **41**, 245501 (2008), .

[66] V. Guidi, A. Mazzolari, D. De Salvador, and L. Bacci, Phys. Rev. Lett. **108**, 014801 (2012), .

[67] A. Mazzolari, V. Guidi, D. D. Salvador, and L. Bacci, Nuclear Instruments and Methods in Physics Research Section B: Beam Interactions with Materials and Atoms **309**, 130 (2013), ISSN 0168-583X, the 5th International Conference Channeling 2012, Charged and Neutral Particles Channeling Phenomena, September 23-28,2012, Alghero (Sardinia), Italy, .

[68] W. Scandale, G. Arduini, M. Butcher, F. Cerutti, S. Gilardoni, A. Lechner, R. Losito, A. Masi, E. Metral, D. Mirarchi, et al., Physics Letters B **734**, 1 (2014), ISSN 0370-2693, .

[69] G. Germogli, A. Mazzolari, L. Bandiera, E. Bagli, and V. Guidi, Nuclear Instruments and Methods in Physics Research Section B: Beam Interactions with Materials and Atoms **355**, 81 (2015), ISSN 0168-583X, proceedings of the 6th International Conference "Channeling 2014: Charged and Neutral Particles Channeling Phenomena" October 5-10, 2014, Capri, Italy, .

[70] A. Mazzolari, E. Bagli, L. Bandiera, V. Guidi, H. Backe, W. Lauth, V. Tikhomirov, A. Berra, D. Lietti, M. Prest, et al., Phys. Rev. Lett. **112**, 135503 (2014), .

[71] L. Bandiera, E. Bagli, G. Germogli, V. Guidi, A. Mazzolari, H. Backe, W. Lauth, A. Berra, D. Lietti, M. Prest, et al., Phys. Rev. Lett. **115**, 025504 (2015), .

[72] U. Wienands, T. Markiewicz, J. Nelson, R. Noble, J. Turner, U. Uggerhøj, T. Wistisen, E. Bagli, L. Bandiera, G. Germogli, et al., Physical Review Letters **114**, 074801 (2015).

[73] A. Mazzolari, Pubblicazioni dello IUSS **3**, 1 (2009).

[74] V. Baublis, A. Khanzadeev, V. Kuryatkov, E. Lapin, N. Miftakhov, S. Novikov, T. Prokofieva, V. Samsonov, G. Solodov, B. Loginov, et al., Nuclear Instruments and Methods in Physics Research Section B: Beam Interactions with Materials and Atoms **119**, 308 (1996), ISSN 0168-583X, .

[75] K. Elsener, G. Fidecaro, M. Gyr, W. Herr, J. Klem, U. Mikkelsen, S. Møller, E. Uggerhøj, G. Vuagnin, and E. Weisse, Nuclear Instruments and Methods in Physics Research Section B: Beam Interactions with Materials and Atoms **119**, 215 (1996), ISSN 0168-583X, .

[76] W. Scandale, G. Arduini, R. Assmann, F. Cerutti, S. Gilardoni, E. Laface,

R. Losito, A. Masi, E. Metral, D. Mirarchi, et al., Physics Letters B **714**, 231 (2012), ISSN 0370-2693, .

[77] J. W. Gardner and V. K. Varadan, *Microsensors, Mems and Smart Devices* (2001).

[78] H. Seidel, L. Csepregi, A. Heuberger, and H. Baumgärtel, Journal of The Electrochemical Society **137**, 3612 (1990), , .

[79] K. Williams, K. Gupta, and M. Wasilik, Microelectromechanical Systems, Journal of **12**, 761 (2003), ISSN 1057-7157.

[80] W. Scandale, I. Efthymiopoulos, D. A. Still, A. Carnera, G. Della Mea, D. De Salvador, R. Milan, A. Vomiero, S. Baricordi, S. Chiozzi, et al., Review of Scientific Instruments **79**, 023303 (2008), .

[81] S. Timoshenko and . Goodier, J. N. (James Norman), *Theory of elasticity* (Auckland ; Singapore : McGraw-Hill, 1984), 3rd ed., ISBN 0070858055, originally published: New York, c1970.

[82] V. Guidi, L. Lanzoni, and A. Mazzolari, Journal of Applied Physics **107**, 113534 (2010), .

[83] J. J. Wortman and R. A. Evans, Journal of Applied Physics **36** (1965).

[84] S. Lekhnitskii, Grand Forks, BC, Mir (2011).

[85] G. Searle, *Experimental Elasticity* (Read Books, 2007), ISBN 9781406704440, .

[86] S. K. Kaldor and I. C. Noyan, Applied Physics Letters **80**, 2284 (2002).

[87] S. Kaldor and I. Noyan, Materials Science and Engineering: A **399**, 64 (2005), ISSN 0921-5093, measurement and Interpretation of Internal/Residual Stresses, .

[88] V. Carassiti, P. Dalpiaz, V. Guidi, A. Mazzolari, and M. Melchiorri, Review of Scientific Instruments **81**, 066106 (2010), .

[89] M. Schuster and H. Gobel, Journal of Physics D: Applied Physics **28**, A270 (1995), .

[90] V. Kupcik, R. Wulf, M. Wendschuh, A. Wolf, and A. Pähler, Nuclear Instruments and Methods in Physics Research **208**, 519 (1983), ISSN 0167-5087, .

[91] R. Camattari, L. Lanzoni, V. Bellucci, and V. Guidi, Journal of Applied Crystallography **48**, 943 (2015), .

[92] O. I. Sumbaev, Soviet Journal of Experimental and Theoretical Physics **5**, 1276 (1957).

[93] Lekhnitskii, *Anisotropic Plates [by] S.G. Lekhnitskii. Translated from the Second Russian Edition by S.W. Tsai and T. Cheron* (????).

[94] A. G. Afonin, V. T. Baranov, V. M. Biryukov, M. B. H. Breese, V. N. Chepegin, Y. A. Chesnokov, V. Guidi, Y. M. Ivanov, V. I. Kotov, G. Martinelli, et al., Phys. Rev. Lett. **87**, 094802 (2001), .

[95] Y. Ivanov, N. Bondar', Y. Gavrikov, A. Denisov, A. Zhelamkov, V. Ivochkin, S. Kos'yanenko, L. Lapina, A. Petrunin, V. Skorobogatov, et al., JETP Letters **84**, 372 (2006), ISSN 0021-3640, .

[96] H. Backe, P. Kunz, W. Lauth, and A. Rueda, Nuclear Instruments and Methods in Physics Research Section B: Beam Interactions with Materials and Atoms **266**, 3835 (2008), ISSN 0168-583X, radiation from Relativistic Electrons in Periodic Structures RREPS'07, .

[97] V. Guidi, A. Mazzolari, D. D. Salvador, and A. Carnera, Journal of Physics D: Applied Physics **42**, 182005 (2009), .

[98] G. Celler and S. Cristoloveanu, Journal of Applied Physics **93**, 4955 (2003).

[99] V. Lindroos, S. Franssila, M. Tilli, M. Paulasto-Krockel, A. Lehto, T. Motooka, and V. Airaksinen, *Handbook of Silicon Based MEMS Materials and Technologies*, Micro and Nano Technologies (Elsevier Science, 2009), ISBN 9780815519881, .

[100] R. Camattari, V. Guidi, V. Bellucci, and A. Mazzolari, Journal of Applied Crystallography **48**, 977 (2015), .

[101] D. Ashwell, Journal of Royal Aeronautical Society **54**, 708 (1950).

[102] S. Guiducci, in *Particle Accelerator Conference, 1999. Proceedings of the 1999* (1999), vol. 1, pp. 277–281 vol.1.

[103] A. Jankowiak, The European Physical Journal A - Hadrons and Nuclei **28**, 149 (2006), ISSN 1434-6001, .

[104] T. Iijima, Nuclear Instruments and Methods in Physics Research Section A: Accelerators, Spectrometers, Detectors and Associated Equipment **446**, 65 (2000), ISSN 0168-9002, .

[105] V. Kushnir, J. Quintana, and P. Georgopoulos, Nuclear Instruments and Methods in Physics Research Section A: Accelerators, Spectrometers, Detectors and Associated Equipment **328**, 588 (1993), ISSN 0168-9002, .

[106] J. Rogers, M. Lagally, and R. Nuzzo, Nature **477**, 45 (2011).

[107] H. C. Ko, M. P. Stoykovich, J. Song, V. Malyarchuk, W. M. Choi, C.-J. Yu, J. B. Geddes Iii, J. Xiao, S. Wang, Y. Huang, et al., Nature **454**, 748 (2008).

[108] E. Menard, R. G. Nuzzo, and J. A. Rogers, Applied Physics Letters **86**, 093507 (2005).

[109] H.-C. Yuan, J. Shin, G. Qin, L. Sun, P. Bhattacharya, M. G. Lagally, G. K. Celler, and Z. Ma, Applied Physics Letters **94**, 013102 (2009), .

[110] Y. Mei, D. Thurmer, F. Cavallo, S. Kiravittaya, and O. Schmidt, Advanced Materials **19**, 2124 (2007), ISSN 1521-4095, .

[111] H. Yang, H. Pang, Z. Qiang, Z. Ma, and W. Zhou, Electronics Letters **44**, 858 (2008), ISSN 0013-5194.

[112] M. A. Kumakhov, JETP Letters **45**, 781 (1977), .

[113] M. Ter-Mikaelian, *High-Energy Electromagnetic Processes in Condensed Media*, Interscience tracts on physics and astronomy (Wiley-Interscience, 1972), ISBN 9780471851905, .

[114] W. Heitler, *The quantum theory of radiation*, vol. 86 (Courier Corporation, 1954).

[115] E. Tsyganov and A. Taratin, Nuclear Instruments and Methods in Physics Research Section A: Accelerators, Spectrometers, Detectors and Associated Equipment **363**, 511 (1995), ISSN 0168-9002, .

[116] Y. Xu, R. Huang, and G. Rigby, Journal of Electronic Materials **21**, 373 (1992), ISSN 0361-5235, .

[117] B. Schwartz and H. Robbins, Journal of The Electrochemical Society **123**, 1903 (1976), , .

[118] D. F. Swinehart, Journal of Chemical Education **39**, 333 (1962), , .

[119] J. Baltazar-Rodrigues and C. Cusatis, Nuclear Instruments and Methods in Physics Research Section B: Beam Interactions with Materials and Atoms **179**, 325 (2001), ISSN 0168-583X, .

[120] D. Creagh, Nuclear Instruments and Methods in Physics Research Section A: Accelerators, Spectrometers, Detectors and Associated Equipment **255**, 1 (1987), ISSN 0168-9002, .

[121] R. A. Carrigan *et al.*, Phys. Rev. ST Accel. Beams **5**, 043501 (2002).

[122] Yu.N. Adishchev *et al.*, Phys. Lett. A **77**, 263 (1980), ISSN 0375-9601, .

[123] A. Baurichter *et al.*, Nucl. Instrum. Methods Phys. Res. B **119**, 143 (1996), ISSN 0168-583X, .

[124] Yu. A. Chesnokov et al., Journal of Instrumentation **3**, P02005 (2008).

[125] D. Lietti et al., Nucl. Instrum. Methods Phys. Res. B **283**, 84 (2012).

[126] L. Bandiera et al., Nucl. Instrum. Methods Phys. Res. B **309**, 135 (2013).

[127] L. Bandiera et al., Phys. Rev. Lett. **111**, 255502 (2013).

[128] A. Kostyuk, Phys. Rev. Lett. **110**, 115503 (2013), .

[129] E. Bagli, L. Bandiera, V. Bellucci, A. Berra, R. Camattari, D. De Salvador, G. Germogli, V. Guidi, L. Lanzoni, D. Lietti, et al., The European Physical Journal C **74**, 3114 (2014), ISSN 1434-6044, .

[130] D. Lietti, H. Backe, E. Bagli, L. Bandiera, A. Berra, S. Carturan, D. De Salvador, G. Germogli, V. Guidi, W. Lauth, et al., Review of Scientific Instruments **86**, 045102 (2015), .

[131] T. Wistisen, U. Uggerhoj, U. Aarhus, U. Wienands, T. Markiewicz, R. Noble, B. Benson, T. Smith, E. Bagli, L. Bandiera, et al., Tech. Rep., SLAC National Accelerator Laboratory (SLAC) (2015).

[132] H. Herminghaus, A. Feder, K. Kaiser, W. Manz, and H. Schmitt, Nuclear Instruments and Methods **138**, 1 (1976), ISSN 0029-554X, .

[133] W. Scandale *et al.*, EPL (Europhysics Letters) **93**, 56002 (2011), .

[134] M. Tobiyama *et al.*, Phys. Rev. B **44**, 9248 (1991).

[135] V. Baryshevsky and V. Tikhomirov, Nucl. Instrum. Methods Phys. Res. B **309**, 30 (2013).

[136] V. Biryukov, Phys. Lett. A **205**, 340 (1995).

[137] L. Bandiera, Ph.D. thesis, Università degli Studi di Ferrara (2015).

[138] E. Bagli and V. Guidi, Nucl. Instrum. Methods Phys. Res. B **309**, 124 (2013).

[139] L. Bandiera, E. Bagli, V. Guidi, and V. V. Tikhomirov, Nuclear Instruments and Methods in Physics Research Section B: Beam Interactions with Materials and Atoms **355**, 44 (2015), ISSN 0168-583X, proceedings of the 6th International Conference Channeling 2014:"Charged and Neutral Particles Channeling Phenomena" October 5-10, 2014, Capri, Italy, .

[140] V. Guidi, L. Bandiera and V. Tikhomirov, Phys. Rev. A **86**, 042903 (2012).

[141] E. Bagli et al., Phys. Rev. Lett. **110**, 175502 (2013).

[142] C. Gary, R. Pantell, M. Özcan, M. Piestrup, and D. Boyers, J. Appl. Phys **70**, 2995 (1991).

[143] U. Wienands, T. Markiewicz, J. Nelson, R. Noble, J. Turner, U. Uggerhøj, T. Wistisen, E. Bagli, L. Bandiera, G. Germogli, et al., Tech. Rep., SLAC National Accelerator Laboratory (SLAC) (2014).

[144] K. Olive and P. D. Group, Chinese Physics C **38**, 090001 (2014), .

[145] V. Baier, V. Katkov, and V. Strakhovenko, *Electromagnetic Processes at High Energies in Oriented Single Crystals* (World Scientific, Singapore, 1998).

[146] R. Assmann *et al.*, Proc. of European Particle Accelerator Conference: EPAC'02 pp. Report–599 (2002).

[147] R. P. Fliller *et al.*, Phys. Rev. ST Accel. Beams **9**, 013501 (2006).

[148] V. D. Shiltsev *et al.*, Proc. of 1st International Particle Accelerator Conference: IPAC'10 p. TUOAMH03 (2010).

[149] W. Scandale et al., Phys. Lett. B **703**, 547 (2011).

[150] S. Hasan, Ph.D. thesis, University of Insubria (2011).

[151] V. Biryukov, Nuclear Instruments and Methods in Physics Research Section B: Beam Interactions with Materials and Atoms **53**, 202 (1991), ISSN 0168-583X, .

[152] A. G. Afonin *et al.*, Instruments and Experimental Techniques **54**, 1 (2011), ISSN 0020-4412, .

[153] M. Pesaresi, W. Ferguson, J. Fulcher, G. Hall, M. Raymond, M. Ryan, and O. Zorba, Journal of Instrumentation **6**, P04006 (2011).

[154] D. Mirarchi, S. Redaelli, W. Scandale, and G. Hall, Ph.D. thesis, Imperial Coll., London (2015), presented 18 Jun 2015, .

[155] D. Mirarchi, S. Montesano, S. Redaelli, W. Scandale, A. Taratin, and F. Galluccio, Proceedings of IPAC **2014** (2014).